Title
Scalable Routes to Efficient Thermoelectric Materials

Author
Feser, Joseph Patrick

Publication Date
2010

Peer reviewed|Thesis/dissertation

Scalable Routes to Efficient Thermoelectric Materials

By

Joseph Patrick Feser

A dissertation submitted in partial satisfaction of the

requirements for the degree of

Doctor in Philosophy

in

Engineering - Mechanical Engineering

in the

Graduate Division

of the

University of California, Berkeley

Committee in charge:

Professor Rachel Segalman, co-chair
Professor Costas Grigoropoulos, co-chair
Professor Xiang Zhang
Professor Joel Moore

Fall 2010

Abstract

Scalable Routes to Efficient Thermoelectrics

by

Joseph Patrick Feser

Doctor of Philosophy in Engineering - Mechanical Engineering

University of California, Berkeley

Professor Rachel Segalman, Co-chair

Professor Costas Grigoropoulos, Co-chair

Thermoelectrics are solid-state materials with the ability to directly convert heat to electricity and *visa versa*. Despite their advantages in power density and reliability, state-of-the-art bulk alloy materials have not been efficient enough or inexpensive enough to be deployed widely. Newer nanostructured materials show significantly improved efficiencies and could overcome these long-standing problems. This dissertation studies the conditions that govern efficiency improvements in nanostructured materials with particular attention paid to lattice thermal conductivity reductions as well as methods to make such materials inexpensively using solution processing.

Measurements of a new p-type material system, $In_{1-x}Ga_xSb$ doped with epitaxially embedded metallic ErSb nanocrystals show that lattice thermal conductivity is reduced significantly below the alloy limit with as little as 1% nanocrystal loading by volume. Theoretical modeling based on the Boltzmann transport equation (BTE) is able to explain the reductions on the basis of an increased scattering cross section for long wavelength phonons which are scattered much less effectively by phonon-phonon and alloy impurity interactions. The optimal conditions for nanoparticle size, concentration, alloy composition are explored and the existence of an optimal nanocrystal size which depends on the alloy composition and temperature is predicted.

A variety of colloidal nanocrystals are explored as inexpensive building blocks for nanostructured thermoelectric materials with tunable electronic and thermal properties. First, the electronic properties of superlattices of PbSe nanocrystals are studied in the limit of strong quantum confinement (d<10nm). PbSe quantum dot superlattices show size-dependent Seebeck coefficient which exceed that of the bulk material at equivalent carrier concentrations. Reversible control of the carrier concentration is shown by

surface exposure of the superlattices to oxidizing and reducing agents and in-situ monitoring of the thermopower.

Next, phonon transport in ultra-fine grained nanocomposites with tunable grain size are studied using colloidal nanocrystals. Particles of CdSe are coated with a hydrazine-based metal chalcogenide ligand which serves as a functional “glue.” Composites with grain size between 3nm-6nm display ultra-low thermal conductivity approaching the theoretical limit for a crystalline solid, nearly 30 times lower than the bulk compound. Modeling shows that boundary scattering in the framework of BTE cannot adequately explain the measured properties and alternative mechanisms are discussed.

Finally, a solution processable route to $Bi_2Te_{3-x}Se_x$ thermoelectrics is developed by reacting Bi_2S_3 in hydrazine to form a universal precursor. The precursor is spin-coated in the presence of excess Se and Te and annealed to form a thermoelectrics material with a maximum ZT~0.4 at room temperature, which is the highest for any spin-coated material currently reported.

Table of Contents

List of Figures

Acknowledgements

To say that this dissertation required the help of many people would be an understatement. I am very thankful for my primary thesis advisors Rachel Segalman and Arun Majumdar who have both allowed me great leeway over the years to attack the problems that I found the most compelling; this odyssey has led me to a broad knowledge of diverse fields such as biofuel production, carbon sequestration, solar energy, microelectronics, and thermoelectrics. In the end, my dissertation will concern only thermoelectrics, but the knowledge I have gained from my dabblings in other research fields will ultimately enrich me for the rest of my career.

I have had the good fortune of collaborations with a number of outstanding researchers. Ali Shakouri and the rest of our DARPA-funded team (Josh Zide, Hong Lu, Dongyan Xu, Tim Sands, Lon Bell, Bian Zhixi to name a few) have heavily influenced the way I think about thermoelectrics material development and certain experiments would not have been possible without the high quality materials growth performed by Josh and Hong. The Molecular Foundry and their staff members have been crucial to the development of solution processed nanostructured thermoelectrics. In particular, Dmitri Talapin convinced me of the extraordinary potential of colloidal nanocrystals to revolutionize the way semiconductors are used and provided all the materials used in Chapter 4. Jeff Urban has given continual advice regarding the development of hydrazine chemistry for thermoelectric applications (Chapter 5 and 6) and has served as an unofficial advisor for several years. Special thanks also goes to Robert Wang, Jong-Soo Lee, Antie Rey, Delia Milliorn, Kin Man Yu, Emory Chan, Jeremy Schroeder, Rob Wortman, and all the other members of Prof. Majumdar's and Prof. Segalman's laboratories who have assisted with the growth and characterization of many materials.

However, in life, our current position is merely the end result of an entire trajectory. This trajectory was made possible by my mother, Sonja Comegna, who made heavy economic sacrifices to ensure that my sister and I could attend college; I can only hope that my brother is so fortunate. My wife, Allison, has also sacrificed family and career to follow me around the globe and has endured my unreasonable work schedule for many years. I would be remiss if I did not thank several professors at the University of Delaware who changed my life and made this dissertation possible: 1) Prof. Valery Roy who taught me about the existence of scientific research and took me under his wing as a sophomore, 2) Prof. Andras Szeri, who pulled strings to get me into graduate school. Twice. And 3) Prof. Ajay Prasad and Suresh Advani who gave excellent research advisement during the most productive year of my life. My education could not have been successful without these people so I am eternally grateful.

Background

General Concepts

The manipulation and conversion of heat are at the very core of the modern society. Heat engines are required for the cheap production of electricity as well as the heating and cooling of our homes (and nowadays our gadgets). Nearly 80% of the worlds energy needs are met by heat engines, most of which operate far below the maximum efficiency allowed by thermodynamics and expel heat far above the ambient temperature. Similarly, modern electronics such as the computer chip and LED have become so powerful that they are capable of releasing more heat than can be moved by solid state heatsinks or even phase-change heat transfer devices. Thermoelectrics have been proposed as solid state heat engines that may be an excellent fit for both waste-heat harvesting and high power density cooling applications.

Thermoelectrics are based on two related effects: the Seebeck effect and the Peltier effect. The Seebeck effect is the observation that when a temperature gradient exists between two junctions of a conducting material, there is a potential buildup at open circuit conditions. The proportionality between the voltage and temperature difference is known as the Seebeck coefficient. A related phenomena called the Peltier effect occurs when current passes from one material into another and absorbs or emits heat near the junction. Physically, the origin of the effect is that the average energy of an electron differs from one material to the next with respect to the chemical potential; when an electron crosses the boundary into a new material, the electron will thermalize with its new surrounds; if the new average energy is higher, then the electron must have absorbed heat. If the energy is lower, it will have emitted heat. The constant of proportionality between the heat flux and the current is called the Peltier coefficient and is mathematically related to the Seebeck coefficient, through the relation $\Pi_{1\to 2} = (S_2 - S_1)T$. To use this effect in a device, n-type and p-type materials are stacked thermally in parallel and electrically in series to form a module. If on one side of the device, heat is absorbed at the n-to-p junction, then on the other side heat will be emitted a current goes from n-to-p. Thus the device uses electrical current to move heat to a new location. If instead, a heat flux is applied to the device, current will be circulated and can be used to do work. Thus, thermoelectric modules are potentially useful for cooling and power generation applications.

The performance characteristics of thermoelectric modules intimately depend on the material properties and to some extent the geometric design. Table 1 shows some typical performance characteristics of a single leg of a thermoelectric module, neglecting thermal and electrical contact resistances [1]. Most characteristics directly depend on a non-dimensional material property known as the thermoelectric figure-of-merit,

$$ZT \equiv \frac{S^2 \sigma T}{k} \qquad 1.1$$

where S is the Seebeck coefficient, σ is the electrical conductivity, and k is the thermal conductivity. The subgrouping $S^2\sigma$ is often called the power factor, because of the scaling laws of the heat flux (refrigeration) and power density (generation). Studying the form of 1.1 it is easy to see why so many researchers have struggled to find materials with ZT>>1. Typical absolute values for the Seebeck coefficient range from ~1-1000μV/K, with the low end corresponding to metals (e.g. S_{Au}~1.7μV/K) and the high end corresponding to nearly-intrinsic semiconductors (e.g. S_{Si}~ -2000μV/K @ n_d~10^{14}/cm^3). The Seebeck and electrical conductivity have conflicting trends with carrier concentration: the Seebeck coefficient tends to be low when conductivity is high and visa-versa. In practice, the materials with the best power factors are highly doped semiconductors; the optimal doping level depends on the particular material and the temperature. At room temperature, the best known materials are $Sb_{2-x}Bi_xTe_{3-y}Se_y$ alloys which can simultaneously achieve a power factor of ~40 μW/cm-K^2 and thermal conductivity ~1 W/m-K for a ZT~1 [2]. Achieving power factors of this magnitude is difficult in most other material systems.

Refrigeration	Power Generation
$(\mathrm{COP})_{MAX} = \frac{T_c}{T_H - T_C}\left(\frac{\sqrt{1+ZT_{avg}} - T_H/T_C}{\sqrt{1+ZT_{avg}}+1}\right)$	$\eta_{MAX} = \frac{T_H - T_C}{T_H}\left(\frac{\sqrt{1+ZT_{avg}}-1}{\sqrt{1+ZT_{avg}+T_C/T_H}}\right)$
$Q''_{MAX} = \frac{S^2\sigma T_C}{L}\left(\frac{T_C}{2} - \frac{\Delta T}{ZT_C}\right)$	$W''_{MAX} = \frac{1}{2}\frac{S^2\sigma}{L}\Delta T^2$
$\Delta T_{MAX} = \frac{1}{2}ZT_C^2$	

Table 1 Performance characteristics of thermoelectrics, and their dependence on ZT in the absence of thermal and electrical contact resistance [1].

Once a suitable power factor has been obtained, achieving a low enough thermal conductivity often remains a challenge; the best electrical performance generally comes from single crystalline semiconductors. However, in crystalline samples, the scattering mechanisms are very limited, since many strategies that reduce heat transport also reduce electron transport (e.g. dislocations, defects). Physically, heat in a crystalline solid has two main carriers: electrons and nuclear motions ("phonons"). If the heat diffuses primarily because of electron motion, then electrical conductivity and thermal conductivity are inextricably linked; this is most commonly expressed as the Wiedemann-Franz law:

$$\frac{1}{L_0} = \frac{\sigma T}{k_e} \qquad 1.2$$

the constant L_0 varies slightly between metals and semiconductors but is generally ~2.5×10^{-8} $W\Omega/K^2$. In principle this "law" can be violated by having different momentum and energy relaxation time scales, but this rarely occurs in practice. I have purposefully expressed the law in the same form that it appears in the expression for ZT (equation 1.1). Since the real thermal conductivity is always larger than the electronic portion, the value of $\sigma T/k$ will always be less than the expression 1.2. This places a lower limit on the allowable Seebeck coefficient for ZT~1 (S_{min}>160μV/K). For a high ZT, the phonon component of thermal conductivity should be as low as possible, preferably smaller than the electronic component. The most broadly successful strategy has been to use heavy isoelectronic alloys (e.g. $Sb_{2-x}Bi_xTe_3$, $Pb_{1-x}Sn_xTe$, $Si_{1-x}Ge_x$) which enhances phonon scattering, slows the speed of sound, and does not significantly impede electrical transport.

Several papers have postulated the extent to which thermoelectrics could have an economic and environmental impact [3-5]. Since thermoelectrics are currently fairly inefficient (overall device generation efficiencies ~10%) compared to established energy generation techniques, there is broad agreement that thermoelectrics will require substantial improvements in performance if they are to displace existing technologies which are generally 2-5 times more efficient. However, thermoelectric heat engines have several significant advantages over existing technology. They are lightweight and very reliable with a proven record of running without maintenance for decades, as demonstrated by the thermoelectric radioisotope generators used in the Galileo and Cassani deep space probe missions [6]. They also operate nearly as well with low grade heat as with high grade heat, which has lead to a major push for thermoelectric waste heat recovery applications. For cooling, current thermoelectrics can move heat fluxes of >300W/cm^2, comparable to the critical heat flux for pool boiling, but without the dangers of the film boiling catastrophe [7]. Never-the-less, thermoelectrics are likely to initially penetrate into niche markets such a spot cooling and small scale power generation/heat recovery applications until more efficient and less expensive materials can be developed [4].

Heat Transport by Phonons in Nanostructures

Since this dissertation will focus heavily on the study of phonons in thermoelectric materials, I will discuss a few more details about the physics of phonons, most of which can be found in textbooks [1, 8, 9]. Phonons are the collective excitations of coupled oscillators: the correlation between the motions of atomic nuclei. In crystalline materials, one can envision nuclei are bonded to one another via their valence electrons, and form a large lattice of connected masses and springs. In the harmonic approximation, the motions of the nuclei are correlated and can be projected onto waves (called normal modes) of the type

$$\mathbf{u}^{\ell}(t) = \sum_{k} \mathbf{u}_{0,k}^{\ell} e^{i(\omega t - \mathbf{k}\cdot\mathbf{a})} \qquad 1.3$$

By solving the equations of motion, it can be seen that the frequency of oscillation is related to the wavelength of the oscillations; this is called dispersion, $\omega(k)$. In a three dimensional wave, there are 3 modes (degrees of freedom, known as "polarization") per nuclei of the lattice unit cell at any given k point. For each branch of the dispersion, waves carry energy at the speed of the group velocity

$$\mathbf{v}_g = \frac{\partial \omega}{\partial \mathbf{k}} \qquad 1.4$$

near the Γ point (k=0), phonons have linear dispersion so the group velocity is simply the speed of sound. When multiple atoms exist in a unit cell, often but not always, there is a region of forbidden frequencies, the size of which depends on the degree of mass and bonding mismatch as well as the crystal symmetry. Generally, large mass or bonding strength inhomogeneities within the unit cell lead to larger regions of forbidden energies. Dispersion relations for GaSb are shown in Figure 1 for some high symmetry directions. Note that the high energy modes (called "optical" modes) are fairly flat, meaning they have low group velocity. This, combined with short-lifetime of optical phonons, will lead us to neglect optical phonon transport for modeling of the thermal conductivity.

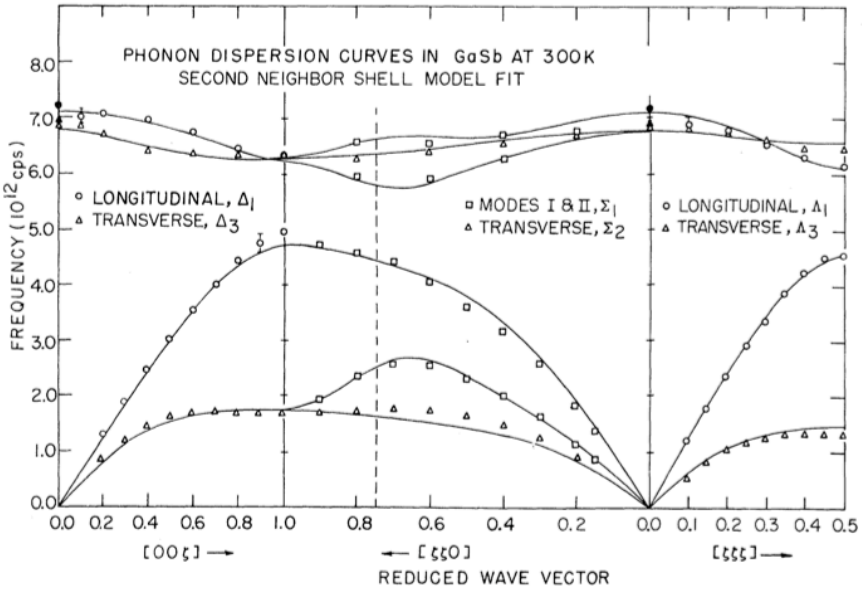

Figure 1 Phonon dispersion of GaSb from [10]

The treatment thus far has been entirely based on classical physics. However, viewing the motions based on the quantum mechanical Hamiltonian for harmonic oscillators, the energy of vibrations is quantized and in three dimensions depends on the frequency as

$$E(\mathbf{k}) = \hbar\omega(\mathbf{k})\left(n_0 + \frac{3}{2}\right) \qquad 1.5$$

where n_0 (= 0, 1, 2 , …) is the quantum "occupation" number for the n^{th} excited state. Since phonons are bosons, from statistical thermodynamics the occupation number follows Bose-Einstein statistics

$$\langle n_0 \rangle = \left(e^{\frac{\hbar\omega}{k_B T}} - 1 \right)^{-1} \qquad 1.6$$

which approximately goes as $\langle n_0 \rangle \sim \frac{k_B T}{\hbar\omega}$ at high temperature. Note that even the highest phonon energies are typically ~40meV in energy, comparable to the thermal energy at room temperature. Since even very small nanocrystals have hundreds to thousands of atoms, the separation between energy levels is very small compared to the thermal energy and thus quantum effects (apart from the following of Bose-Einstein statistics) such as changes to the phonon density of states are not expected near room temperature.

To calculate the thermal conductivity of a solid using the above relations, we can use the Boltzmann transport theory approach. The solid will have spatially dependent average occupation number n(x,k,T) and thus regions of differing occupation will exchange phonons with one another. Mathematically

$$\frac{Dn}{Dt} = \mathbf{v}_g \bullet \frac{\partial n}{\partial \mathbf{x}} = \left(\frac{\partial n}{\partial t} \right)_{scat} \qquad 1.7$$

Making the usual relaxation time approximation, we can model the scattering as having a characteristic timescale to restore it to the thermodynamically required equilibrium

$$\left(\frac{\partial n}{\partial t} \right)_{scat} = \frac{\langle n \rangle - n}{\tau} \qquad 1.8$$

and approximating $\nabla n \approx \nabla \langle n \rangle$ then the equation can be solved as

$$n = \langle n \rangle - \tau \mathbf{v}_g \bullet \frac{\partial \langle n \rangle}{\partial \mathbf{x}} \qquad 1.9$$

To calculate the thermal conductivity, the heat flux can be written

$$\begin{aligned} \mathbf{q} &= \sum_{\mathbf{k},\alpha} \mathbf{v}_{g,\mathbf{k}} \hbar\omega_{\mathbf{k}} n \\ &= \sum_{\alpha} \int_{\omega} d\omega \left(\hbar\omega D(\omega) n(\omega, T) \mathbf{v}_{g,\omega} \right) \end{aligned} \qquad 1.10$$

where to make the integral, the density of states was used. Using the expression for n

$$\frac{\partial n}{\partial \mathbf{x}} = \frac{dn}{dT} \frac{\partial T}{\partial \mathbf{x}} \qquad 1.11$$

$$\mathbf{q} = -\left\{ \sum_{\alpha} \int_{\omega} d\omega \left(\hbar\omega D(\omega) \tau(\omega) \frac{d\langle n \rangle}{dT} \mathbf{v}_{g,\omega} \mathbf{v}_{g,\omega} \bullet \right) \right\} \frac{\partial T}{\partial \mathbf{x}} \qquad 1.12$$

From the form of 1.12 it can be seen that the bracketed expression is the thermal conductivity. In the case of isotropic, dispersionless materials with energy independent scattering time

$$k = \frac{1}{3} C v_s \ell \qquad 1.13$$

The above equations are overly simplified since scattering processes are considerably more complicated than the relaxation time approximation allows. The so-called Normal phonon-phonon scattering process, for example, does not change the overall momentum of the involved phonons and thus cannot alter the thermal conductivity, but it does redistribute the momentum of the individual phonons which is important to account for at low temperature [11]. In a later chapter, I will use a simplified version of equation 1.12 developed by Callaway, that assumes isotropic, dispersionless media while maintaining the effect of Normal phonon processes by instead re-modeling the scattering time. The details of that calculation will be discussed therein.

Much of the current work will focus on the role that nanostructures play in reducing the phonon thermal conductivity. Many researchers have reported over the previous decade that the efficiency of their thermoelectric materials have been increased by the use of nanostructures. Initially, it was thought that the increases would come from electron quantum confinement which had been predicted to raise the power factor by changing the shape of the electron density of states to be more asymmetric with respect to the Fermi surface [12-14]. While efficiency gains due to this effect were not ultimately observed experimentally, the excitement drew many other workers into the field, who then discovered the benefits these structures had on *phonons*. Venkatasubramanian made a landmark discovery in 2001 with the measurement of a ZT~2.4 at 300K and a maximum heat flux of 900W/cm^2 in an ultra-small period superlattice of Bi_2Te_3:Sb_2Te_3 [15]; currently, this is the highest reported value for any material or temperature. In a later paper it was reported that the through plane lattice thermal conductivity was nearly 0.2 W/m-K, a fivefold improvement over the alloy material. Several years later Hsu [16] reported a ZT~2.2 for a bulk material PbTe simultaneously doped with Ag and Sb. It was discovered that the Ag and Sb were reacting within the materials to form $AgSbTe_2$ nanocrystals (11% by vol) embedded in the larger PbTe matrix, and were significantly decreasing the lattice conductivity. Poudel recently reported a method of making materials with very small grainsize that enhances the efficiency of traditional thermoelectric alloys by reducing the lattice thermal conductivity [2]. Other nanostructured materials such as nanowires [17, 18] and nanomeshes [19] have similarly shown marked improvement in the lattice conductivity. While the long mean-free-path in pure semiconductors like silicon has been known for some time, the reduced thermal conductivity of heavily alloyed compounds was slightly more surprising. Previous work in our group has focused on explaining the reduced conductivity in these systems [20], and I will also devote a chapter to several new observations made while studying a new nanostructured $In_{1-x}Ga_xSb$ material system.

Scalable Production of Thermoelectric Materials

One less-discussed aspect of thermoelectrics is the need for scalable approaches to the production of such materials. While it is easy to say that a thermoelectric power module could be used for waste-heat scavenging, the scale of energy production should be kept in mind. An average coal power plant produces ~200MW of electricity (loses ~600MW as heat @ ~400C), then in order to recover 10% of the lost heat using a thermoelectric with power factor of 45$\mu W/cmK^2$ would require >100m^2 of thermoelectric modules (or on the order of 1 metric ton of thermoelectric material). This would be a major problem if the material were based on Tellurium, which has a total annual worldwide production of only 100ton/yr and costs ~$100,000/ton [21], especially since the total installed coal capacity in the US is close to 200,000MW [22]. It would also present a manufacturing issue. Traditionally, thermoelectric modules are made using single crystals that are nearly 1mm thick. While using modern, nanostructured materials would reduce the required amount of material due to efficiency gains, the manufacturing methods may not be scalable enough to be competitive even with existing thermoelectrics. Typical routes to nanostructured thermoelectrics include the use of relatively non-scalable growth techniques such as Molecular Beam Epitaxy [23, 24], Metal-Organic Chemical Vapor Deposition [15], and controlled phase-segregation during ingot growth [16] which require slow growth rates, high temperatures, and/or high vacuum environments. Recent attempts have focused on the use of more earth abundant materials (e.g. Silicon [17, 18]), however these materials are not yet competitive in terms of efficiency and device performance has yet to be demonstrated. One promising recent development was the discovery of the ball-mill/SPS technique [2] which has improved the performance of $Sb_{2-x}Bi_xTe_3$ by about 25% while removing the need for single crystal samples.

In that technique, a starting material (initially single crystals [2], but later mixtures of pure elements [25]) were crushed by a high energy ball-mill until a very fine powder composed of nanograins was formed; to rebuild the material into a dense module, the grains are pressed and heated using internal Joule heat, until the particles fuse and form grain boundaries. The grain boundaries lead to improved thermal conductivity, but appearently do not lead to lower electrical conductivity in many compounds. Despite the success of this method, there are several disadvantages to this approach. First, the ball milling approach leads to non-monodisperse sizes. Also, grain sizes tend to be fairly high (~20nm); while this is small enough to see an improvement over bulk properties, it is not small enough to change the ZT of a bad thermoelectric material into a good one. Lastly, the ball-milling stage is time and energy intensive.

One primary focus of this dissertation will be to develop techniques that address the issue of scalability of thermoelectrics. The primary inspiration is from the field of organic photovoltaics which has long realized the importance of scalability and the interplay between cost/m^2, efficiency, and ultimately $/W. By moving to solution processing, manufacturing can be accomplished by techniques such as printing, casting, or spray-coating, which greatly reduces the manufacturing cost while simultaneously offering the ability to pattern. However, traditional organic semiconductor materials are currently far from suitable for thermoelectrics, having

typical mobilities <1 cm^2/V-s; even inorganic materials with mobilities O(1000 cm^2/V-s) struggle to obtain ZT near 1! However, over the last decade a number of solution-processable inorganic materials have been discovered that should be of interest to the thermoelectrics community. Three of the chapters are devoted to ideas that have been pursued along these lines. The approach has been to use knowledge from colloidal chemistry and the rapidly developing field of metal chalcogenide cluster chemistry to form novel materials that are interesting for thermoelectric applications as well as to conduct fundamental studies into phonon and electron transport at the nanoscale.

Colloidal nanocrystals are excellent building blocks for nanostructures. Nanocrystals between 2-20nm can be made entirely in solution for an astonishing variety of metals, semiconductors, and magnetic materials [26], often with the ability to sensitivity tune the size and shape. In this size range, the thermal, electrical, and optical properties are a function of the size and thus colloidal crystals have novel material properties. Monodisperse colloidal nanocrystals are known to self assemble into long-range superlattices when deposited on substrates and have collective properties of their own. Furthermore, when multiple nanocrystal types and sizes are mixed, they can form a complex variety of super-crystals [27]. In particular, colloidal nanocrystals are an excellent match for thermoelectric applications. The sizes of colloidal particles are well below the sizes achievable by other methods such as spinodal decomposition, molecular beam epitaxy, or metal organic chemical vapor deposition and are highly controllable. This in turn could be used to achieve much lower lattice thermal conductivity than has been previously observed. Especially good techniques exist for the colloidal synthesis of IV-VI compounds such as PbS, PbSe, PbTe, GeTe which are known to be good thermoelectrics in bulk. Apart from lattice thermal conductivity reductions, these nanocrystals are expected to have thermoelectrical properties significantly different from their bulk compounds due to strong 3 dimensional quantum confinement which leads to discretized energy states within the nanocrystals.

Another solution processing route amenable to thermoelectric applications is metal chalcogenide cluster chemistry. The main idea is to form soluble precursor compounds that can be decomposed into useful semiconductors. Mitzi [28] has developed a process that uses hydrazine as a reducing agent to react metal chalcogenide semiconductors with excess chalcogen to form small molecules stabilized by hydrazinium cations. The resulting compounds are soluble in polar solvents but unstable at elevated temperature with volatile decomposition products that allow for the recovery of the initial metal chalcogenide semiconductor. The first demonstration of this technology was for SnS_2 and $SnSe_2$ thin film transistors deposited by spin coating [28]. There, 2mmol SnS_2 and 2mmol S was reacted in hydrazine to form the compound $Sn_2S_6(N_2H_4)_x(N_2H_5)_4$ which was spin coated and then decomposed at 200°C to recover SnS_2 (and the decomposition gases H_2S, N_2, H_2, N_2H_4). Transistors from $SnS_{2-x}Se_x$ showed mobilities as high as 12 cm^2/V-s. Many compounds that use this chemistry have been developed for other applications. Mitzi [29] has demonstrated p-type transistors by combining precursors for Cu_2S and In_2Te_3 to form $CuInTe_2$ films with mobility ~10 cm^2/V-s. Milliron [30] demonstrated phase-change memory devices made from a mixture of Sb_2Se_3 and $GeSe_2$ precursors with switching times ~100ns; Mitzi has

demonstrated the phase change material KSbS by a similar route [31], but with slower switching times. The IBM research group has also demonstrated the utility of these methods for the scalable production of solar cells of $CuIn_{1-x}Ga_xSe$ (10% efficiency, AM 1.5 Illumination) [32], $CuInS_{2-x}Se_x$ (12% eff.) [33], Cu-Zn-Sn-S-Se (9.6% eff.) [34], and Sb doped $CuIn_{1-x}Ga_xSe$ (12.3% efficiency) [35]. A full table of known compounds is given in Table 2. Given the excellent electrical properties displayed by the solution processed metal chalcogenide films, its seems logical to apply this technique to the field of thermoelectric materials. Apart from a single report appearing earlier this year [36], this topic has been complete unexplored for thermoelectrics applications.

MCC formula	Semiconductor	Ref
$Sn_2S_6(N_2H_5)_4$	SnS_2	[28]
$Sn_2Se_6(N_2H_5)_4$	$SnSe_2$	[28]
$Ge_2S_6(N_2H_5)_4$	GeS_2	
$Ge_2Se_6(N_2H_5)_4$	$GeSe_2$	[30]
$ZnTe(N_2H_4)$	ZnTe	[37]
$Cu_7S_4(N_2H_5)$	Cu_2S	[38]
$Sb_2S_6(N_2H_5)$	Sb_2S_3	
$Sb_2Se_6(N_2H_5)$	Sb_2Se_3	[30]
$Sb_2Te_8(N_2H_5)_x$	Sb_2Te_3	[39]
$In_2Se_4(N_2H_5)_2$	In_2Se_3	[40]
$In_2Te_3(N_2H_4)_x$	In_2Te_3	[29]
$Ga_2Se_3(N_2H_4)_x$	Ga_2Se_3	[32]
$HgSe_2(N_2H_5)_2$	HgSe	[39]

Table 2 List of known Metal Chalcogenide clusters and their parent compounds.

Chapter Layout

Chapter 2 will cover the experimental methodology used for thermal characterization of materials. This will start by covering the fundamentals of the 3ω method, including the instrumentation, sample preparation, and data reduction. Particular attention will be paid to uncertainty analysis and the optimization of

experiments. The chapter will conclude by discussing the feasibility of performing anisotropic thermal conductivity experiments.

Chapter 3 will concern the thermal characterization and modeling of a new nanostructured $In_{1-x}Ga_xSb$ material with embedded ErSb nanocrystals. The conditions under which nanostructuring can reduced thermal conductivity will be shown. Modeling shows that particle size, alloy content, and temperature play crucial roles in the effectiveness of such nanocomposites. In particular, there is an optimal particle size and alloy content that minimizes the thermal conductivity.

Chapter 4-6 will discuss routes to scalable thermoelectric materials. Chapter 4 will demonstrate the unique thermoelectric aspects of strongly confined quantum dot superlattice made of colloidal PbSe. Here it will be shown that quantum confinement yields a size-dependant Seebeck coefficient with values far beyond bulk for comparable carrier concentrations. Further, thermopower measurements can be used to understand the nature of the conduction mechanisms in such systems.

Chapter 5 will show that dense composites of colloidal crystals can be formed to study the thermal transport mechanism in ultra-fine grained structrures. Thermal conductivity approaching the theorectical limits of diffusive conduction are found confirming the utility of the method.

Chapter 6 will demonstrate a new solution processing route to make spin coated films of $Bi_2Se_{3-x}Te_x$. This is done by first developing a universal precursor based on Bi_2S_3 which is then mixed in appropriate amounts with solublized Se and Te. After a low temperature anneal, material with excellent thermoelectric properties are attained with the ZT~0.4 at room temperature, among the best reported from solution.

Thermal Characterization

Fundamentals of the 3ω Technique

The 3ω technique has been used throughout this work as method of the determining the thermal conductivity of thin films and bulk substrates. Although it has not always been a glorious endeavor, I have developed significant knowledge of the technique including the discovery of several aspects related to performing high temperature measurements and uncertainty analysis which have been overlooked by previous researchers. The purpose of this chapter is to explain in detail how experiments have been performed and why. The chapter will discuss the origin of experimental uncertainty and several methods that have implemented to achieve state-of-the-art thermal measurements. The chapter will finish by demonstrating the possibility of measuring in-plane thermal conductivity. It will be shown that, using an optimized experimental arrangement, the accuracy of in-plane measurements can be significantly enhanced and may even exceed those of more traditional suspended membrane techniques.

Fundamentally, the focus of any technique that measures the thermal conductivity is to quantify the relationship between the heat flow and temperature gradient. The 3ω method is a frequency domain method that makes use of a judiciously arranged resistive thermometer to both supply Joule heat and to measure the temperature of the thermal waves using the temperature dependence of resistivity [41-43]. The value of the temperature coefficient of resistance (TCR) for most metals is similar at room temperature, ~O(0.4% /K). If the temperature fluctuations are a small fraction of the absolute temperature, the change in resistance of the heater is relatively small in a typical experiment. To achieve excellent sensitivity, 3ω methods employ lock-in techniques to reject signals and noise sources not associated with the thermal signal. A typical implementation of the 3ω method for a dielectric thin film sample is shown in Figure 2.

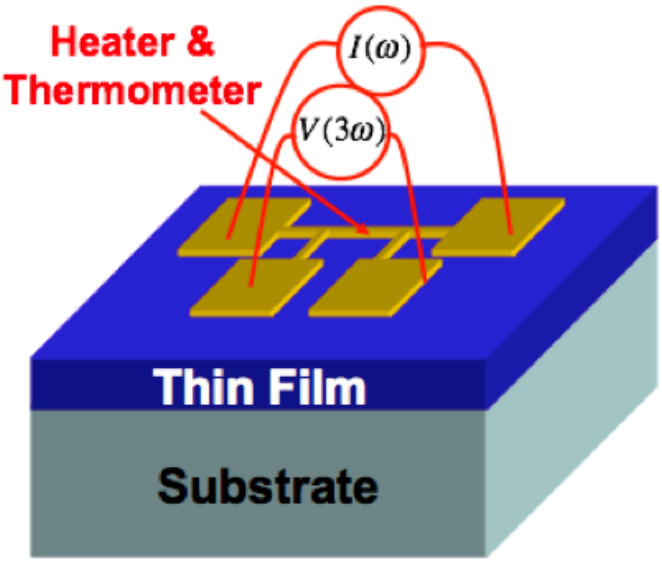

Figure 2 Schematic arrangement of a 3ω experiment

An AC current source supplies current at frequency ω to a micropatterned resistive heater configured to measure the 4-wire resistance.

$$I = I_0 sin(\omega t) \tag{2.1}$$

The current generates Joule heating, $Q = I^2 R$ which serves to heat the wire.

$$Q = I_0^2 sin^2(\omega t) R_s(Q,\omega) \tag{2.2}$$

Typically, the approximation that $R_s(Q,\omega) \approx \mathrm{R}_{s,0}$ is made; the ramifications of this approximation are small when the external circuitry are properly implemented as will be discussed in association with uncertainty analysis. Then, the equation can be simplified

$$\begin{aligned} Q &= \frac{I_0^2 R_{s,0}}{2} - \frac{I_0^2 R_{s,0}}{2}\cos(2\omega) \\ &= Q_{DC} + Q_{2\omega}\cos(2\omega) \end{aligned} \tag{2.3}$$

Thus, in addition to a DC component, heat is generated at frequency 2ω. Using a lock-amplifier, the 2ω component of heat generation can be measured as

$$Q_{2\omega} = \frac{V_{0,RMS}^2}{R_{s,0}} \tag{2.4}$$

The heat generates a temperature fluctuation with amplitude $\Delta T_{2\omega}$ at the same frequency, but generally out of phase by angle $\phi(\omega)$. The temperature fluctuation imparts a small change in the resistance of the heater line because of the temperature coefficient of resistance.

$$\begin{aligned} R_s &= R_{s,0} + \left(\frac{dR}{dT}\right)\Delta T \\ &= R_{s,0} + \left(\frac{dR}{dT}\right)\Delta T_{2\omega} cos(2\omega t + \phi) \end{aligned} \qquad 2.5$$

Thus, the first perturbation to the voltage drop across the heater is

$$\begin{aligned} V &= IR_s \\ &\approx I_0 R_{s,0} \sin(\omega t) + I_0 \left(\frac{dR}{dT}\right)\Delta T_{2\omega} cos(2\omega t + \phi)\sin(\omega t) \\ &= V_0 \sin(\omega t) + \frac{V_0}{R_{s,0}}\left(\frac{dR}{dT}\right)\Delta T_{2\omega} cos(2\omega t + \phi)\sin(\omega t) \\ &= V_0 \sin(\omega t) + \frac{V_0}{R_{s,0}}\left(\frac{dR}{dT}\right)\frac{\Delta T_{2\omega}}{2}\left[\sin(3\omega t + \phi) - sin(\omega t - \phi)\right] \\ &= \left[V_0 \sin(\omega t) - \frac{1}{2}\frac{V_0}{R_{s,0}}\left(\frac{dR}{dT}\right)\Delta T_{2\omega} sin(\omega t - \phi)\right] + \left[\frac{1}{2}\frac{V_0}{R_{s,0}}\left(\frac{dR}{dT}\right)\Delta T_{2\omega} \sin(3\omega t + \phi)\right] \\ &= V_{1\omega} sin(\omega t + \chi) + V_{3\omega} sin(3\omega t + \phi) \end{aligned} \qquad 2.6$$

From the last and second-to-last line, it is seen that signatures of the temperature fluctuation exist in the voltages at frequency 1ω and 3ω. As the name suggests, the 3ω method uses the voltage at frequency 3ω to measure the temperature. Rearranging the 3ω component of equation 2.6,

$$\Delta T_{2\omega} = 2\frac{dT}{dR} R_{s,0} \frac{V_{3\omega}}{V_0} \qquad 2.7$$

Note that the initial paper describing the 3ω method is missing a factor of 2 in this equation [41], which has been corrected in a subsequent erratum. For a typical experimental setup, the temperature fluctuation is small enough that $V_0 \approx V_{1\omega}$ so that

$$\begin{aligned} \Delta T_{2\omega} &= 2\frac{dT}{dR} R_{s,0} \frac{V_{3\omega}}{V_{1\omega}} \\ &= 2\frac{dT}{dR} R_{s,0} \frac{V_{3\omega,RMS}}{V_{1\omega,RMS}} \end{aligned} \qquad 2.8$$

Equation 2.4 & 2.8 provide a means to directly measure the thermal transfer function in the frequency domain. Since the transfer function depends on frequency, data collection consists of sweeping the excitation frequency at fixed $V_{1\omega}$ and measuring the 3ω Voltage, which generates a characteristic "3ω curve." Figure 3 is an example curve for a CdSe substrate.

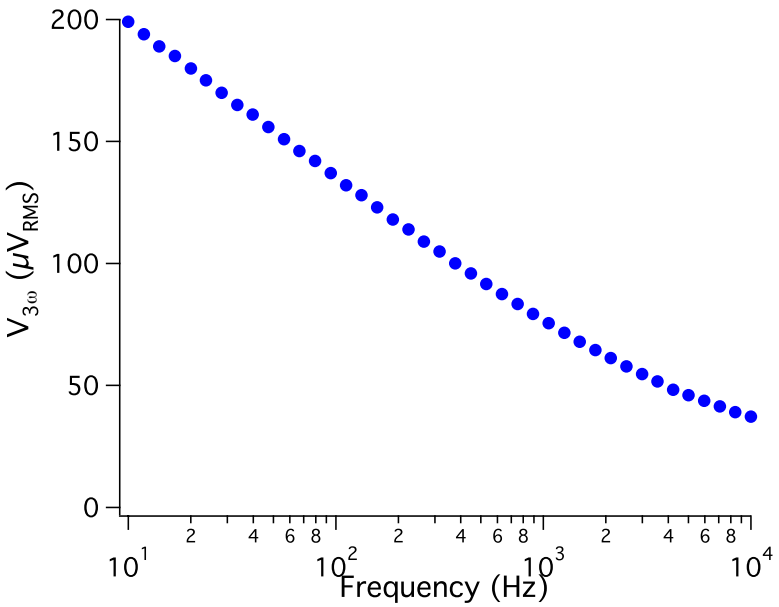

Figure 3 In-phase part of the measured 3ω curve for CdSe near room temperature. At low frequency the slope of the curve on a logscale is indicative of the substrate thermal conductivity (see equation 2.19)

Current Sources vs. Voltage Sources

While the above equations have been derived for a sinusoidal current source, in practice, a voltage source is often used to generate the Joule heating. Using the same first order analysis, the current that travels through the sample is

$$I_S \approx \frac{V_s}{R_{s,0}} \qquad 2.9$$

where the sample voltage, V_s, produced by the voltage source, V_{GEN}, is simply

$$V_s = \frac{R_s}{R_s + R_{EXT}} V_{GEN} \qquad 2.10$$

where R_{EXT} is any resistance in the circuit external to the sample. However, the first-order analysis with a voltage source has a critical flaw: the 3ω voltage generated as a result of the sample heating cannot be balanced by any other circuit component; the voltage source can only support the 1ω voltage (by definition), and since to first order the current through the external resistance is at frequency 1ω, the potential drop across the external resistance R_{EXT} is also at frequency 1ω. Physically, the way this inconsistency is resolved is by the generation of an additional current at frequency 3ω, which is not accounted for in the first order analysis. Mathematically, it is necessary to carryout the second order analysis to correct this issue.

If the signal $V_{3\omega}$ from the first-order analysis is considered as a voltage source for a second-order analysis, the additional current through the circuit is

$$I_{3\omega}^{(2)} = -\frac{V_{3\omega}^{(1)}}{R_s + R_{EXT}} \qquad 2.11$$

where the superscripts denote the order of the approximation, for clarity ($V_{3\omega}^{(1)}$ corresponds to equation 2.6). This generates additional potential drops across the sample and external resistance

$$V_{3\omega,sample}^{(2)} = -\frac{R_s}{R_s + R_{EXT}} V_{3\omega,sample}^{(1)} \qquad 2.12$$

and

$$V_{3\omega,EXT}^{(2)} = -\frac{R_{EXT}}{R_s + R_{EXT}} V_{3\omega,sample}^{(1)} \qquad 2.13$$

where we have neglected the effect of further heating in the sample. Note that the potential drops in the second order analysis (eq 2.12 and 2.13) are of the same order-of-magnitude as the first, and therefore should not be neglected in general, when using a voltage source. If only the 3ω voltage across the sample is measured, Equation 2.8 could not be applied, then.

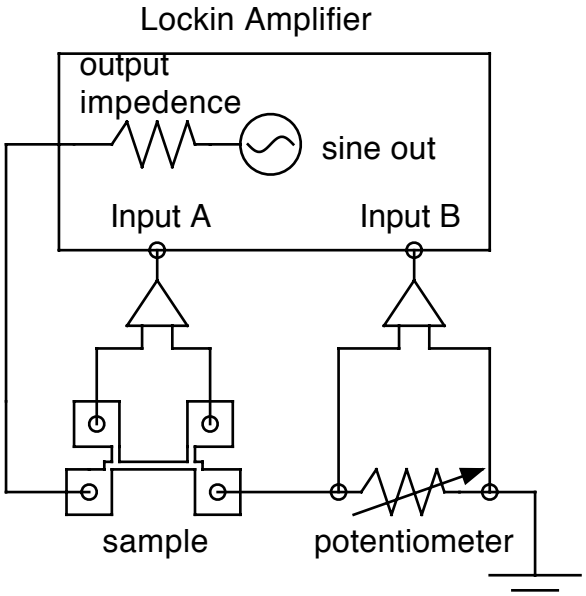

Figure 4 Schematic Circuit Diagram of the 3ω Experiments

Dames et al. [43] suggests mitigating the effect of the voltage source by placing a large "ballast" resistor in series with the sample, which effectively mimics a current source. However, unrealistically large voltages are often required to generate a desirable amount of current in this arrangement, so an alternative circuit arrangement shown in Figure 4 has been used (with the detailed circuit components shown in Figure

5). A heat-sunk precision potentiometer with constant and known resistance is placed in series with the sample heaterline. When the resistances of the potentiometer and sample are matched, the two experience the same potential drop, with the exception of the thermal component which only occurs in the sample. Thus, if the potential across the sample and potentiometer are subtracted in a differential circuit, including the 3ω voltages from the first and second order analysis

$$\begin{aligned}(V_S - V_{Pot})_{3\omega} &= (V^{(1)} + V^{(2)})_{3\omega,sample} - (V^{(2)})_{3\omega,Pot} \\ &= \left(1 - \frac{R_s}{R_s + R_{EXT}}\right)V_{3\omega}^{(1)} - \left(-\frac{R_{Pot}}{R_s + R_{EXT}}\right)V_{3\omega}^{(1)} \\ &= V_{3\omega}^{(1)}\end{aligned} \qquad 2.14$$

Thus, the spurious 3ω current that occurs as a result of using a non-ideal current source does not effect the measurement when the circuit is used, and Equation 2.8 is still a correct measure of temperature so long as the differential signal $(V_S - V_{Pot})_{3\omega}$ is used rather than $V_{S,3\omega}$ directly. In order to automate this process, it is more convenient to employ a fixed potentiometer setting and instead use a multiplying digital-to-analog converter (MDAC). In this case, rather then setting $R_s = R_{Pot}$ by hand, the MDAC factor α can be adjusted in software such that $R_s = \alpha R_{Pot}$ which achieves the same final result.

$$\begin{aligned}(V_S - V_{Pot})_{3\omega} &= \left(1 - \frac{R_s}{R_s + R_{EXT}}\right)V_{3\omega}^{(1)} - \left(\frac{\alpha R_{Pot}}{R_s + R_{EXT}}\right)V_{3\omega}^{(1)} \\ &= V_{3\omega}^{(1)}\end{aligned} \qquad 2.15$$

Using a computer code, the exact circuit equations have been simultated and it is found that the approximations used give the correct thermal transfer functions to better than 0.5% when $\Delta T / T < 0.05$ which is acceptable for all experiments reported here.

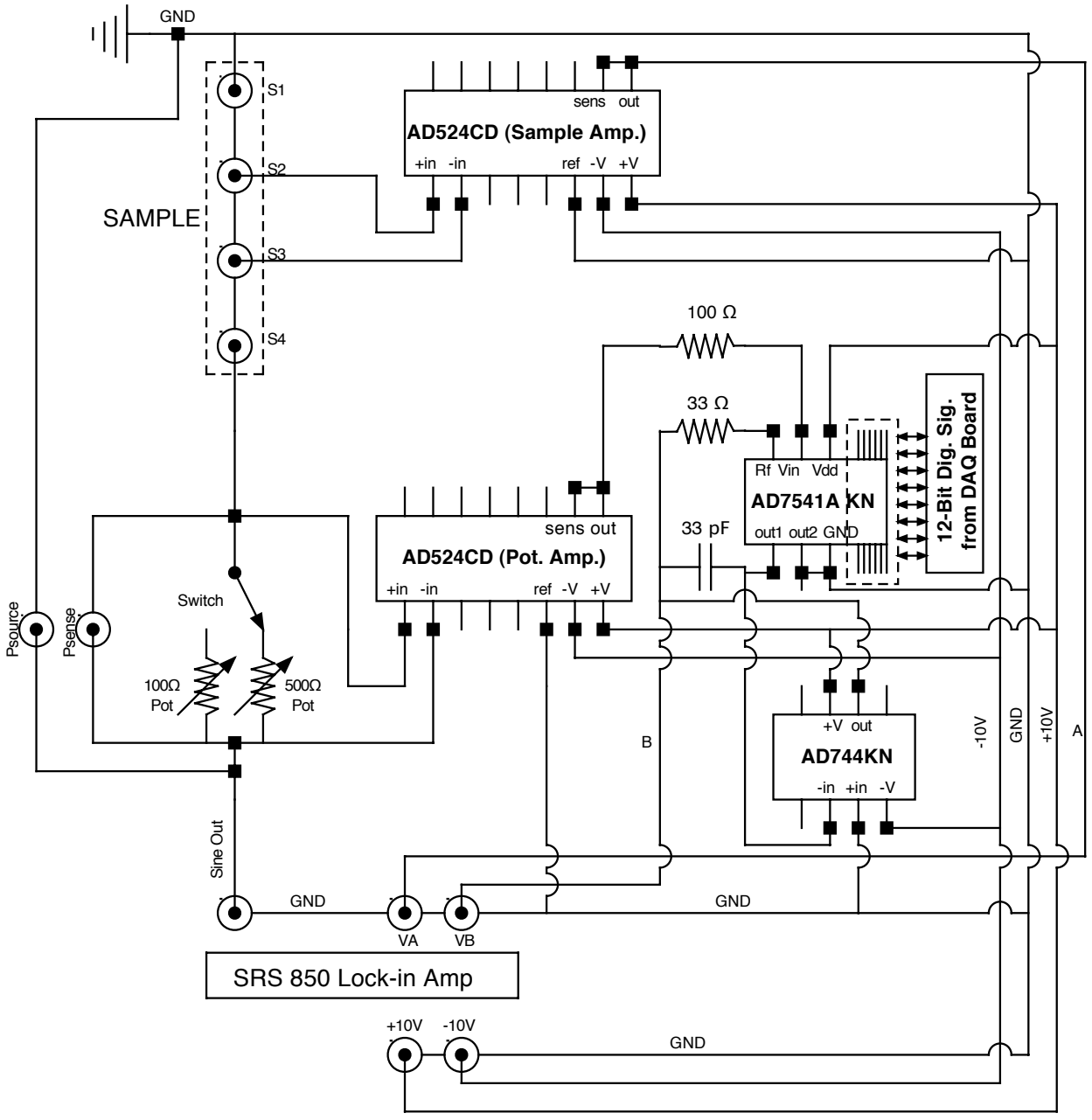

Figure 5 Circuit diagram for 3ω measurements

Data Reduction

Equation 2.4 and 2.8 provide a direct measurement of the thermal transfer function of the system. By fitting the measured transfer function to a thermal model, properties of the underlying materials can be determined. The next section will discuss modeling techniques and data reduction for the 3ω method, starting from a 2D solution of the transient diffusion equation for an N-layer system with anisotropic thermal

conductivities, and then several useful approximations which allow simple analysis for bulk materials and thin films measured experimentally.

Borca-Tascuic has reported an analytic solution of the transient heat equation [42] for an anisotropic N-layer system with a uniform heat flux of width, 2b, on the surface

$$\langle \Delta T \rangle = \frac{-p}{\pi L k_{y1}} \int_0^\infty \frac{1}{A_1 B_1} \frac{\sin^2(b\lambda)}{b^2 \lambda^2} d\lambda \qquad 2.16$$

where

$$A_{i-1} = \frac{A_i \dfrac{k_{y,i} B_i}{k_{y,i-1} B_{i-1}} - \tanh(\phi_{i-1})}{1 - A_i \dfrac{k_{y,i} B_i}{k_{y,i-1} B_{i-1}} \tanh(\phi_{i-1})}, i = N..2$$

$$B_i = \left(\eta_i \lambda^2 + \frac{i2\omega}{\alpha_{y,i}} \right)^{1/2}, \quad \phi_i = B_i d_i, \quad \eta = k_x / k_y \qquad 2.17$$

In the above expressions, N is the total number of layers (where the top-most layer with the heaterline is layer number 1), k is thermal conductivity, α is thermal diffusivity, p/l is the heater power per length, and d is the thickness of the layer. The bracket notation $\langle \Delta T \rangle$ is meant to imply the temperature on the surface is averaged over the linewidth; since the averaged quantity will be reported in all further equations in this paper, the notation will be dropped going forward. Although analytic, the evaluation generally requires iterative substitution followed by numerical integration over a very large range of wavelengths. An efficient MATLAB algorithm for accomplishing this is included in the Appendix II. Note that the temperature fluctuation in this formulation is generally complex, indicating the in-phase and out-of-phase component of the temperature fluctuation. While this formulation will be used to analyze very general multilayer heat transport, it is instructive to study common simple geometries.

The simplest example is of a very thin heater on an isotropic, semi-infinite substrate. In that case, Cahill has shown that the equations simplify to

$$\Delta T = \frac{p}{\pi L k} \left(0.5 \ln\left\{ \frac{k}{\rho C b^2} \right\} - 0.5 \ln(2\omega) + \eta - i\frac{\pi}{4} \right) \qquad 2.18$$

where η is a constant which has been numerically evaluated to be ~0.923 [41]. Taking the derivative of equation 2.18, with respect to $\ln(2\omega)$ it can be seen that

$$k_S = -\frac{P}{2\pi L} \left(\frac{d(\Delta T)}{d(\ln(2\omega))} \right)^{-1} \qquad 2.19$$

Thus, by taking the slope of the experimentally measured ΔT vs $\ln(\omega)$ curve, the thermal conductivity of the underlying substrate can be determined. A length scale known as the thermal penetration depth can be defined from dimensional considerations,

$$L_P \equiv \left(\frac{\alpha}{2\omega} \right)^{1/2} \qquad 2.20$$

which physically represents the distance a thermal wave travels over the period of the heat oscillation. In order to satisfy the approximations made in the slope method, the fitting must be applied within a somewhat restricted frequency regime. To approximate an infinitely small line source experimentally, the penetration depth should be larger than the linewidth (which is finite in reality), and in order to justify the semi-infinite substrate approximation, the penetration depth should be shorter than the thickness of the substrate (which is finite in reality). Thus,

$$t_{sub} < L_P < b \qquad 2.21$$

In principle, the thermal conductivity could also be determined by fitting to the out-phase signal or some other scheme, such as a fit to the phase lag between the heat flux and temperature. However, calculating the thermal conductivity by using the slope method has the advantages that it is highly insensitive to external uncertainties in linewidth, specific heat, and interfacial resistances and it determines the thermal conductivity directly instead of the thermal diffusivity or effusivity. Additionally, the magnitude of the in-phase portion of the temperature fluctuation is generally much larger than the out-of-phase temperature fluctuation which justifies use of only the in-phase portion.

Another very common use of the 3ω method is to determine the thermal conductivity of a thin film on a substrate. In the most common situation, a film with low thermal conductivity is deposited on a high thermal conductivity substrate with the heaterline on top of the film. It is often possible to design the experiment to operate in a long-wavelength limit such that the heater width is larger than the film thickness ($b >> t_f$), the penetration depth of the film exceeds its thickness ($L_P^f >> t_f$), and the penetration depth in the substrate exceeds the linewidth ($L_P^{sub} >> b$). Then, heat flow within the thin film may be treated as quasi-steady and one-dimensional. Then, the temperature drop across the film is linear and is in-phase with the heaterline heat flux. The temperature drop across the film is simply

$$P = k_f L w_f \frac{\Delta T_f}{t_f} \qquad 2.22$$

where $\Delta T_f = \Delta T_{total} - \Delta T_{sub}$ and $w_f \equiv 2b_f$ is the heaterline width. Since the heat travels one dimensionally through the thin film, the condition at the surface of the substrate remains one of constant heat flux. Thus, the temperature fluctuation of the substrate can be analyzed similarly to Equation 2.18. To first order, the effect of the film is to add an additional component to the in-phase temperature fluctuation.

$$\Delta T_{total} = \frac{P}{\pi L k_S}\left(0.5\ln\left\{\frac{k_S}{\rho_S C_S b^2}\right\} - 0.5\ln(2\omega) + \eta - i\frac{\pi}{4}\right) + \frac{Pt_f}{Lw_f}\frac{1}{k_f} \qquad 2.23$$

This equation suggests a method to determine the thermal conductivity of the film and substrate using a single experiment. The thermal conductivity of the substrate can first be determined directly from the frequency dependence of the transfer function.

$$k_S = -\frac{P}{2\pi L}\left(\frac{d(\Delta T_{total})}{d(\ln(2\omega))}\right)^{-1} \qquad 2.24$$

If the specific heat capacity of the substrate is known, then the temperature fluctuation in the substrate, ΔT_S, can be modeled using eq. 2.18. Then, using $\Delta T_f = \Delta T_{total} - \Delta T_S$ the properties of the film can be determined

$$k_f = \frac{Pt_f}{Lw\Delta T_f} \qquad 2.25$$

This technique is known commonly as the "slope" method. It works well for the simple case of a single layer on a substrate, and is often the only possible way to extract the thermal conductivity (such as when a dielectric film is deposited on a high electrical conductivity substrate). However, there are several caveats to the use of the slope method: 1) it cannot account for boundary resistance and thus may not be applicable to very thin films where interfacial boundary resistance plays a strong role or to films that are grown on "buffer" layers which are commonly used during high quality film growth. 2) It has been stated in literature that the constant η in Equation 2.18 is experimentally observed to be different than the theoretical value (1.05 vs 0.92) [44]. It is unclear whether this inconsistency is related to the first point, but regardless affects the accuracy of the method.

To circumvent these issues, we use a technique known as the "differential" method to determine the thermal conductivity of thin films. Rather than relying on a numerical model, the observation that the temperature drop across the film is quasi-steady and one-dimensional is invoked. In two separate experiments, the film-of-interest on the substrate (with buffer layers and any required dielectric layers) and a "reference" sample which contains just the dielectric layers, buffer layers, and substrate are measured under the same heat flux conditions ($\Delta T_{total}(\omega)$ and $\Delta T_{ref}(\omega)$ respectively). The difference in temperature between the two experiments is purely due to the presence of the film and the temperature drop across the film is just $\Delta T_f = \Delta T_{total} - \Delta T_{ref}$, so that the thermal conductivity of the film can be determined directly without knowledge of the exact geometry, material properties, or interfaces in the system.

$$k_f = \frac{Pt_f}{Lw\Delta T_f} \qquad 2.26$$

Although ΔT_f is not a function of frequency under the assumptions here, the best practice is to average over a range of frequencies to achieve more certainty and check

for inconsistencies in the assumptions. The differential method serves as the core data reduction technique in this work, except where noted. The few exceptions involve cases where experiment cannot be made to obey the underlying assumption of one-dimensional, quasi-steady conduction within the film. In these cases, experimentally measured transfer functions are fit via non-linear least squared regression to the full equations 2.16 and 2.17. Tong et al. has written an excellent outline for the limits-of-applicability of the differential method [45]. The most common violation of this treatment occurs at high temperature where the thermal conductivity of the substrate is reduced and may be comparable to the film; in this case, heat spreads within the film and the one-dimensionality assumption breaks down. Using the full equations such films can, in principle, still be measured.

Sample Preparation

The 3ω technique requires the existence of a well-defined resistive thermometer on the experimental samples. If the top-most layer of the sample is electrically conducting, then a dielectric layer must also be deposited to maintain a separation; this ensures that heat is deposited uniformly, with quantifiable heat flux in the heaterline. Depending on the thermal stability of the particular material to be measured, I have used different techniques to deposit the dielectric layer: Atomic Layer Deposition of amorphous Al_2O_3 (300°C), Low Pressure Chemical Vapor Deposition of SiO_2(450°C), and Low Temperature Chemical Vapor Deposition of Poly(para-xylene) “Parylene N” (25°C). Generally speaking, Parylene is used for films that are unstable at high temperature while Al_2O_3 is used to make very thin films. The films must be grown thick enough to be pin-hole free; I have found that 50nm Al_2O_3, 200nm SiO_2, and 80nm Parylene are of high enough quality to maintain integrity after the bonding process. Each chapter will specify which method was used.

Microfabrication of the heaterline was accomplished by a lift-off technique (Figure 6). A liftoff resist (LOR-10a), which has the property of etching in developer regardless of its exposure to UV-light, was used as an underlayer (185degC, 5min bake, spun at 5000rpm) followed by a standard I-line resist (95degC, 2min bake, spun at 4000rpm). After exposure to the desired lithographic pattern, a developer (OPD 4262) was used to make a mushroom shaped pattern. Since the TCR of most metals are similar, a number of pure metals and deposition processes are viable at low temperature (<500K); Evaporated and sputtered Au, Al, W, Pd, and Pt have all been verified to make acceptable thermometers. For temperatures up to 800K, sputtered films of Pt (~200nm) with an adhesion layer of Zr (~10nm) are used. However, I have recently found that evaporated and sputtered aluminum are viable alternatives.

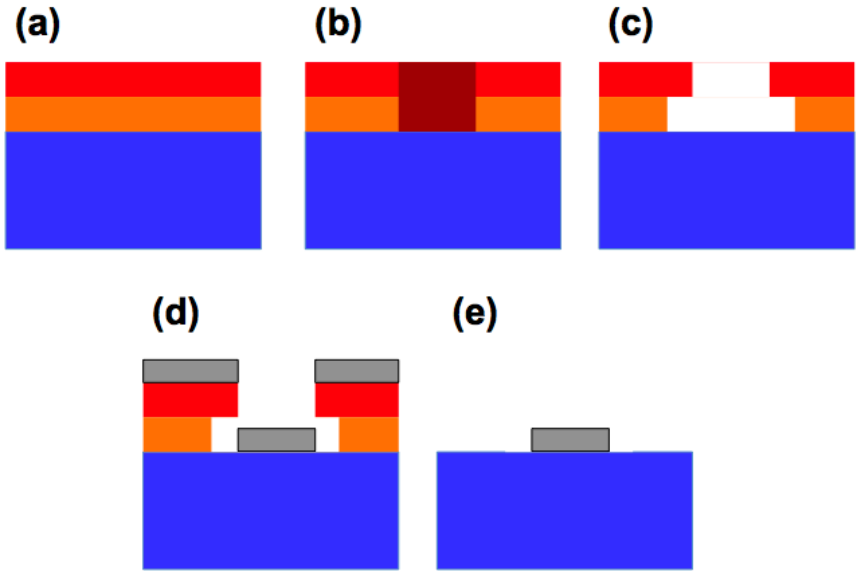

Figure 6 Stages of Liftoff lithography: (a) After bilayer photoresist spinnering, (b) exposure, (c) development, (d) metallization, and (e) lift-off.

Experiments are conducted in under vacuum conditions (~10^{-6} torr) using a wide temperature range cryostage (40K-800K). It is vitally important to obtain an accurate calibrate curve (T vs. R) for the resistive thermometer since much of the accuracy of the overall method depends on the exact knowledge of dT/dR. Our setup uses an E-type thermocouple mounted directly to the surface of the sample to measure the temperature, with accuracy better than 0.5% in the range 70K-800K. The temperature of the sample stage is stabilized for 45 minutes between each measurement. Another important aspect of thermometer calibration is that the properties of the thermometer should not vary with time. For samples that must be measured at high temperature, it is crucial to pre-anneal samples. For measurement to 800K, Zr/Pt heaters are annealed to 600°C for several minutes in a rapid thermal annealing furnace (Ar environment) to achieve a stable morphology before beginning an experiment.

The heaterline geometry can be chosen based on the particular experiment and material combination to minimize experimental measurement uncertainty, as will be discussed in the following section. However, many experiments are insensitive to the exact geometry. A 30μm wide x 1mm long x 200nm thick heater line works well for most films in this work. This is the geometry that has been used, except where noted.

Uncertainty Analysis

In order to design experiments with maximum accuracy, it is desirable to understand the most important sources of error. This section will discuss the major sources of error, estimate the magnitude of the uncertainty, and outline the methods developed to minimize those sources. The section will conclude by discussing the ability of the

method to measure the thermal conductivity tensor in the case of an anisotropic material within the framework of the uncertainty analysis.

In order to deduce thermal properties using the 3ω method, a number of parameters are utilized which each have uncertainty that affect the final results. To estimate the uncertainty in any parameter, f, calculated from uncorrelated parameters x_i, the standard treatment can be used

$$\delta f^2 = \sum_i \left(\frac{\partial f}{\partial x_i} \right)^2 \delta x_i^2 \qquad 2.27$$

In the previous section, it was shown that the thermal conductivity of a substrate can be calculated using

$$k_S = -\frac{P}{2\pi L} \left(\frac{d(\Delta T_{total})}{d(\ln(2\omega))} \right)^{-1}$$

Since Lock-In Amplifiers are very accurate, uncertainties in the voltage $V_{1\omega}$, resistance R, and frequency ω are typically negligibly small. The heater length is also very precise, varying by about 1μm over a 1000μm length. Thus, the only major source of uncertainty is ΔT_{total}, which depends on the heater calibration through Equation 2.8. Thus,

$$\frac{\delta k_S}{k_S} = \frac{\delta(dT/dR)}{dT/dR} \qquad 2.28$$

While the stated accuracy of the thermocouple is better than 0.5%, the uncertainty is amplified when taking the derivative, dT/dR, and can be difficult to estimate is general, particularly in regions of non-linearity. A good approach is to use a statistical analysis based on generalized linear regression. For this purpose, I have developed a scheme to estimate the uncertainty in dT/dR from the covariance matrix associated with the regression coefficients of the polynomial (note that regression coefficients are highly correlated to each other and an equation of the type 2.27 is not correct); the details of this calculation are included in an appendix. The degree of uncertainty varies between experiments depending on the quality of the calibration curve and is a strong function of temperature, being more uncertain at the extreme temperature extents. Often the maximum uncertainty in dT/dR is estimated to be <5% over the entire range of temperatures, leading to the conclusion that for bulk samples, the 3ω technique can be very accurate with uncertainty less than 5%, which equals or exceeds the sensitivity of the more commonly used flash diffusivity technique.

In the case of thin films measured using the differential method, the thermal conductivity is calculated using

$$k_f = \frac{Pt_f}{Lw(\Delta T_{total} - \Delta T_{ref})}$$

Then considering uncertainties in the calibration of the two samples, $(dT/dR)_{total}$ and $(dT/dR)_{ref}$, and the geometry it can be shown that

$$\frac{\delta k_f}{k_f} = \sqrt{\left(\frac{\delta t_f}{t_f}\right)^2 + \left(\frac{\delta w}{w}\right)^2 + \left[\left(\frac{\Delta T_{ref}}{\Delta T_f}\right)\left(\frac{\delta(dT/dR)_{ref}}{(dT/dR)_{ref}}\right)\right]^2 + \left[\left(\frac{\Delta T_{total}}{\Delta T_f}\right)\left(\frac{\delta(dT/dR)_{total}}{(dT/dR)_{total}}\right)\right]^2} \quad 2.29$$

Since $\Delta T_{total} > \Delta T_f$, the pre-factor for the final term is always greater than one, which indicates that the relative uncertainty of the thermal conductivity always exceeds the uncertainty in the heater calibration. If the temperature drop in the reference sample exceeds that of the film, ($\Delta T_{ref} > \Delta T_f$), then the background signal is large with the consequence that the second-to-last pre-factor is also greater than one, which exacerbates the issue. If the temperature drop across the film is much larger than the background, $\Delta T_{ref} << \Delta T_f$, then uncertainties in the calibration of the reference sample become negligibly small. It is clear that the uncertainty in thermal conductivity of thin films will vary depending on the material system under investigation, and therefore no single error estimate can encompass all experiments. However, it is helpful to estimate the uncertainty for an example system. Table 3, summarizes the uncertainty analysis for a film of 2um thick $In_{0.7}Ga_{0.3}Sb$ grown on a GaAs substrate and protected with a 130nm thick dielectric layer of Al_2O_3. This particular film is grown by Molecular Beam Epitaxy (MBE) and thus the thickness is very precisely known; the heater width is kept as wide as is reasonable to minimize uncertainties in the linewidth; the dielectric layer is kept as thin as possible to reduce the background signal from the reference sample. The final result is a total uncertainty of about 12%.

Variable	Nominal Value	Uncertainty (%)	Uncertainty in k (%)
t_f	2μm	20nm (1%)	0.05 W/m-K (1%)
w	30μm	1μm (3%)	0.15 W/m-K (3%)
dT/dR_{total}	20 K/Ω	1 K/Ω (5%)	0.50 W/m-K (10%)
dT/dR_{ref}	20 K/Ω	1 K/Ω (5%)	0.25 W/m-K (5%)
k	5 W/m-K		0.58 W/m-K (12%)

Table 3 **Error estimate for $In_{0.7}Ga_{0.3}Sb$ grown on a GaAs substrate and protected with a 130nm thick dielectric layer of Al_2O_3**

To appreciate the importance good experimental design for the 3ω method, it is instructive to further study the role of the heater calibration. Assuming the relative uncertainty in calibrations is similar from experiment-to-experiment and temporarily neglecting other uncertainties

$$\frac{\delta k_f}{k_f} = \underbrace{\sqrt{\left(\frac{\Delta T_{ref}}{\Delta T_f}\right)^2 + \left(\frac{\Delta T_{total}}{\Delta T_f}\right)^2}}_{\equiv \chi} \frac{\delta(dT/dR)}{dT/dR} \qquad 2.30$$

The prefactor χ quantifies the sensitivity of k to the heater calibration. If the contribution of the background signal is $\alpha \equiv \Delta T_{ref} / \Delta T_f$, then it can be shown that

$$\chi = \sqrt{1 + 2\alpha + 2\alpha^2} \qquad 2.31$$

This function is plotted in Figure 7 for clarity. When the background is large, the sensitivity of the results to the calibration is large, $\frac{\delta k_f}{k_f} \approx \sqrt{2} \frac{\Delta T_{ref}}{\Delta T_{film}} \frac{\delta(dT/dR)}{dT/dR}$

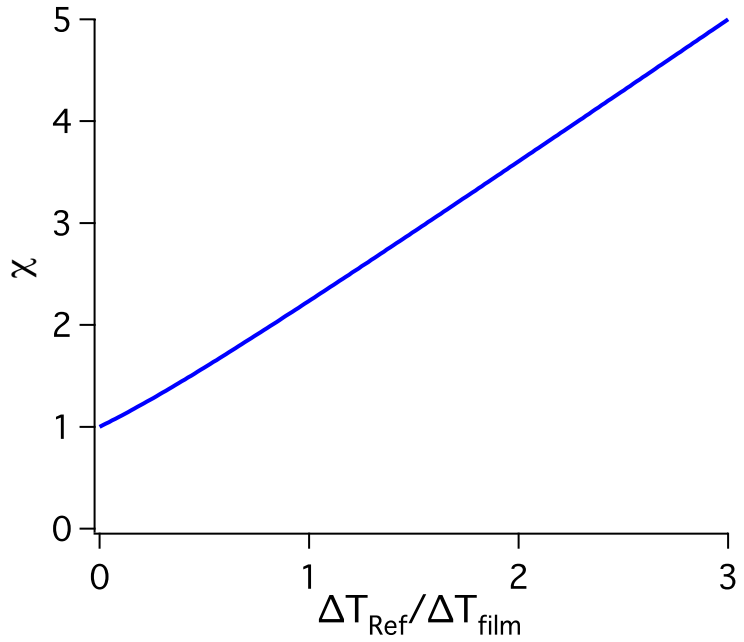

Figure 7 Plot of χ vs α, equation 2.31

While it is important to achieve a very high quality calibration, it is equally important to design experiments to reduce the background signal, ΔT_{Ref}, to acceptable values. To a good approximation, the ratio $\Delta T_{ref} / \Delta T_{film}$ is given by

$$\alpha = \frac{\frac{b}{k_S} + \frac{t_d}{k_d} + \frac{t_b}{k_b}}{\frac{t_f}{k_f}} = \frac{b}{t_f}\frac{k_f}{k_S} + \frac{t_d}{t_f}\frac{k_f}{k_d} + \frac{t_b}{t_f}\frac{k_f}{k_b} \qquad 2.32$$

where the subscripts d and b stand for the dielectric layer and buffer layers respectively. This equation suggests several methods for reducing the uncertainty: 1) Choose a high thermal conductivity substrate when possible ($k_f << k_s$), 2) Use the smallest linewidth possible to reduce the substrate contribution, 3) Use a thick sample film when possible, 4) For all other layers, use the smallest thickness possible. If a value of ~5% for the calibration uncertainty can be obtained, then according to 2.32, with a value of α less than 3, the experiment can achieve accuracy better than 25%. These error estimates generally lead to less uncertainty than previously predicted by Koh [46], primarily because larger error (10%) in the heater calibration is assumed there (without justification); the current estimate of the calibration uncertainty is based on a statistical analysis and thus is expected to be more realistic.

Anisotropic Thermal Conductivity Determination Using 3ω

Having established a method to calculate the experimental uncertainty for the most common 3ω usages, the ability of the 3ω method to be applied to the more advanced application of in-plane measurements will now be examined. This will be done in the context of an uncertainty analysis, which will be the measure of "ability." It will be shown that under optimized conditions, it is possible to measure the in-plane properties of a film, and that the optimal substrate is not necessarily one with high thermal conductivity (as it is for through-plane measurements, see equation 2.32).

While there are well-developed techniques to measure the thermal conductivity of thin films in the through-plane direction (e.g. time domain thermoreflectance and the 3ω method), development of characterization techniques for in-plane transport have proven more difficult. The most widely applied techniques to measure in-plane properties of thin films involve the use microfabricated suspended structures. By suspending the film of interest, the in-plane direction becomes insulated and heat can be forced to move in the plane of the film. This technique was applied recently by Nguyen [47] to study in-plane thermal transport in turbostratically disordered layered compounds. There, a slice of a WSe_2 film was cut by photolithography and placed, using a nanomanipulator, to span between two suspended thermal reservoirs with integrated thermometers. Using DC heating, a temperature gradient was made across the reservoirs, and by carefully accounting for leakage from the reservoirs, the thermal conductivity was determined. Kurabayashi has used a variation of the 3ω method to measure the in-plane properties of spin-coated polyimide films. This was done using TMAH (Tetramethlyammonium Hydroxide) etch to suspend the film across a silicon substrate. Using a heaterline in the center of the gap, 3ω measurements were coupled to a thermal model to determine the in-plane thermal conductivity. While suspension techniques are effective, they are expensive and the etching chemistries are not robust enough to be applied across a wide array of material chemistries.

As an alternative, several groups have considered the possibility of using the 3ω method in the normal geometry (film on a substrate), but using smaller heaterlines to force heat to spread within the film. Kurabayashi has reported the anisotropic measurement of thin-films of spin-coated polyimide using this technique and a finite

element model to account for spreading [48]. Tong [45] developed a new data reduction scheme which used the "differential method" on up to three different sets of samples: 1) a sample and reference with a wide heater, to independently determine through-plane properties and 2) a sample and reference with a heater nearly equivalent in width to the film thickness, which would not undergo one-dimension transport in the film, and 3) a sample with very small film thickness to enhance the role of thermal interface conductance. By coupling measurements to an analytical two-layer anisotropic model, Tong was able to calculate the anisotropic ratio of a Bi/Sb superlattice. In those demonstrations, the optimal sample arrangement and geometries were not discussed. In [48] an error bar of ~30% was estimated (although no justification was given), and in [45] no error bar was given. Given the general utility of this method, it is worth exploring the limits of its application and developing a rationale for optimization.

In the case of anisotropy, it is difficult to calculate the uncertainty using an analytical expression like that of equation 2.27 because the math quickly becomes unwieldy due to the iterative nature of the data reduction (equations 2.16-2.17). However, a completely analogous numerical technique can be used to calculate the errorbars for any experiment as follows. Given that an algorthim exists to fit data to a model, the results can be viewed as a function of the input parameters and experimental data,

$$k = f(\Delta T_i, \omega_i; p, L, t, w, k_s, C_j, b, dT/dR_i, ...) \qquad 2.33$$

where the items to the right of the semi-colon are parameters that must go into the fitting model. While the analytic form of the derivatives of f with respect to all the parameters is difficult to calculate, it is trivial to write a computer code to simulate.

$$\left(\frac{\partial f}{\partial x_i}\delta x_i\right)^2 \approx \left(f\left[x_i + \delta x_i, x_j(j \neq i)\right] - f\left[x_i, x_j(j \neq i)\right]\right)^2 \qquad 2.34$$

Thus the partial sums of δk^2 can be simulated directly using whatever algorithm represents "f". In this case, the algorithm will be the least-squares fit of the model (from 2.16-2.17) to the experimental data. To predict how accurate an experiment will be in the presence of uncertainty in the parameters (e.g. film thicknesses, calibration errors, linewidths), the 3ω curve ("data") can be generated for a set of "true" parameters and thermal conductivities; then the partial sums of the errors, δk^2, can be calculated by varying each of the uncertain parameters. In this way, the effect of uncertainty in each parameter is quantified using 2.34.

The uncertainty analysis is conducted for the specific case of a film with thickness 1μm and thermal conductivities $k_{in\text{-}plane}$=1.8 W/m-K, $k_{through\text{-}plane}$=6.0 W/m-K (to match a planned control experiment). Suppose a data reduction similar to Tong [45] is used. Using a large 20μm wide thermometer the through plane thermal conductivity is decoupled. Then another experiment with a thinner heater (the width of which will be optimized) is used to determine the in-plane portion. The data reduction will be a simultaneous fit to both experiments. I have assumed typical uncertainties in the

experimental parameters (~5% each dT/dR, ~5% linewidths, ~1% filmthickness) and calculated the cumulative error in thermal conductivities under various scenarios.

One important objective of the analysis is to help choose the optimal substrate. In a typical (through-plane) 3ω experiment, it is desirable to make the thermal conductivity of the substrate as large as possible to reduce the background signal (see equation 2.32). However, this is not necessarily the best arrangement when the in-plane thermal conductivity is desired, since then heat does not spread much in the film. Alternatively, when the substrate is chosen to be nearly insulating, heat spreads laterally in the film before being drawn into the substrate.

Contrary to the common wisdom, the results show that anisotropic measurements are more accurate on highly insulating substrates (Figure 8). While either of the limiting cases can be used to measure anisotropic properties, when the thermal conductivity of the substrate is very low, *both* the through-plane and the in-plane conductivities can be measured accurately. In contrast, when $k_{substrate} >> k_y$, through-plane conductivity is significantly more accurate than in-plane conductivity. Note that in this data reduction scheme, the outputs k_x and k_y are anti-correlated and thus the anisotropic ratio, k_x/k_y, is less accurate than the individual k_x and k_y results.

In the two different regimes, $k_x << k_{substrate}$ and $k_x >> k_{substrate}$ the optimal linewidth for the thinner heater is calculated. Figure 9 shows the expected uncertainity as a function of linewidth in the case of $k_{substrate}$ =140W/m-K (Silicon), which was found to be a good value in the $k_x << k_{substrate}$ limit (from Figure 8). In this case, experimental uncertainties grow very large for linewidths greater than the film thickness, and the limiting behavior is not achieved until $w << t_f$. Then, in order to measure thin films, the linewidth should be very small, which would require advanced lithography techniques such as e-beam lithography. In contrast, the expected uncertainty is much less sensitive to linewidth in the other limit $k_x >> k_{substrate}$. If the film were deposited on glass (k=1.2 W/m-K), then the measurement could be made using standard photolithographic techniques and would still achieve excellent accuracy for the in-plane and through-plane conductivities (see Figure 10): both being less than 20% uncertainty.

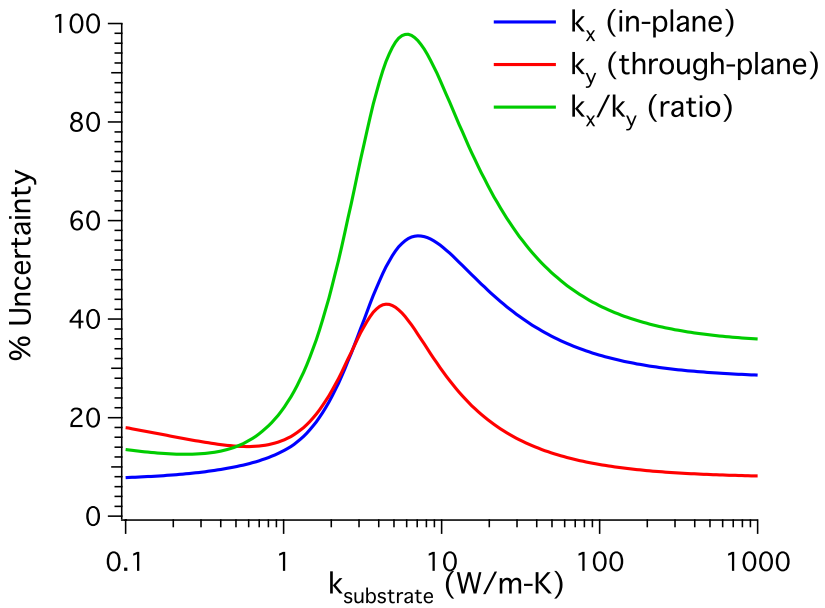

Figure 8 Dependence of the uncertainty in thermal conductivity on substrate thermal conductivity, w=1μm (for film a with k_y=1.8 W/m-K, k_x=6.0 W/m-K, 1μm thick).

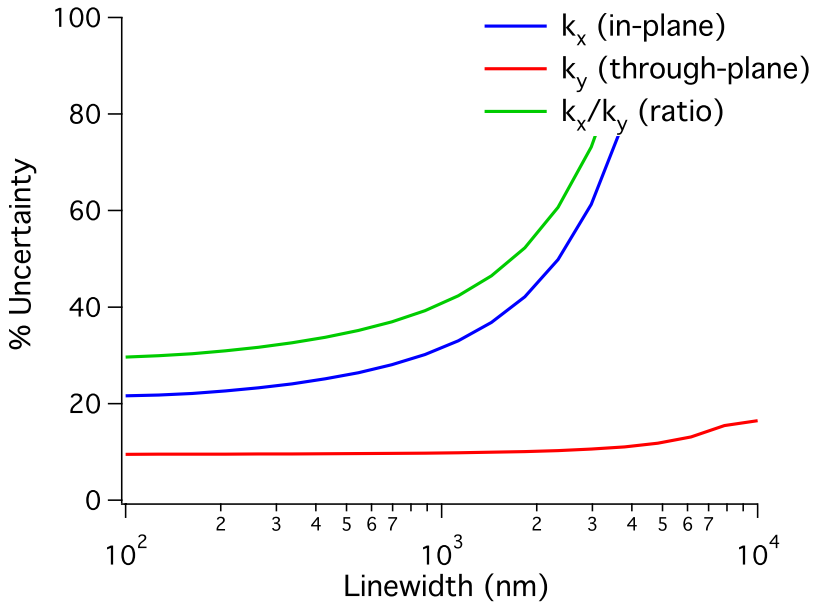

Figure 9 Linewidth dependence of uncertainty for $k_{substrate}$=140 W/m-K

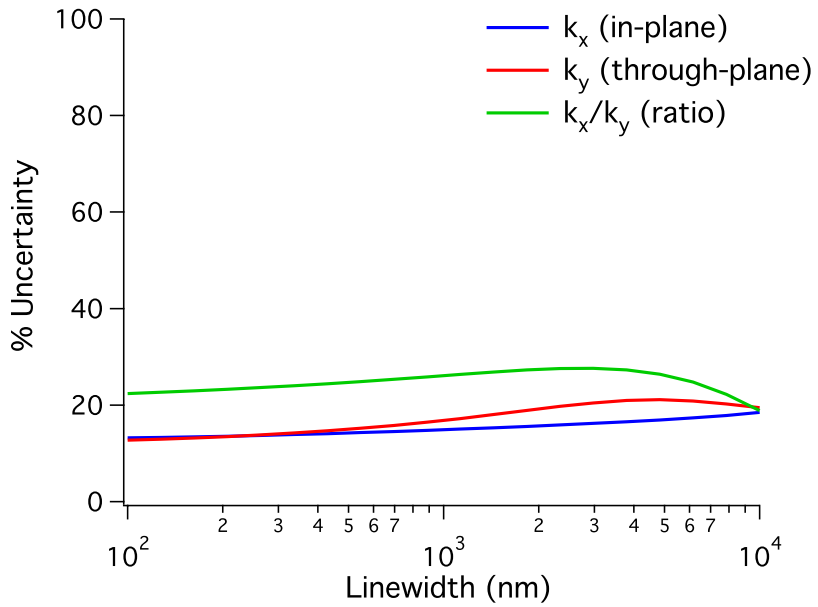

Figure 10 Linewidth dependence of uncertainty for $k_{substrate}$=1.2 W/m-K

In summary, it is possible to measure anisotropic thermal conductivity using the 3ω method. Using a judicious choice of the substrate and heaterline geometry, the method can achieve experimental uncertainties comparable to the state-of-the-art suspension techniques, while using considerably less complicated fabrication procedures that apply to a much wider array of material possibilities. This also suggests that the thermal properties of highly conducting isotropic materials may be measurable by performing in-plane experiments, which would extend the method to the measure metals and hard ceramics, which have previously been considered unsuitable for the 3ω method.

Thermal Transport in Semiconducting Alloys with Embedded Nanostructures

In order to maximize the thermoelectric figure-of-merit, the lattice component of the thermal conductivity should be made to be as low as possible without harming the electrical properties. For decades, the only known method for accomplishing this was to form isovalent alloys of semiconductors, the primary examples being $Sb_{2-x}Bi_xTe_{3-y}Se_y$, $Pb_{1-x}Sn_xTe$, and $Si_{1-x}Ge_x$. This introduces mass disorder on the atomic scale which very effectively scatters phonons; however, because the components are isovalent, charge transport is generally similar in the alloy and thus electric properties remain good, with the caveat that the fundamental band gap is varied and some local strain is generated due to difference in ionic radii. As an example of the effectiveness of alloy scattering, the lattice thermal conductivity for $In_{1-x}Ga_xSb$ at room temperature is shown in Figure 11. There is generally a large range of alloy compositions for which the lattice thermal conductivity of the alloy is less than either pure component, and subsequently there exists a composition with minimum thermal conductivity known as the "alloy limit." Given that mass disorder exists at the smallest possible length scale, it might seem reasonable to believe that this is the best possible arrangement to scatter phonons. However, it can be readily seen the thermal conductivity of most alloys does not correspond to the theoretical minimum for a disordered crystal [49]. For example, $In_{0.5}Ga_{0.5}Sb$ has a measured room temperature thermal conductivity of ~5 W/m-K compared to a computed theoretical limit of ~0.4 W/m-K. Thus, there exists tremendous opportunities for improvement in traditional alloyed materials systems.

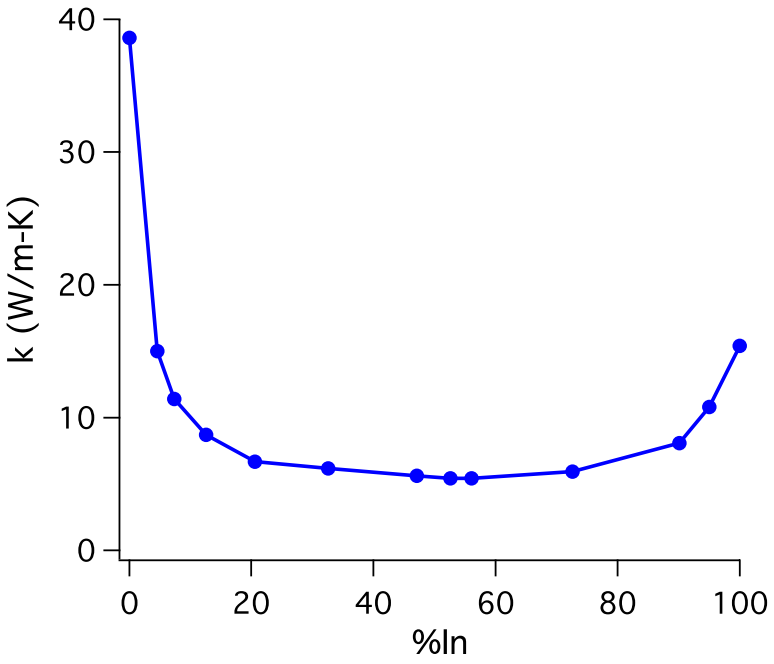

Figure 11 Thermal conductivity of $In_{1-x}Ga_xSb$ alloy as a function of Indium content, showing the "alloy limit." Data is reproduced from [50].

In the previous decade, a number of research groups have demonstrated that the performance of thermoelectric materials can be improved using nanostructures [2, 15-19, 23, 51, 52]. Apart from just a few reports [52, 53], the enhancements have come entirely from increased scattering rates for phonons. One of the most direct studies of this mechanism in nanocomposites was reported by Kim et al. [51]. By introducing a relatively small amount of nanoprecipitates (~0.3% ErAs, ~1-2nm diameter [54]) into a semiconductor alloy ($In_{0.53}Ga_{0.47}As$), the thermal conductivity was reduced to below the "alloy limit." The mechanism for the reduction has been explained based on the strong frequency dependence of phonon scattering in alloys. Since inhomogeneities associated with alloy impurities are on the atomic scale and dominant phonon wavelengths based on the Planck distribution for intensities are on the nanoscale, the scattering from an alloy impurity occurs in the Rayleigh limit ($\lambda >> R$), and therefore scattering cross-section scales as $\sigma \sim R^6 / \lambda^4$. Thus, long wavelength phonons are scattered much less effectively than short wavelength phonons in alloys. It was reasoned that, due to the impurity-size dependence in the Rayleigh limit, the introduction of nanoimpurities increases the effective scattering cross-section and leads to the lower thermal conductivity. Using this concept, we have recently shown that due to a combination of electronic enhancement and lattice thermal conductivity reduction, the figure-of-merit of a more electrically optimized version of this material (0.6% ErAs: $In_{0.53}Ga_{0.38}Al_{0.09}As$) is ZT~1.3 at 800K, making it one of the highest performance n-type thermoelectrics at that temperature [53]. This has led us to pursue an analogous

material, Er-doped $In_{1-x}Ga_xSb$, as a promising p-type analog. The remainder of this chapter will focus on the thermal characterization and modeling of the new p-type system, with the more general goals of further understanding the origins of the lattice thermal conductivity reduction, the limits-of-applicability, and the optimal conditions for the nanostructuring approach; in this sense, the predictions made are broadly applicable to other materials systems as well.

$In_{1-x}Ga_xSb$ with ErSb Embedded Nanocrystals

Rare earth metals are relatively insoluble in III-V materials [55], with solubility ~$10^{17}/cm^3$, well below the typical doping level of most thermoelectrics. Above this level, precipitates of Er-V compounds are generated. ErSb is a metallic compound with the rocksalt crystal structure [56]; it has the special characteristic that the lattice parameter is nearly that of GaSb (6.106 Å vs 6.095 Å), which allows for the epitaxial growth of $In_{1-x}Ga_xSb$ with embedded ErSb precipitates. Similar to our previous reports on ErAs:$In_{1-x}Ga_xAs$ materials [54], our collaborators at UC Santa Barbara observe the spontaneous formation of isolated ErSb nanoparticles in $In_{1-x}Ga_xSb$ with a diameter of ~3-5nm when Er is co-deposited at an overall film growth rate ~1μm/hr (Figure 12) [57]. Conditions controlling the size of the particles are not yet well established, but MBE grown materials are generally kinetically driven, and therefore the size is expected to depend on variables such as growth temperature and deposition rate. When a zincblende material (e.g. GaSb) grows on a rocksalt lattice (e.g. ErSb) there is the possibility of forming twinning defects. Therefore, in order to produce high quality films using the co-deposition method, the zincblende material must template around the rocksalt precipitate, which requires fairly moderate concentrations of precipitate (<10%vol) to avoid an extended blockage of the zincblende phase.

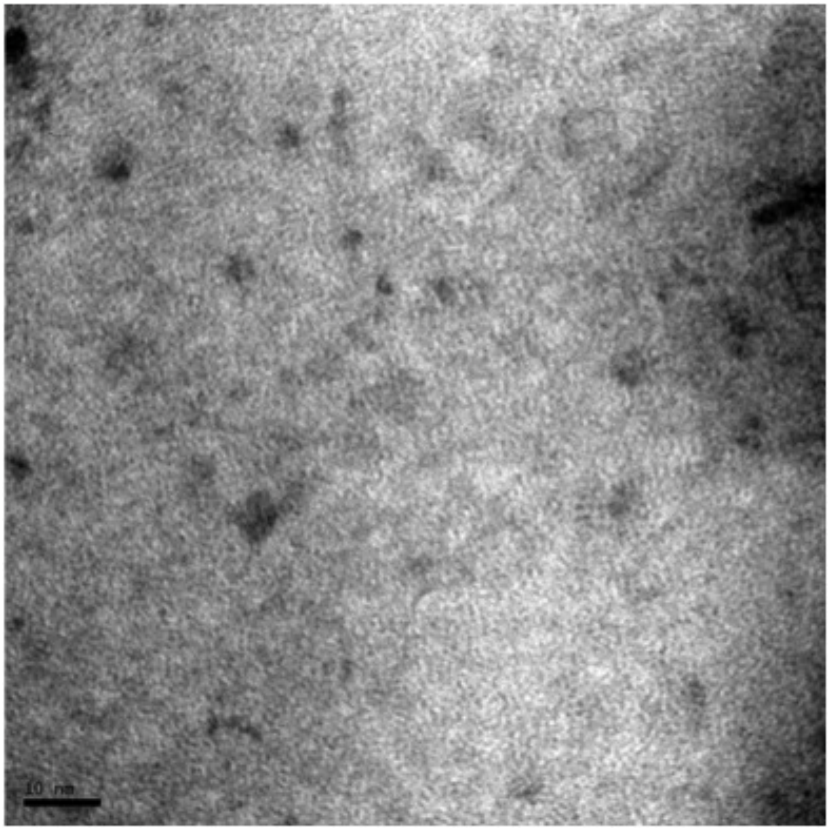

Figure 12 TEM Image showing the formation of ErSb nanocrystal in GaSb. The scalebar at the bottom-left is 10nm.

We have studied the thermal transport of undoped and Er-doped $In_{1-x}Ga_xSb$ films as a function of Indium composition using the 3ω method. Since the optimal doping concentrations for electronic and thermal properties is not yet known, doping levels similar to our best ErAs: $In_{1-x}Ga_xAs$ films (~0.8%ErSb vol) have been used. Our collaborators at UC Santa Barbara grew 2μm thick films of ErSb: $In_{1-x}Ga_xSb$ on semi-insulating GaAs substrates. A 200 nm thick GaAs buffer was grown at a substrate temperature of 600 ºC followed by a 50 nm thick GaSb buffer layer grown at a substrate temperature of 530 °C for all the samples to relief the strain and smooth the surface. The strain between the antimonide epi-films and the arsenide substrates was relieved by periodic misfit arrays [51] formed during the interface adjustment. Both As_2 and Sb_2 were used from valved As and Sb crackers, respectively. For the growth of the ErSb:$In_xGa_{1-x}Sb$ nanocomposites the substrate temperature was reduced to 500 °C. For thermal characterization, we then covered the films with a dielectric layer of 130nm Al_2O_3 by atomic layer deposition or 200nm SiO_2 by low-pressure chemical vapor deposition, fabricated a resistive thermometer, and measured the thermal conductivity from 40K – 800K. At high Indium concentration's ($x<0.5$), the melting point of the alloy is reduced, and thus high temperature measurements were avoided. The resistive thermometers were 30μm wide x 1000μm long x 200nm thick Pt (with thin Zr adhesion layer) and were annealed beyond the maximum experimental temperature prior to

measurements. Data was analyzed using the differential method [42], but corrected to account for minor spreading effects that occur at high temperature.

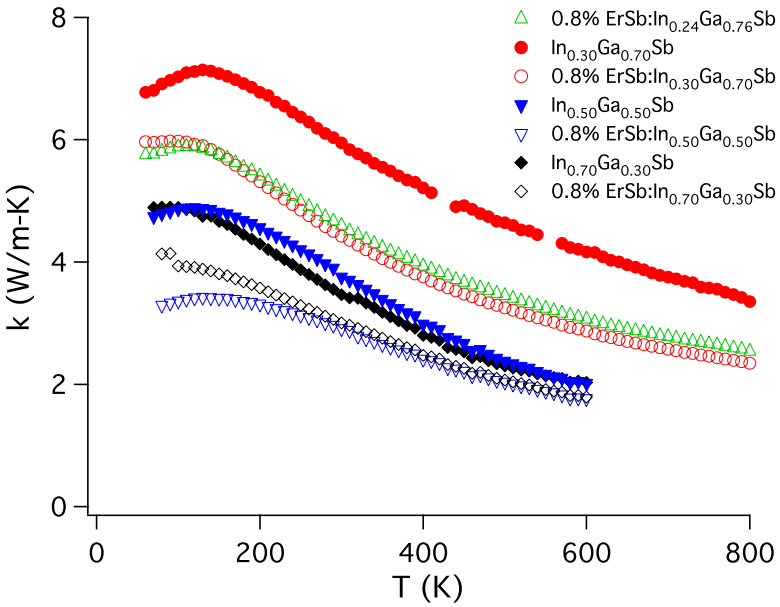

Figure 13 Measured thermal conductivities of Er-doped and undoped $In_{1-x}Ga_xSb$ films grown on GaAs.

The experimental data confirms that the introduction of nanostructural defects can help materials go below the alloy limit; a mere 0.8%vol ErSb reduces the thermal conductivity of the most heavily alloyed $In_{0.5}Ga_{0.5}Sb$ films by ~24% below the alloy limit at room temperature. The results are shown in Figure 13. Each of the Er-doped films display lower thermal conductivities than the corresponding undoped alloys over the entire range of temperatures. We have measured the thermal conductivity of pure ErSb at room temperature and found that it is very high (>10W/m-K) and thus the reduction in conductivity cannot be explained on the based on a model that does not take into account the change in microscale physics. Note that the effect at high temperature is far more modest. To understand why this should happen, and how to further optimize the material it is helpful to employ Boltzmann transport modeling, which will be outlined in the following section.

Transport Modeling of Nanoparticle-in-Alloy Systems

In what follows, the phonon component to thermal conductivity is analyzed on the basis of the Callaway model [11]. In the Callaway model, the thermal conductivity may be written as

$$k = \frac{k_B}{2\pi^2 v}\left(\frac{k_B T}{\hbar}\right)^3 \left(I_1 + \frac{I_2^2}{I_3}\right) \qquad 3.1$$

where

$$I_1 = \int_0^{\Theta_D/T} \frac{\tau_c x^4 e^x}{(e^x - 1)^2} dx \qquad 3.2$$

$$I_2 = \int_0^{\Theta_D/T} \frac{\tau_c}{\tau_N} \frac{x^4 e^x}{(e^x - 1)^2} dx \qquad 3.3$$

and

$$I_3 = \int_0^{\Theta_D/T} \frac{1}{\tau_N} \left(1 - \frac{\tau_c}{\tau_N}\right) \frac{x^4 e^x}{(e^x - 1)^2} dx \qquad 3.4$$

Here v is group velocity averaged over the longitudinal and transverse phonon modes, Θ_D is the Debye temperature, τ_N is the scattering time due to the normal phonon-phonon scattering process, and τ_c is the combined scattering time when all possible processes are considered, which is calculated from Matthiessen's rule.

$$\tau_c^{-1} = \tau_N^{-1} + \tau_U^{-1} + \tau_B^{-1} + \tau_{alloy}^{-1} + \tau_{nc}^{-1} \qquad 3.5$$

The subscript's above indicate the scattering rates for Normal phonon-phonon, Umklapp phonon-phonon, boundary, alloy impurity, and nanocrystal processes, respectively. Physically, the Callaway model is an implementation of Boltzmann transport modeling that accounts for the fact that, although the Normal phonon-phonon scattering processes do not alter the overall momentum of phonons and thus cannot alone alter the thermal conductivity, they are a still responsible for the restoration of momentum of the individual phonons to the equilibrium distribution. The typical expression for the Normal processes is

$$\tau_N^{-1} = B_N \omega^2 T^3 \qquad 3.6$$

There is no universally excepted form of the Umklapp scattering rate, but one popular form is

$$\tau_U^{-1} = B_U \omega^2 T e^{-\Theta_D/nT} \qquad 3.7$$

The phenomenological constants B_N, B_U, and n are obtained by a fit to the measured temperature dependent thermal conductivity of unalloyed, single crystals of GaSb and InSb (Figure 14). To approximate the phonon-phonon scattering of any intermediate a composition weighted average is taken. The alloy scattering is modeled as

$$\tau_{alloy}^{-1} = A \frac{x(1-x)\omega^4}{v_x^3} \qquad 3.8$$

In principle, the constant A could be estimated from the model proposed by Abeles [58].

$$A = \frac{\delta^3}{4\pi}\left[\left(\frac{\Delta\rho}{\rho}\right)^2 + \epsilon\left(\frac{\Delta\delta}{\delta}\right)^2\right] \quad 3.9$$

where δ is the lattice constant, ρ is the density, and ε~45 is a phenomenological constant.

$$\Delta\delta = \delta_{GaSb} - \delta_{InSb} \quad 3.10$$

$$\Delta\rho = \Delta\rho_{GaSb} - \Delta\rho_{InSb} \quad 3.11$$

$$\delta = x\delta_{GaSb} + (1-x)\delta_{InSb} \quad 3.12$$

$$\rho = x\rho_{GaSb} + (1-x)\rho_{InSb} \quad 3.13$$

However, here the constant, A, has been obtained directly from a fit of the room temperature thermal conductivity as a function of composition (k vs x, at fixed T). Typically, boundary scattering is unimportant for these films but the expression

$$\tau_B^{-1} = v_x / L_B \quad 3.14$$

has been adopted with a value equal to the film thickness assumed for L_B (2μm).

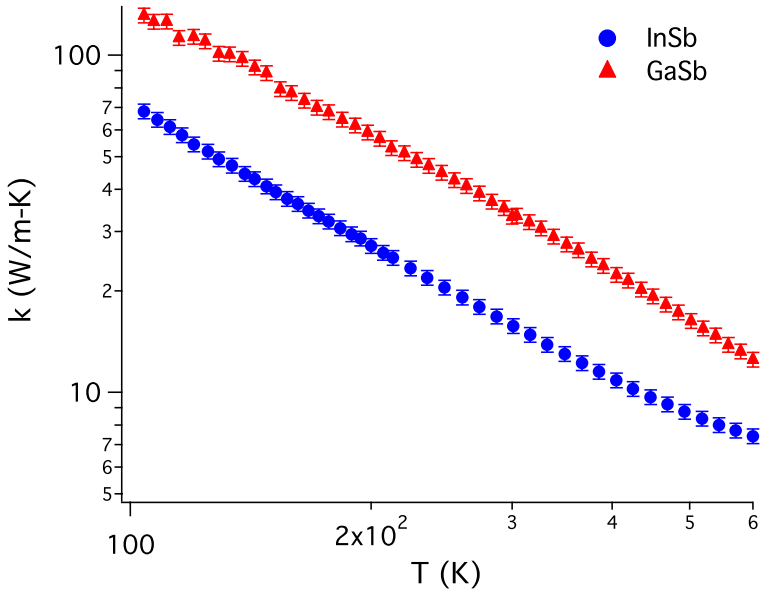

Figure 14 Bulk thermal conductivity of undoped GaSb and InSb measured from commercially obtained single crystals.

In order to model the effect of nanocrystalline impurities, a modified version of theory developed by Kim [59] was used. Kim derived explicit analytical expressions for the scattering cross sections in the Rayleigh and near-Geometric limits. A quantum mechanical perturbation method was applied to find the Rayleigh limit for scattering from a spherical impurity.

$$\frac{\sigma_{Rayleigh}^{-1}}{\pi R^2} = \chi^4 \left[\frac{\alpha^2}{4}\left(\frac{\Delta\rho}{\rho}\right)^2 + 3\alpha^8 \left(\frac{\Delta K}{K}\right)^2 \frac{\sin^4\left(\frac{\alpha|q|\delta}{2}\right)}{\left(\frac{\alpha|q|\delta}{2}\right)^4} \right] \times \left\{ \frac{\pi\left[\cos(4\chi) - 1 + 4\chi sin(4\chi) + 32\chi^4 - 8\chi^2\right]}{16\chi^6} \right\} \quad 3.15$$

The near-geometric limit was obtained using the van de Hulst theorem from optics [60].

$$\frac{\sigma_{geometric}^{-1}}{\pi R^2} = 2\left(1 - \frac{\sin\left[2\chi\left(\frac{q'}{q} - 1\right)\right]}{\chi\left(\frac{q'}{q} - 1\right)} + \frac{\sin^2\left[\chi\left(\frac{q'}{q} - 1\right)\right]}{\left[\chi\left(\frac{q'}{q} - 1\right)\right]^2} \right) \quad 3.16$$

where

$$\frac{q'}{q} - 1 = \frac{\sqrt{1 + \frac{\Delta\rho}{\rho}}}{\sqrt{1 + \frac{\Delta K}{K}}} - 1 \quad 3.17$$

The quantity δ is the distance between neighboring lattice sites, and thus the term containing it is typically small and negligible. The term $\chi = qR$ is a non-dimensionalized wavevector called the "scattering parameter." For χ>>1 the wavelength is smaller than the particle and the geometric limit applies; for χ<<1 the wavelength is larger than the particle and the Rayleigh limit applies. The two limits have been combined using Matthiessen's rule to bridge the two regimes.

$$\sigma_{nc}^{-1} = \sigma_{Rayleigh}^{-1} + \sigma_{geometric}^{-1} \quad 3.18$$

The nanocrystal impurity scattering cross-section based on these expressions has been plotted in Figure 15 using $\Delta\rho / \rho = 0.5$ and $\Delta K / K = 0.9$, which corresponds to ErSb embedded in a matrix of $In_{0.5}Ga_{0.5}Sb$. While the approximation used to derive 3.16 accurately captures the cross section oscillations from Mie theory, it underpredicts the cross section in the intermediate range that is of great importance for the thermal modeling. On the other hand, it has been shown that when slight polydispersity is

present, the oscillations for the average cross section become washed-out and thus become unimportant. Given this, a simplified version of these equations is used that maintains the extremal limits while ensuring a more accurate intermediate regime, but loses the oscillations that would occur in the presence of monodisperse particles. To a very good approximation, equation 3.15 can be written as

$$\frac{\sigma_{Rayleigh}}{\pi R^2} = \frac{2\pi}{9}\left(\left(\frac{\delta\rho}{\rho}\right)^2 + \frac{3}{2}\left(\frac{\delta K}{K}\right)^2\right)\chi^4 \qquad 3.19$$

in the low χ regime. Likewise, neglecting the oscillations in equation 3.16, the expression simplifies to the limit of

$$\frac{\sigma_{geometric}}{\pi R^2} = 2 \qquad 3.20$$

Approximations 3.19 and 3.20 are combined using equation 3.18 to calculate the scattering times associated with nanoparticle scattering.

$$\tau_{nc}^{-1} = \eta\sigma_{nc}v \qquad 3.21$$

where η is the number density of nanocrystals. Mingo [61] has recently used a similar expression to model metal-silicide nanocrystals in $Si_{1-x}Ge_x$, but only included the effect of mass contrast. It can be readily seen from equation 3.19 that the effect of elastic mismatch is ~5 times larger than mass contrast in the case of ErSb nanocrystals in $In_{1-x}Ga_xSb$, and thus must be included to make accurate predictions. Using the model above, we have simulated the thermal transport behavior of the ErSb:$In_{1-x}Ga_xSb$ systems under a variety of conditions, which gives fundamental insight into the physics of nanostructured systems and provides a path toward optimization of nanocomposites for thermoelectric applications.

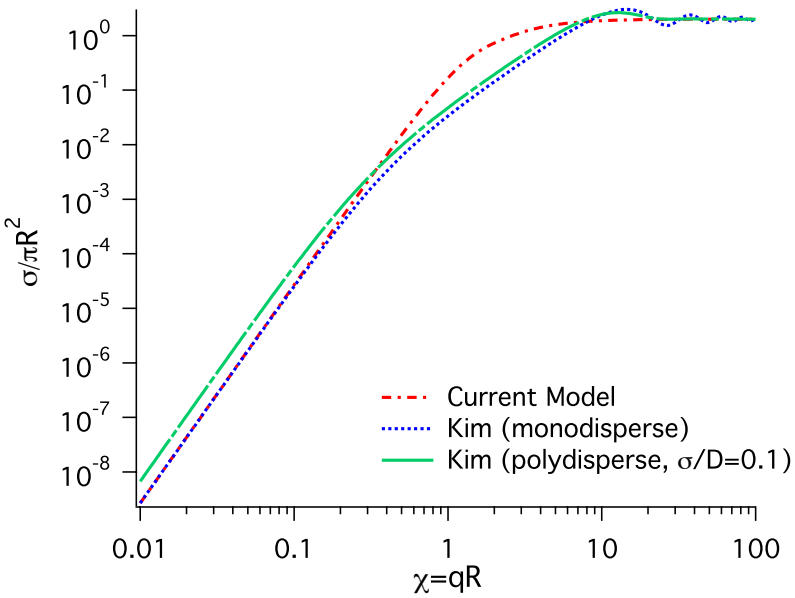

Figure 15 Scattering cross-section of embedded nanocrystals predicted by various models. Last two curves used the model of [59].

A typical spectrum of phonon scattering rates is shown in Figure 16 for the case of $In_{0,5}Ga_{0.5}Sb$ at 300K with 1%vol ErSb embedded nanocrystals (d=4nm). Despite the fact that nanocrystals only increase the scattering rate at low-to-medium frequencies, which constitute a minority of the phonon radiative intensity in the material, they have a profound impact on thermal transport. This is because alloy scattering is so efficient at high frequency that long wavelength phonons contribute substantially to transport. Figure 17 shows the cumulative thermal conductivity of $In_{0,5}Ga_{0.5}Sb$ before nanocrystal impurities are introduced. Over half of the thermal conductivity can be attributed to phonons with frequency less than 1THz.

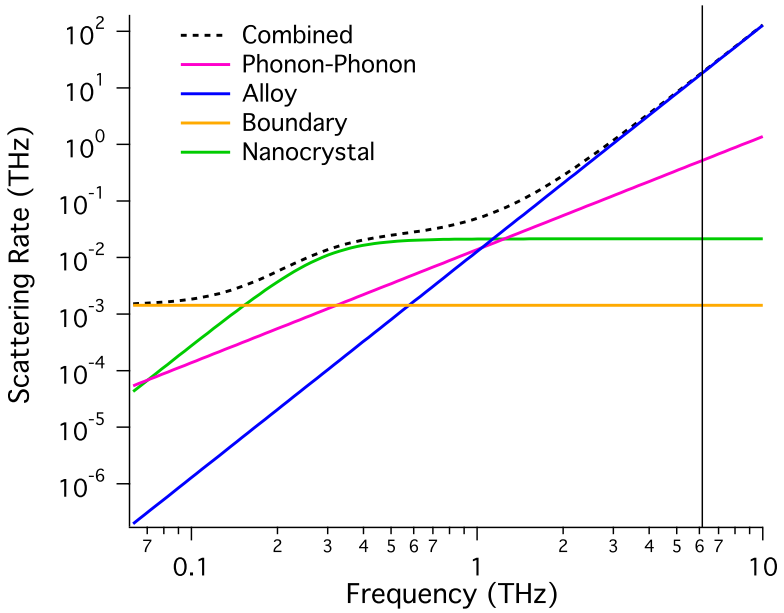

Figure 16. Model of scattering rates for phonons in $In_{0.5}Ga_{0.5}Sb$ with 1%vol ErSb nanocrystals 4nm in size at 300K. The solid, vertical black line represents $\omega = k_B T / \hbar$, below which phonons are excited.

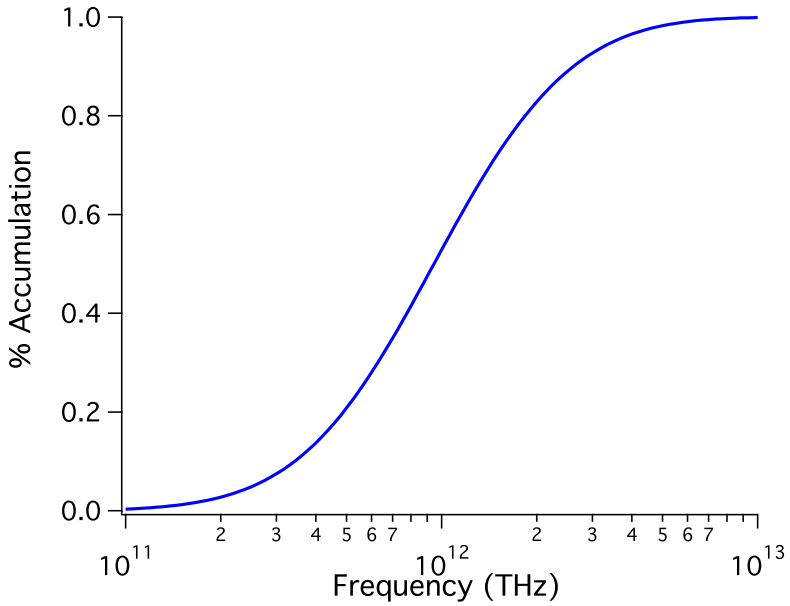

Figure 17. Cumulative thermal conductivity of $In_{0.5}Ga_{0.5}Sb$ (no ErSb) @ 300K computed from Callaway model. Half of the thermal conduction comes from phonons with frequency <1 THz, corresponding to a mean-free-path of ~100nm.

One important aspect of phonon transport in nanostructured alloys is the amount of nanocrystalline impurities required to observed a thermal conductivity reduction. Practically speaking, it is often desirable to keep the amount low in order to maintain

good electrical mobility, although with careful band alignment design this can be improved. It is clear that in order for nanostructuring to affect thermal transport, the scattering rate of nanocrystals should be greater than that of all other mechanisms at least in some frequency range important to transport. For a given nanocrystal size, the scattering rate increases proportional to the volume fraction and eventually can exceed that of phonon-phonon and boundary scattering at low frequency. At the crossover, thermal reductions begin. Figure 18 shows the predicted dependence of thermal conductivity as a function of volume fraction of ErSb (d=4nm) embedded in $In_{0,5}Ga_{0.5}Sb$. At room temperature, a very small amount of material (~0.1%vol ErSb) is required to achieve improvements. By 10%vol ErSb, nanocrystalline scattering dominates over a very large range of frequencies and the thermal conductivity is expected to be lowered by ~70% relative to the non-nanostructured alloy. In contrast, at higher temperatures, the dominant phonons shift to higher frequencies where alloy scattering and phonon-phonon processes are more important, thus the threshold volume fraction required to reduce conductivity is higher. This temperature effect explains the reason that the thermal conductivity of undoped $In_{0,5}Ga_{0.5}Sb$ comparable to the 0.8%vol ErSb doped films at high temperature in Figure 13.

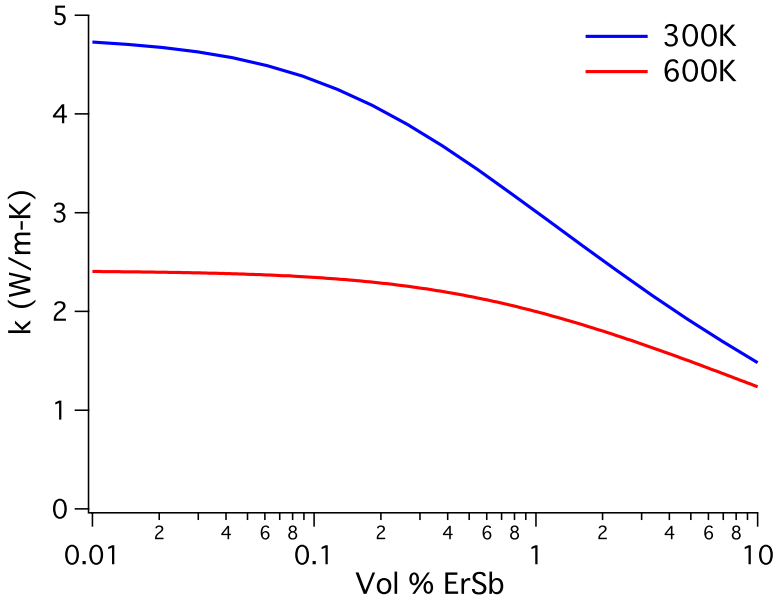

Figure 18 Predicted dependence of the thermal conductivity on Er doping concentration for $In_{0.5}Ga_{0.5}Sb$ @ 300K and 600K based on Boltzmann transport theory.

In the long-wavelength limit, it is clear from equation 3.19 that the scattering cross section scales very favorably with nanocrystal size (~R^6) which makes scattering from a nanocrystal orders of magnitude more intense than from an isolated impurity. This would seem to indicate that very large particles are desirable (perhaps not even "nano"). Mingo has outlined a helpful thought experiment which explains why the nanoscale is desirable [61]: Suppose that one has a fixed volume of impurties to

distribute in a material. The impurities can be clustered to form large particles or more isolated to achieve higher number density of particles. The scattering rate scales like $\tau^{-1} \sim \eta\sigma$ and the number density of particles scales like $\eta \sim 1/V_p$, where $V_p = 4/3\pi R^3$ is the volume of each particle. Then in the long wavelength limit, the scattering rate scales like

$$\begin{aligned} \tau^{-1} &\sim \left(\frac{1}{V_p}\right)\left(R^6\right) \\ &\sim \left(\frac{1}{V_p}\right)\left(V_p^2\right) \\ &\sim V_p \end{aligned} \qquad 3.22$$

Again, this would seem to indicate that larger particles are better for scattering. However, the short wavelength limit gives the opposite result since in that case $\sigma \sim R^2$.

$$\begin{aligned} \tau^{-1} &\sim \left(\frac{1}{V_p}\right)\left(R^2\right) \\ &\sim \left(\frac{1}{V_p}\right)\left(V_p^{2/3}\right) \\ &\sim V_p^{-1/3} \end{aligned} \qquad 3.23$$

Thus, scattering rate for phonons actually decreases once the particle size becomes large enough to be described by geometric scattering. This thought experiment indicates two things: there should exist an optimal particle size for a given volume fraction of impurties and this minimum should exist near the dominant wavelength of phonons which represents the transition from “long” to “short” wavelength phonons. For most materials, this occurs in the very low nanoscale region near room temperature (1-10nm). This argument is slightly complicated by the fact that other scattering mechanisms co-exist in real materials. We have simulated the behavior of nanostructured III-V alloy materials and have found that indeed, an optimal nanocrystal size should exist. Near room temperature the effect is very pronounced. Figure 20 shows the diameter dependence at room temperature for $In_{0.3}Ga_{0.7}Sb$ doped with 1%vol and 10%vol ErSb.

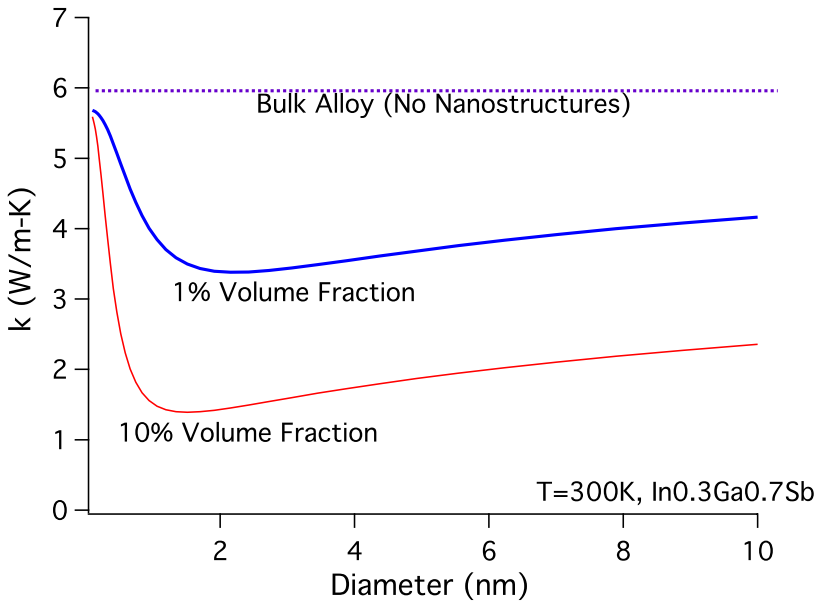

Figure 20 Dependence of the thermal conductivity of Er-doped In0.3Ga0.7Sb on nanocrystal size.

While the optimal particle diameter for this material is found to be near 2nm, it depends on a number of parameters such as alloy content, temperature, volume fraction of nanostructures. Temperature has the effect of decreasing the overall importance of nanostructure scattering, but also shifts the dominant wavelengths to higher frequency, which requires smaller particles to optimize transport. Alloy content also plays an important role. Near the alloy limit, high frequency phonons are scattered very efficiently already. Nanoparticles should then be designed to scatter longer wavelength phonons, despite the fact that shorter wavelength phonons may dominate the intensity spectrum. Figure 19 shows a contour plot of thermal conductivity as a function nanocrystal size and matrix alloy composition for 1%vol ErSb. The thermal conductivity shows a broad global minimum near composition of $In_{0.6}Ga_{0.4}Sb$ with ~3nm particle diameter. Experimentally measured thermal conductivities on sample near this global minimum (Figure 13) are in very good agreement with the predicted value and thus likely represent the optimized arrangement for this volume fraction.

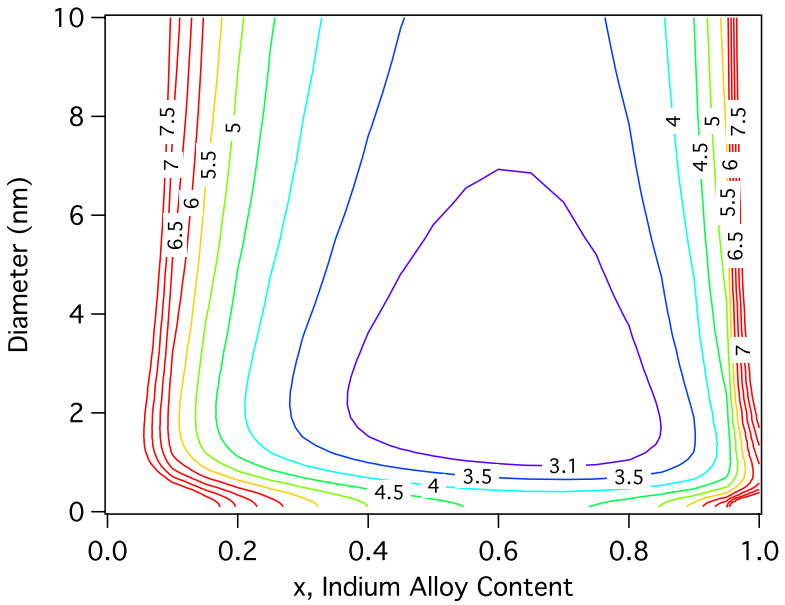

Figure 19 Thermal conductivity as a function of alloy composition, x, and nanocrystal diameter at 300K for fixed ErSb concentration (1% Vol).

Using existing growth techniques, it is very difficult to prepare model systems that explicitly demonstrate the existence of the minimum. Layer-by-layer growth techniques typically have little control over nanocrystal size on this length scale, and with the current material system, the parameters governing nanocrystal size remain poorly understood. This is one of the primary motivations for exploring colloidal nanostructures as a route to nanostructured solids (this will be the subject of the remaining chapters). In that case, the size of nanocrystals can be controlled with extreme precision, but the ability to make high quality matrix materials is extremely limited. Thus, to date, no group has directly observed this effect during experiments and it remains an outstanding research topic.

Several topics remain outstanding in the thermal transport for this type of nanocomposite. The direct observation of an optimal nanocrystal size is prime among them. However, another important issue is the study of highly dense nanostructures. In the current model, we have included the effect of nanocrystals by modeling only scattering, and we have modeled such scattering as independent/random events. When elastic scattering events occur more often than inelastic (phonon-phonon) events, coherence can be maintained between scattering, and thus multiple-scattering should be accounted for; such events have been linked to localization in other particle systems [62], and may prove to be an intriguing research topic for phonon transport. In addition, it is clear that if the volume fraction of the second phase becomes large, the overall material should eventually converge to the properties of the second phase. Thus, a new approach to modeling should be developed, which can account for these phenomena, perhaps based upon a mean-field approach. In has been recently hypothesized that nanocomposites based on TbAs:$In_{1-x}Ga_xAs$ will maintain excellent

electrical transport at high volume fractions of TbAs (>10%); understanding the optimal thermal transport conditions for a system of this type will require a more careful treatement of phonon in dense nanostructures.

In summary, we have demonstrated that the nanostructured p-type system ErSb:$In_{1-x}Ga_xSb$ displays thermal conducting below the alloy limit. Boltzmann transport theory predicts that as little a 0.1% ErSb can accomplish this. Using higher loadings it should be possible to create composites that approach the theoretical lower limit for thermal conductivity. We have also predicted the existence of an optimal nanostructure size.

Enhanced Thermopower in Quantum Dot Superlattices

While improvements in ZT for nanostructured materials have generally been attributed to reductions in thermal conductivity [63, 64], the unique electronic structure of low dimensional materials can also have a strong impact on thermopower and charge transport. Colloidal synthesis of monodisperse nanocrystals could offer a convenient route to low-cost and production-scalable low-dimensional thermoelectric materials. Moreover, chemical synthesis allows precise tuning of the nanocrystal size in sub-10 nm range typically inaccessible for molecular beam epitaxy grown quantum dots [65]. This opens up the possibility to explore thermoelectric properties of strongly quantum-confined materials. In this regime the valence and conduction bands of a semiconductor collapse into well separated discrete energy states [64, 66, 67], which alters fundamental properties of a semiconductor such as the electronic density of states (DOS) and band gap energy [64, 66, 67]. Quantum confinement leads to sharp delta-function-like peaks in the DOS, which is predicted by Mahan and Sofo [68] to be the best possible electronic structure for a thermoelectric material. Recent calculations by Humphrey and Linke [69] predict that optimized nanostructured materials with a delta-like DOS should have ZT approaching 10 at room temperature. This exciting prediction originates from the fundamental difference between thermodynamics and transport in nanostructured materials as compared to bulk thermoelectric materials [69]. It is also anticipated that these materials will have advantageous thermal properties because the nanocrystal diameters are much smaller than the phonon mean free path (~10^{-7} to 10^{-8} m for crystalline materials at room temperature) [70, 71]. This causes a strong suppression of thermal conductivity due to phonon scattering at the nanocrystal boundaries [72, 73]. In our work this extreme regime is realized by using PbSe nanocrystal superlattices with varying nanocrystal sizes.

Charge transport in an array of close packed semiconductor nanocrystals separated by thin barriers can occur by hopping between quantum confined orbitals with S and P symmetry [74, 75]. To date, arrays of lead chalcogenide nanocrystals show the most promising charge transport properties. This is due to their monodispersity and eight-fold degeneracy of 1S electron and hole states that allows good energy level alignment between adjacent particles, leads to sharp peaks in the electronic DOS, and provides a very large number of electronic states available for charge transport [26]. The extraordinarily large static dielectric constant of PbSe (ε~250) brings down the charging energy and prevents Coulomb blockade in PbSe nanocrystal solids [26, 76]. Talapin [26] has demonstrated that engineering interparticle spacing allows tuning of the exchange coupling energy and can increase carrier mobility in self-assembled superlattices of PbSe nanocrystals by many orders of magnitude approaching >1 cm^2/Vs. Ultimately, further increases of quantum mechanical coupling between individual nanocrystals packed into a long-range ordered superlattice should lead to high-mobility Bloch transport through three-dimensional minibands [77]. Lastly, bulk lead chalcogenides are widely used in commercial thermoelectric devices due to the combination of S, σ and k parameters naturally favoring large values of ZT.

Size Dependant Thermopower Measurements of PbSe Quantum Dot Superlattices

PbSe nanocrystals of different size were synthesized by reacting lead oleate with tri-n-octylphosphine selenide in squalane in the presence of oleic acid capping ligands [18]. We varied the size of the nanocrystals from ~4.3 nm to ~8.6 nm while keeping the size distribution well below 10%. The narrow size distribution allows resolution of the sharp excitonic features in the absorption spectra of the colloidal solutions and can also be seen in the transmission electron microscopy images (Figure 20a). Prior to nanocrystal film deposition, glass substrates were treated with hexamethyl disilazane (HMDS) to improve wetting properties. Films of monodisperse PbSe nanocrystals were deposited by drop-casting hexane:octane (~9:1 by volume) solutions on substrates with pre-formed parallel Au/Cr electrodes (Figure 20b). The resulting film thickness was generally 50 – 200 nm. The PbSe nanocrystals are initially coated with oleic acid ligands. After drop-casting, the oleic acid is removed by hydrazine treatment as described in [26]. Hydrazine molecules replace oleic acid at the nanocrystal surface, which reduces the inter-particle spacing from ~1.1 nm down to 0.4 nm and results in greatly improved electrical conductivity. Hydrazine treatment does not change nanocrystal size and shape (Figure 20c); treated nanocrystal films possess characteristic excitonic features in the absorption spectrum [26].

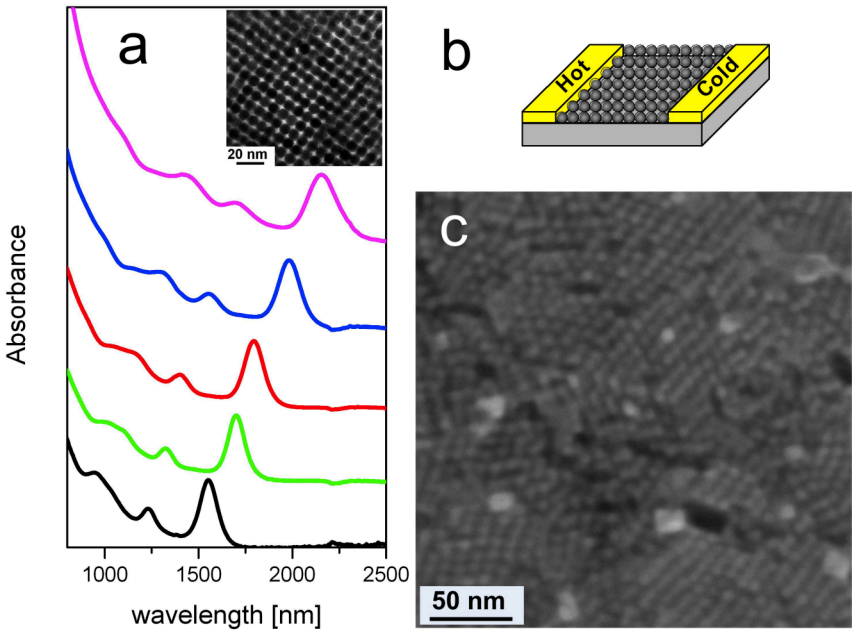

Figure 20 (a) The absorption spectra of PbSe nanocrystals dispersed in tetrachloroethylene. The diameters are 4.8 nm (black), 5.6 nm (green), 6.4 nm (red), 7.1 nm (blue), and 8.6 nm (pink). The electronic structure of PbSe depends on the particle size due to quantum confinement. The inset shows transmission electron microscopy image of PbSe nanocrystals with diameter ~ 7.1 nm. (b) The measurement device consisted of a glass wafer with two Au/Cr electrodes. (c) Typical high resolution scanning electron microscopy images of a conductive PbSe nanocrystal film used in this study.

Unless otherwise stated, all nanocrystal superlattices were kept inside a dry-nitrogen glove box during storage and measurements. Temperature gradients for the thermopower measurements were created with commercially available thermoelectric devices. Voltages and temperatures were measured with an Agilent 34401a voltmeter and thermocouples, respectively. The temperature gradient was modulated by varying the electrical current to the thermoelectric devices. After hydrazine treatment, the thermopower and conductivity of the nanocrystal film exhibited a strong time-dependence that asymptotes. We attribute this time-dependence to the changes in hydrazine concentration in the nanocrystal solid. The length of this transience increased for smaller nanocrystal sizes and generally varied between 1 – 15 days. Unless otherwise indicated, the data presented is taken at the asymptote of this transience.

When a temperature gradient, ($|\Delta T|$=0-30K) is created across the nanocrystal film, an open circuit voltage V_{oc} proportional to the temperature gradient is observed (Figure 21a). The Seebeck coefficient is given by $-dV_{oc}/dT$ (e.g. a positive Seebeck coefficient implies that the cold region develops a higher potential than the hot region). The dependence on nanocrystal size for thermopower is shown in Figure 21b. As the

nanocrystal size decreases from 8.6 nm to 4.8 nm, the thermopower increases from 700 to 1150 μV/K. The positive sign of thermopower indicates that transport in these films is p-type. A combination of electrical conductivity and field-effect transistor measurements provide insight into these thermopower results. Over the same nanocrystal size range, we observed a drop in electrical conductivity by about one order of magnitude (Figure 21c). Field-effect hole mobility was ~ 0.l cm^2/V-s and no nanocrystal size dependence was observed (Figure 22). Using the mobility data we can calculate the carrier concentration in our nanocrystal solids since $\sigma = ne\mu$, where μ is the mobility, e is the electron charge, and n is the carrier concentration. Simple estimates yield ~0.2 carriers/dot for the 8.6 nm nanocrystals and ~0.002 carriers/dot for the 4.3 nm nanocrystals. For comparable carrier concentrations, the PbSe nanocrystal solid exhibits a significant thermopower enhancement of several hundred μV/K relative to bulk PbSe [78]. This enhancement in thermopower is a signature of the sharper peaks in the nanocrystal solid DOS relative to the bulk DOS.

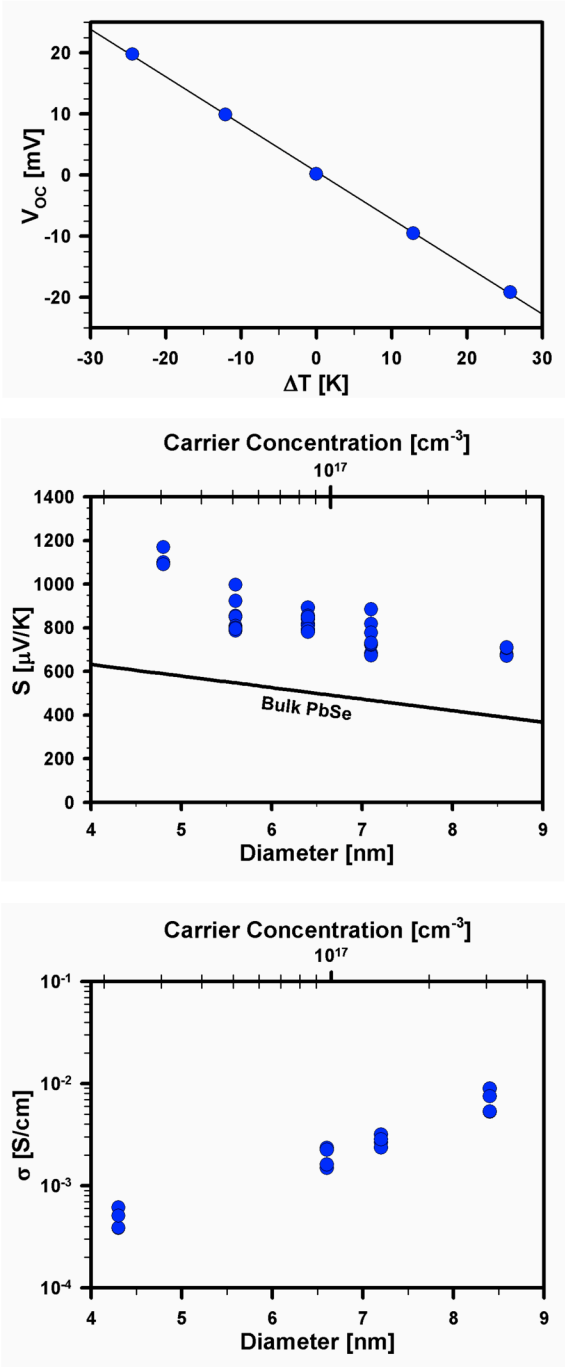

Figure 21 (a) Open circuit voltage, V_{oc}, generated in a 6.4 nm PbSe nanocrystal solid by a temperature gradient, ΔT, due to the Seebeck effect. (b) The nanocrystal size-dependence for thermopower. (c) The nanocrystal size-dependence for electrical conductivity. In both (b) and (c), the approximate carrier concentration in indicated on the top axis (log scale). The conductivity and carrier concentration indicated are representative of the entire film volume. Due to uncertainties in mobility, there is an uncertainty factor of ~2 for the carrier concentration.

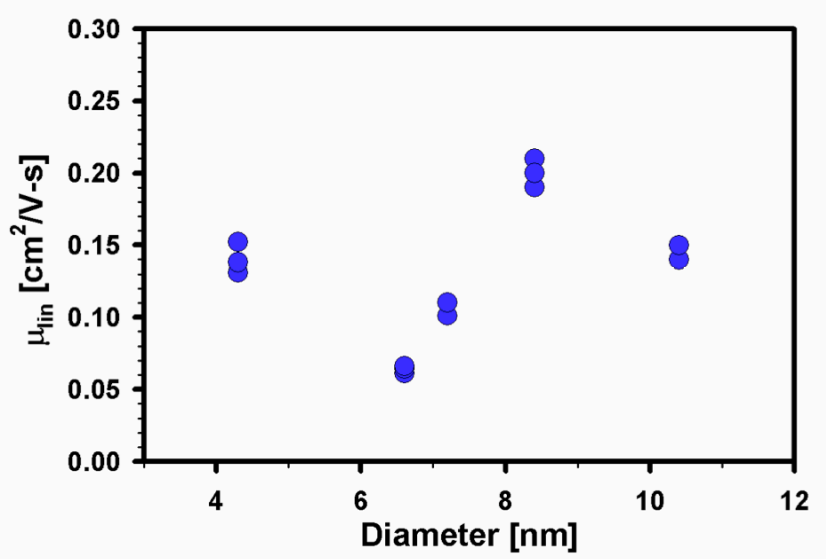

Figure 22 Electric mobility obtained by transistor measurements for PbSe films of various nanocrystal diameter.

The thermopower is approximately proportional to the difference between the Fermi Energy (E_f) and average mobile carrier energy (E_{ave}). In a bulk material with parabolic bands, the Fermi-Dirac occupation function gives a wide distribution of carrier energies (schematically shown in Figure 3a). The DOS of zero-dimensional quantum dots differs dramatically from DOS of a bulk semiconductor (Figure 23b, c) [64, 67, 77]. It has been predicted the thermoelectric power factor ($S^2\sigma$) can be greatly enhanced when the chemical potential is within a few kT's of the delta-like function of the ground state and/or one of the excited states [68]. Although we observe an enhanced thermopower, we do not observe an enhanced power factor due to low carrier mobility. Aside from enhanced thermopower, nanomaterials should also benefit from a relaxation in the Wiedemann-Franz law because it loses validity in materials with a delta-like DOS. Relative to bulk materials, nanostructured materials can have an increased ratio of electrical conductivity to electronic thermal conductivity (k_e) yielding overall greater values of ZT [69].

One possible explanation for the observed size-dependence of thermopower and electrical conductivity originates in the size-dependent band gap of the nanocrystals. The peaks in the nanocrystal absorption spectra (Figure 20a) exhibit progressive blue-shift for decreasing nanocrystal size [66]. This is a signature of the energy band gap, E_g, increasing as the nanocrystal size decreases. Over the nanocrystal size-range studied here, the absorption peak changes by ~ 230 meV. Figure 23b,c illustrates the situation where $\Delta E_f \ll \Delta E_g$ for changes in nanocrystal size (where ΔE_f and ΔE_g are the changes in Fermi Energy and energy band gap, respectively). As the nanocrystal size decreases, the band edge moves away from the Fermi Energy, which results in an increased difference between E_f and E_{ave} (Figure b,c). Since thermopower is approximately proportional to $E_f - E_{ave}$, thermopower increases as the nanocrystal size decreases. This process also results in changes of carrier concentration; larger carrier concentrations are obtained when E_f is near the band edge. As the nanocrystal size increases, the band edge moves closer to E_f. This causes the carrier concentration (and therefore the electrical conductivity) to increase. This explanation is further supported by the fact that mobility did not change with nanocrystal size, which implies that the observed changes in conductivity (Figure 21c) are due to variations in carrier concentration. Another plausible explanation for thermopower size-dependence is alteration of the scattering mechanisms that occur in nanostructured materials which can lead to carrier energy filtering [52].

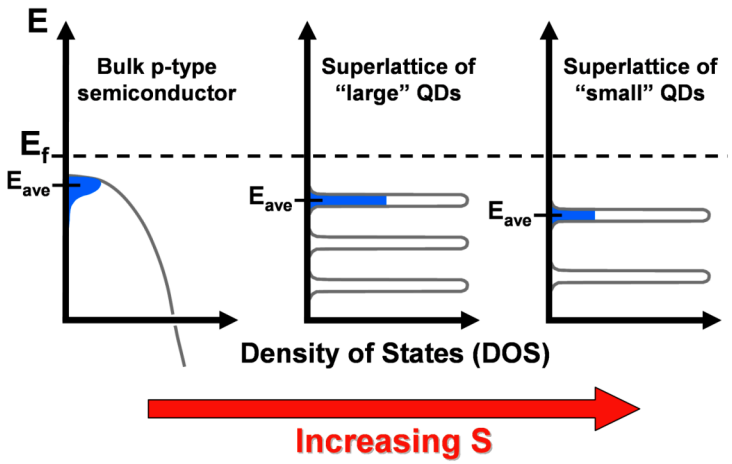

Figure 23 A mechanism that can qualitatively explain the size-dependence of thermopower in the nanocrystal solids. The electronic density of states is represented by the gray lines. The carrier concentration is represented by the area of the blue region and the thermopower is approximately proportional to $E_f - E_{ave}$, where E_f and E_{ave} are the Fermi energy and average energy of conducting holes, respectively.

In the case of PbSe quantum wells, the thermopower and electrical conductivity were found to oscillate with well thickness [79]. In contrast, we observe monotonic changes in thermopower and electrical conductivity. These are the first reported thermopower measurements of solution-processed low-dimensional materials in the regime of strong quantum confinement. The observed size-dependence creates opportunities to tune thermopower in these materials.

Studying Electronic Transport Mechanisms Using Thermopower

Besides obvious interest to thermoelectric applications of nanocrystal solids, thermopower measurements are proven to be a very powerful technique in fundamental studies of electronic structure and doping of bulk materials. In particular, it can unambiguously point to the type of carriers responsible for charge transport and provide valuable information on the Fermi energy under particular experimental conditions. Since thermopower is measured under open circuit conditions, it is not affected by contact resistance. In contrast, the data obtained by current measurements in the field-effect transistor configuration are strongly affected by nature of the contacts formed between the channel and electrodes. For example, single-wall carbon nanotubes contacted by Au or Pd electrodes show p-type gate effect [80], whereas the nanotubes contacted by a metal with low work function (e.g., Sc) show n-type gate effect due to more efficient electron injection [81]. PbSe nanocrystal solids show p-type gate effect (Figure 24b) which is also expected from comparison of the work function and ionization potential of Au and bulk PbSe (Figure 24d). On the other hand, a positive thermopower shows that the Fermi level in a PbSe nanocrystal solid is close to the $1S_h$ quantum confined state and that the nanocrystal array is p-doped. Detailed understanding of electronic doping and conduction mechanism in nanocrystal solids requires further study; a plausible hypothesis could be the presence of surface states behaving as shallow hole acceptors. These states are probably associated with undercoordinated or oxidized surface Se atoms which are known to create the acceptor states in bulk PbSe [82]. Thermal energy is required to generate a hole in the nanocrystal from the acceptor state providing mobile carrier in the $1S_h$ state. An alternative explanation could be the direct hopping between localized midgap surface states. From general considerations, observed hole mobilities (~0.1 cm^2/Vs) are somewhat too high for the hopping between trap states with localized wavefunctions that are separated by dielectric medium. To gain a better understanding of the conduction in hydrazine-treated PbSe nanocrystal solids, our collaborators at the University of Chicago have performed temperature dependent transistor measurements for low-bias conduction (V_{DS}<200mV) in N_2H_4-treated 7.2 nm PbSe nanocrystal solids. In the 200-310K temperature range, the film conduction is well described by activated transport with the activation energy E_A. Activation energy is found to strongly depend on applied gate voltage (V_G) , varying from 200 meV (V_G=40V) down to 85 meV (V_G=0V) and 28 meV (V_G=-40V). Following the analysis by Mentzel [82], we estimates the depth of the acceptor states as ~50-70 meV at room temperature. The DOS at the Fermi energy can be estimated as

$DOS(E_F) = \frac{C_i}{es}(\Delta E_F / \Delta V_G)^{-1}$ where C_i is the capacitance of the gate dielectric per unit area, s is the screening length in the nanocrystal solid and e is the electron charge. For 100 nm thick SiO_2 gate dielectric C_i~$3.4 \cdot 10^{-8}$ F cm^{-2}. $\Delta E_F / \Delta V_G$ ~ $3.1 \cdot 10^{-3}$ eV V^{-1} was obtained from the dependence of the activation energy on V_G. The possibility to efficiently operate 35 nm thick transistor channel in the depletion mode [22] shows that the screening length s is as at least 20 nm. These parameters yield DOS(E_F) < $3 \cdot 10^{19}$/eV cm^{-3} at V_G=0V, i.e., less than 0.5 electronically active acceptor states per nanocrystal and more than an order of magnitude lower than DOS associated with S-type quantum confined orbitals. The localization length a for midgap states is small (~1 nm) compared to that for S states (~ nanocrystal radius, ~3.6 nm). The probability of hopping between two states with similar energy is proportional to P~exp(-2d/a) where d is the hopping distance [83]. For d~8 nm, which is a reasonable estimate for our nanocrystal solid, the probability of hopping between localized midgap states should be ~5 orders of magnitude lower than the hopping probability for more delocalized S states. These arguments seem to strongly support the transport through quantum confined orbitals, not through the surface states. Thermal energy is required to generate a hole in the nanocrystal from the acceptor state providing mobile carrier in the $1S_h$ state. For a 60 meV deep trap the ionization probability at room temperature is about 10%.

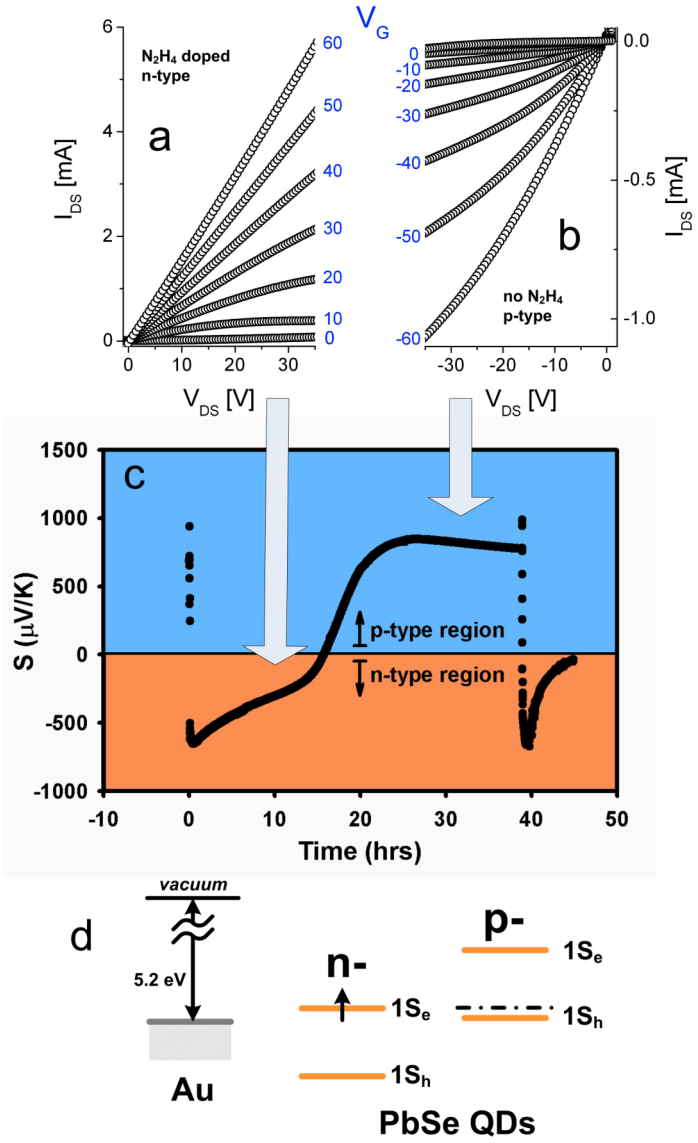

Figure 24 Transistor measurements on 8.5 nm PbSe nanocrystal solids: plots of the current between drain and source electrodes (I_{DS}) versus drain-source voltage (V_{DS}), as a function of gate voltage (V_G). Device channel length is 10 μm, width 3000 μm and thickness of SiO_2 gate dielectric is 100 nm. In the presence of hydrazine the nanocrystal solid exhibits n-type gate effect (a) whereas removal of hydrazine in vacuum switches the device to p-type gate effect (b). (c) Monitoring of thermopower of a PbSe nanocrystal solid during hydrazine addition/removal (nanocrystal diameter ~ 9.2 nm, film thickness ~ 500 nm). At t = 0 hrs, the sample had a steady-state thermopower of 685 μV/K. A few drops of 1 M hydrazine in acetonitrile were added at t = 0 hrs and t = 39 hours. With the addition of hydrazine, the PbSe nanocrystal solid switches from p-type (S > 0) to n-type (S < 0). See text for more detail. (d) Energy diagram proposed for PbSe nanocrystal solid in contact with Au electrodes on the basis of combined transport and thermopower measurements.

To control p-type doping level, we exposed a film of 6.4 nm PbSe nanocrystals to oxygen, which is a well-known p-dopant of bulk lead chalcogenides [84]. After the exposure, we observed an increase in the conductivity of PbSe nanocrystal film by about one order of magnitude (Figure 25) accompanied with a decrease in thermopower from 760 μ V/K to 440 μ V/K (Figure 26). After exposure to oxygen, the nanocrystal solid showed weak gating and electrical measurements alone could not separate the conductivity increase due to changes of carrier mobility and/or doping level. The decrease in thermopower points to a shifting of the Fermi Energy closer to the $1S_h$ state due to the doping effect.

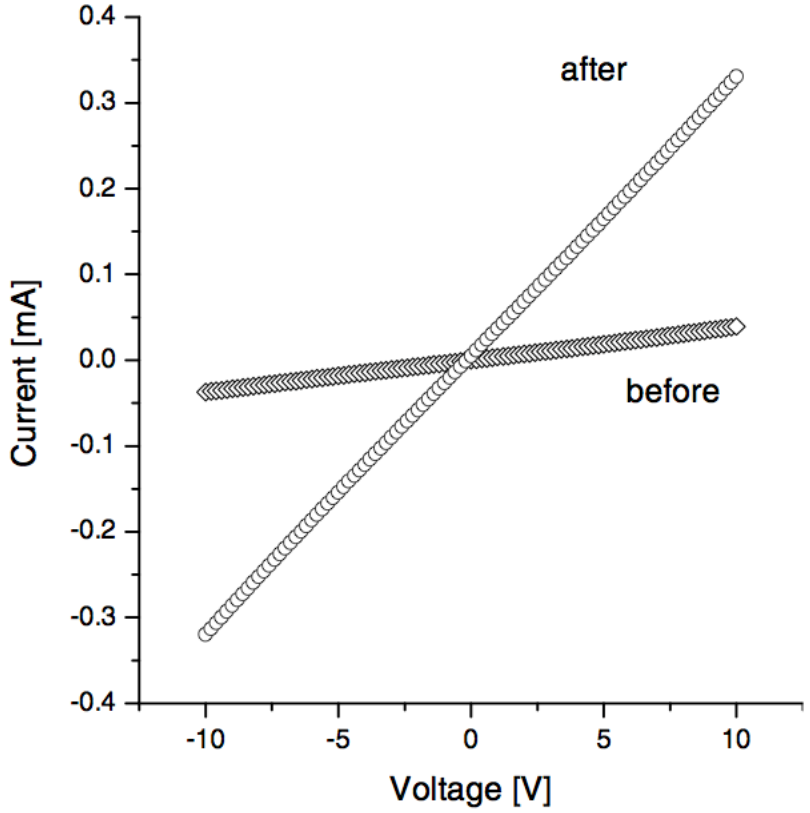

Figure 25 I-V Curve for PbSe quantum dot superlattice in N_2 (diamonds), and after exposure to air (circles).

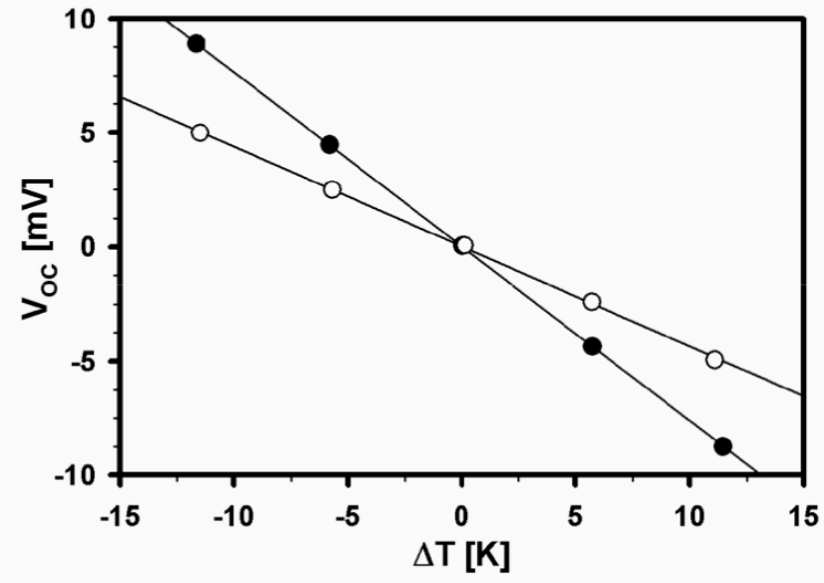

Figure 26 Thermopower measurement of 6.4nm PbSe nanocrystals in N_2 (open circles) and in air (closed circles).

We also used thermopower measurements to study characteristics of n-type surface charge transfer doping of PbSe nanocrystals with hydrazine. Thermopower was continuously monitored as the relative amount of hydrazine in a nanocrystal thin film was varied. This experiment is depicted in Figure 24c. At t = 0 hrs, the sample had a steady-state thermopower of ~ 685 μ V/K, and a few drops of 1 M hydrazine in acetonitrile are placed on the film. The droplets evaporate after a few minutes and a sharp transition from p-type (S > 0) to n-type (S < 0) is simultaneously observed. A slow transition back to p-type is observed over the course of many hours. We attribute this slow transition to evaporation of hydrazine from the nanocrystal film. These results conclusively show that n-doping of PbSe nanocrystal solids is determined by hydrazine adhered to the nanocrystal surface. The n-type doping occurs through the formation of charge-transfer complex between the nanocrystal and hydrazine molecules. Reversible behavior is demonstrated when we repeat the hydrazine treatment at t = 39 hrs. The transistor measurements on similarly treated PbSe nanocrystal films show n-type gate effect in the presence of hydrazine, slowly switching to ambipolar and, finally, p-type gate effect after removal of hydrazine (Figure 24a). Since thermopower measurements are open-circuit, they remove the possibility of the effects associated with non-ideal contact behavior. Figure 24c also shows that hydrazine-doped PbSe nanocrystal solids can reach large negative thermopowers (~ - 650 μ V/K), considerably exceeding values reported for n-PbSe [84].

This work demonstrates that PbSe nanocrystal solids exhibit a significant thermopower enhancement of several hundred μV/K relative to bulk PbSe. This can be attributed to the sharp peaks in the electronic DOS of nanocrystal solids. Tunability of thermopower via changes in nanocrystal size has also been demonstrated. If the electrical conductivity can be improved, these materials represent an emerging class of inexpensive and scalable thermoelectric materials. This can be done by either increasing the carrier concentration or improving mobility. Increasing carrier concentration generally results in a decrease in thermopower, but could enhance ZT up until a maximum S^2n is reached. This maximum value has not been achieved in this work and remains unknown. A more promising route to improve ZT is to improve mobility (e.g. reduce carrier scattering). To compete with commercial thermoelectric materials the carrier mobility in nanocrystal solids should be increased by at least 2-3 orders of magnitude.

Thermal Transport in Fully Inorganic Colloidal Nanocrystal Composites

It is well known that nanostructured materials have enhanced figure-of-merit due to reduced lattice thermal conductivity compared to their bulk components. However, the highest performance nanostructured thermoelectrics have not yet penetrated into widespread commercial production primarily because the processes used to make them require slow and complicated growth techniques such as molecular beam epitaxy, metal organic chemical vapor depostion, or highly controlled ingot growth with precipitates. It would be highly beneficial if similar materials could be made by scalable techniques such as solution processing.

Poudel has shown that nanostructured $Sb_{2-x}Bi_xTe_3$ with high figure-of-merit can be made by using an ultra-high energy ball milling process to produce very finely grained particles, which can then be reassembled into a fully dense material with nanosized crystalline domains using spark-plasma sintering (SPS) [2]. While this method is highly scalable and applicable to many other material systems, the nanostructures made by this method cannot be precisely controlled: grain sizes are not monodisperse and achieving grain sizes below 10nm is difficult. Semiconducting colloidal nanocrystal technology provides an excellent alternative to high energy ball milling for the tunable and scalable production of nano-sized objects. Colloidal nanocrystals can be produced for a variety of materials at low temperature in solution and have excellent characteristics in terms of minimum feature size, tunability, and monodispersity. Thus, in addition to being a possible vehicle for thermoelectric production, they are an ideal platform to study the fundamental physics of transport in nanograined materials.

In order to slow growth rates to experimentally accessable time-scales (e.g. minutes), colloidal nanocrystals are typically grown in high boiling point solvents in the presence of lengthy organometallic surfactants/ligands. These surfactants also serve other important roles, such as to control particle solubility, to prevent undesirable particle fusion after the growth process, and to passivate the dangling bonds on the surface of the crystals, which may constitutes up to 10% of all the atoms in a very small crystal. However, surface ligands are typically insulating and severely impede electrical transport between nanocrystals. Removal of the ligands can be achieved by exposing films to a reducing agent such as hydrazine or ethanol [26], which has been shown to increase electrical mobility by ~7 orders of magnitude in PbSe films. However, films treated by this method must undergo substantial geometric rearrangement due to the change in volume, which leads to the formation of cracks, which must then be back-filled. A alternative method developed by Kovalenko et al. [39] involves the post-synthetic (but pre-film-formation) exchange of the organic ligands for hydrazine-based metal chalcogenide clusters (MCC) which become charge stabilized ligands. A suspension of colloidal nanoparticles (in an organic solvent) is placed in contact with a solution of MCC's (in hydrazine or another polar solvent). If the MCC binds more tightly

to the surface of the particle than the organic ligand, then the MCC replaces the surface groups and the particle becomes soluble in the polar solvent and transfers phase; the organic ligands typically remain in the organic solvent or are drawn to the interface between the two solvents which allows the extraction of a purely inorganic, polar solution of nanoparticles funtionalized with MCC's. Conveniently, most MCC's can be decomposed under mild heating to form useful electronic materials (i.e. $Sn_2S_6(N_2H_5)_4$ decomposes into the semiconductor SnS_2). Thus, this technique is a very flexible platform for the creation of rationally designed nanostructures held together by functional "glue" or matrix materials.

Heat Tranport in Ultra-fine Grained CdSe Nanocomposites

Nanocomposites were made by this technique to study heat transport in ultra-fine grained nanostructures of CdSe. HgSe was chosen as a MCC ligand for CdSe because Hg is isovalent with Cd and because $Hg_{1-x}Cd_xSe$ alloys have shown promise for thermoelectric application previously [85]. However, it should be noted that the final nanocomposites will have a Hg:Cd ratio of less than 0.01. Monodisperse particles of CdSe were grown in the range of 3-6nm by the Dimethylcadmium technique using a robot at The Molecular Foundry [86]. X-ray diffraction shows peaks indicative of the zincblende crystal structure. CdSe nanocrystals have larger band gap due to quantum confinement and show blue-shifted absorption band edge which is used to determine the particle size as 3.1 – 6.1nm for various batches [87]. After synthesis, excess ligand was removed by precipitating in a Hexane:Acetone:Methanol solution (~2:1:2) and resuspended in Hexane. A precursor for HgSe (HgSe MCC) was prepared by stirring 1mmol HgSe (99.999%, Alfa Aesar), 1mmol Se shot (99.999%, Aldrich) in 4mL freshly distilled hydrazine. For each ligand exchage, a solution was prepared by stirring 100μL HgSe MCC solution in 1mL of distilled hydrazine. Nanoparticle suspensions (2mL of ~0.05M CdSe in Hexane) were added to the MCC solution, forming a separate phase on top of the MCC's, and stirred. Nanocrystals transfered phase after several minutes. After 30 minutes, the hydrazine phase was removed by pipette and filtered. At this point, the particles are soluble in hydrazine and there is a large excess of HgSe MCC. In order to control the amount of HgSe in the final composites, excess MCC was removed by precipitating the particles in a 2:1 mixture of acetonitrile and hydrazine. This step is necessary to control the final composition of the composite since the concentration of the CdSe particle is not known precisely prior to the ligand exchange. However, once the particles are re-suspended in hydrazine, they contain only the amount of HgSe MCC required for solubility. The absorption spectra for the CdSe in hydrazine (Figure 27) is similar to the spectra before ligand exchange, confirming that no change in size occurs, in agreement with the observations of Kovalenko [39].

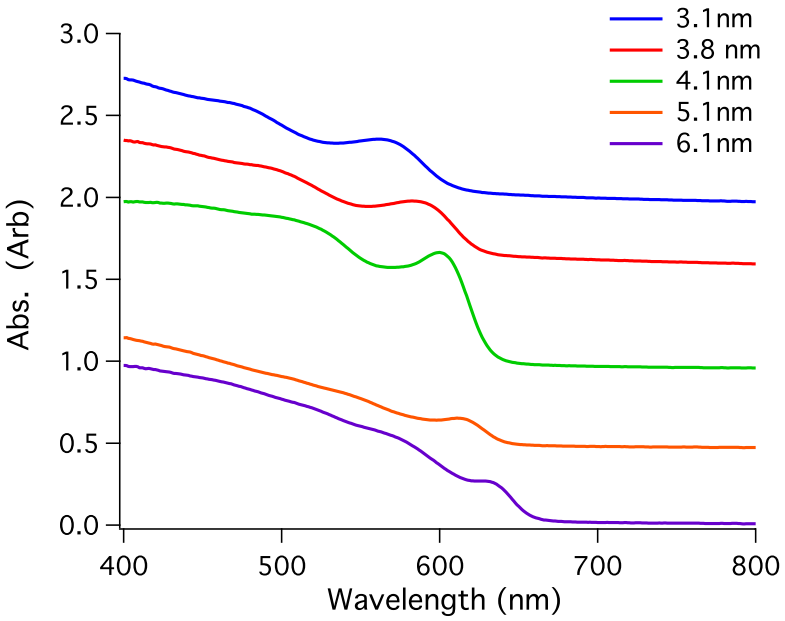

Figure 27 Absorption spectra of nanocrystals after ligand exchange in hydrazine. Quantum confinement leads to blue-shift in the absorption edge, which has been used to determine the size of the nanocrystals from [85].

After re-suspending the particles in 2mL of hydrazine, each particle solution was drop cast onto sapphire substrates for thermal characterization. To achieve high quality drop cast films, sapphire substrates were cleaned using the "piranha" process (3:1 H_2SO_4:H_2O_4) followed by a UV ozone treated for several minutes. A leveled, isothermal platform covered by a culture dish was used to slow the evaporation rate to <0.1 μL/hr-cm^2 which yielded very smooth films with RMS roughness of a few nm for ~500nm thick films (Figure 28). Powder X-Ray Diffraction (XRD) and Thermogravimetric Analysis (TGA) indicate that the HgSe MCC is completely decomposed and crystallized by 150-175C (Figure 29). Thus, CdSe nanocomposite films were annealed at 165C for 30 minutes. X-ray diffraction profiles of the nanocomposites show that the peakwidth is large, consistent with a distribution of nano-sized domains and is unaffected by the annealing time for at least 1hr (Figure 30).

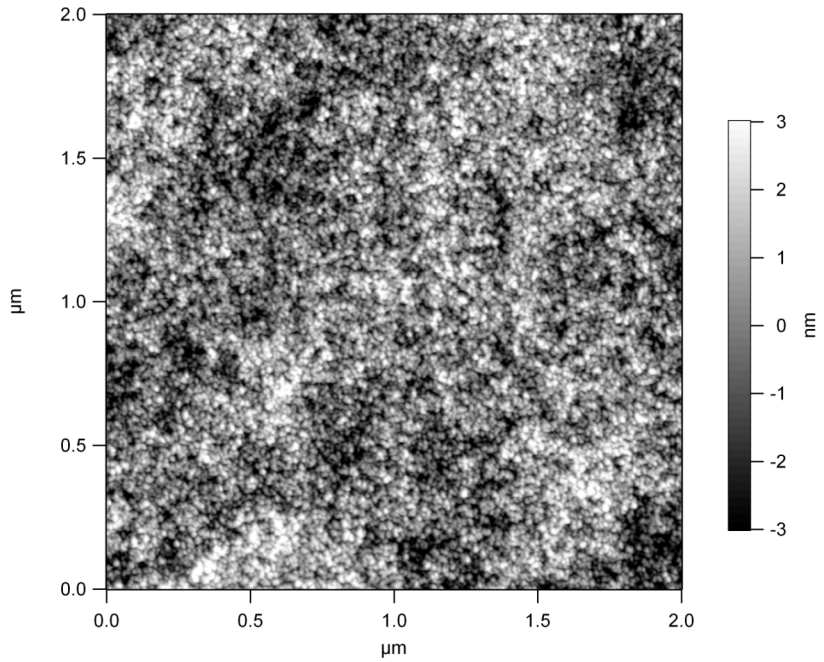

Figure 28 AFM image of a nanocomposite made from 4.1nm CdSe crystals

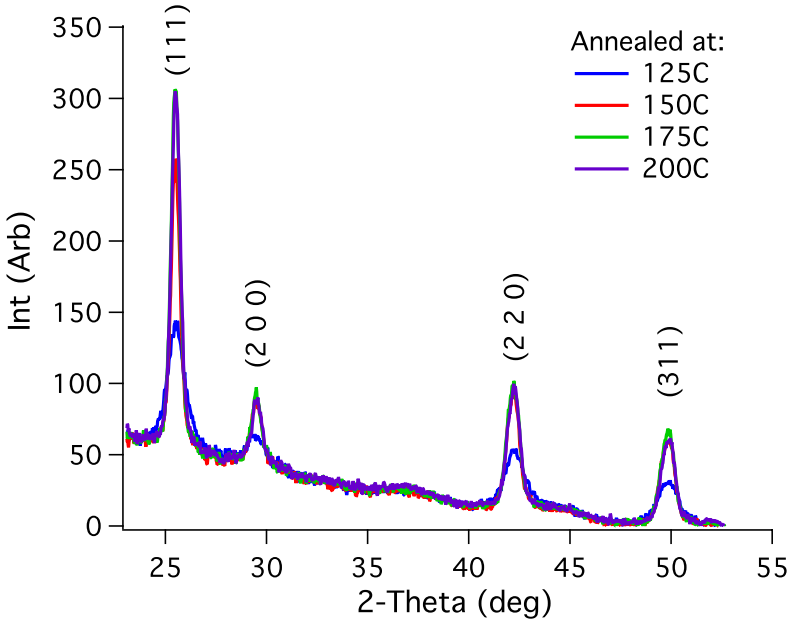

Figure 29. Powder X-Ray diffraction pattern from annealed films of HgSe MCC as a function of annealing temperature. Between 150-175°C sharp peaks are recovered corresponding to the zincblende phase of HgSe.

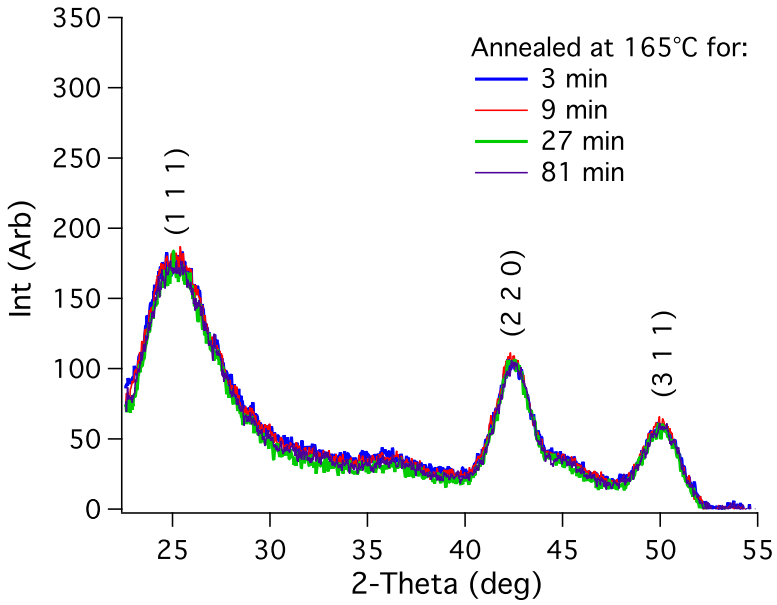

Figure 30. Powder X-Ray diffraction pattern from annealed films of 6.1nm CdSe annealed at 165°C. The peakwidths show that domain sizes are stable for at least 1hr.

Figure 31 shows the powder diffraction pattern for the nanocomposites after the thermal annealing for various starting nanocrystal sizes. Debye-Scherrer analysis can be employed to estimate the grain size [88]. In that case, the average grainsize, L, is

$$L = \frac{k\lambda}{\Delta\theta\cos(\theta)} \qquad 4.1$$

where λ is the radiation wavelength (CuKα=0.15406 nm), k is a Debye-Waller geometric factor between 0.8-1.4, and $\Delta\theta$ is the peakwidth (FWHM). Based on the (111) peak location, the estimated grainsize is ~2.0-3.9nm for the films (depending on the assumed assumed value of k). In addition, we observe that the peaks are shifted to slightly higher diffraction angle than would be expected from a bulk crystal and the magnitude of the shift depends monotonically on the starting crystal size. Thus, the nanocrystals have lattice constant smaller than bulk, indicating the presence of a size dependent strain. While this has been previously observed in nanocrystals covered with organic ligands [89], this is the first observation of this phenomena in dense inorganic nanocomposites. The origin of this lattice contraction is debatable. Normally, this effect is due to the high surface energy of the nanocrystal which causes structural rearrangement. However, for a dense composite, these forces should be significantly smaller. Several possible alternate explanations exist and will be discussed after the thermal characterization.

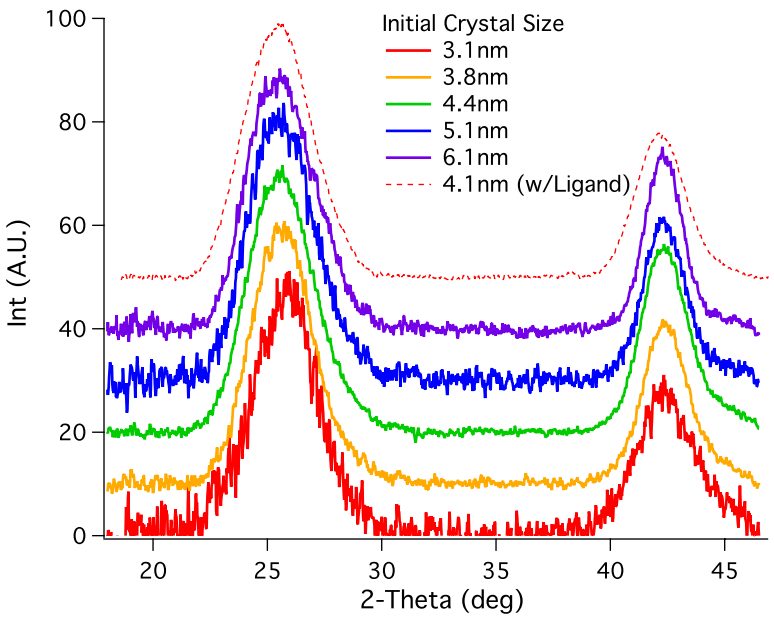

Figure 31 Powder X-Ray Diffraction of the final nanocomposite films used for thermal characterization. A film showing the pattern of the pre-ligand exchange particles is shown for comparison. Films show a size-dependent shift in the (111) peak location.

As shown via SEM (Figure 32) and HRTEM (Figure 33), films are smooth and consist of well packed small grains, reflective of the starting nanoparticle size. Films were prepared for high resolution transmission electron microscopy (HRTEM) using the same procedures as those used for thermal measurements with the exception that drop cast were made onto 200nm thick Silicon nitride suspended membranes with 10μm holes (cleaned using UV-Ozone). Images were taken in thin regions spanning the holes, which yielded the images shown in Figure 33. HRTEM shows clear crystalline domains approximately the same size as the starting nanocrystal.

Figure 32 SEM Image of a CdSe nanocomposite film (6.1nm nanocrystal size). The image was taken near a crack to show that the image is in focus.

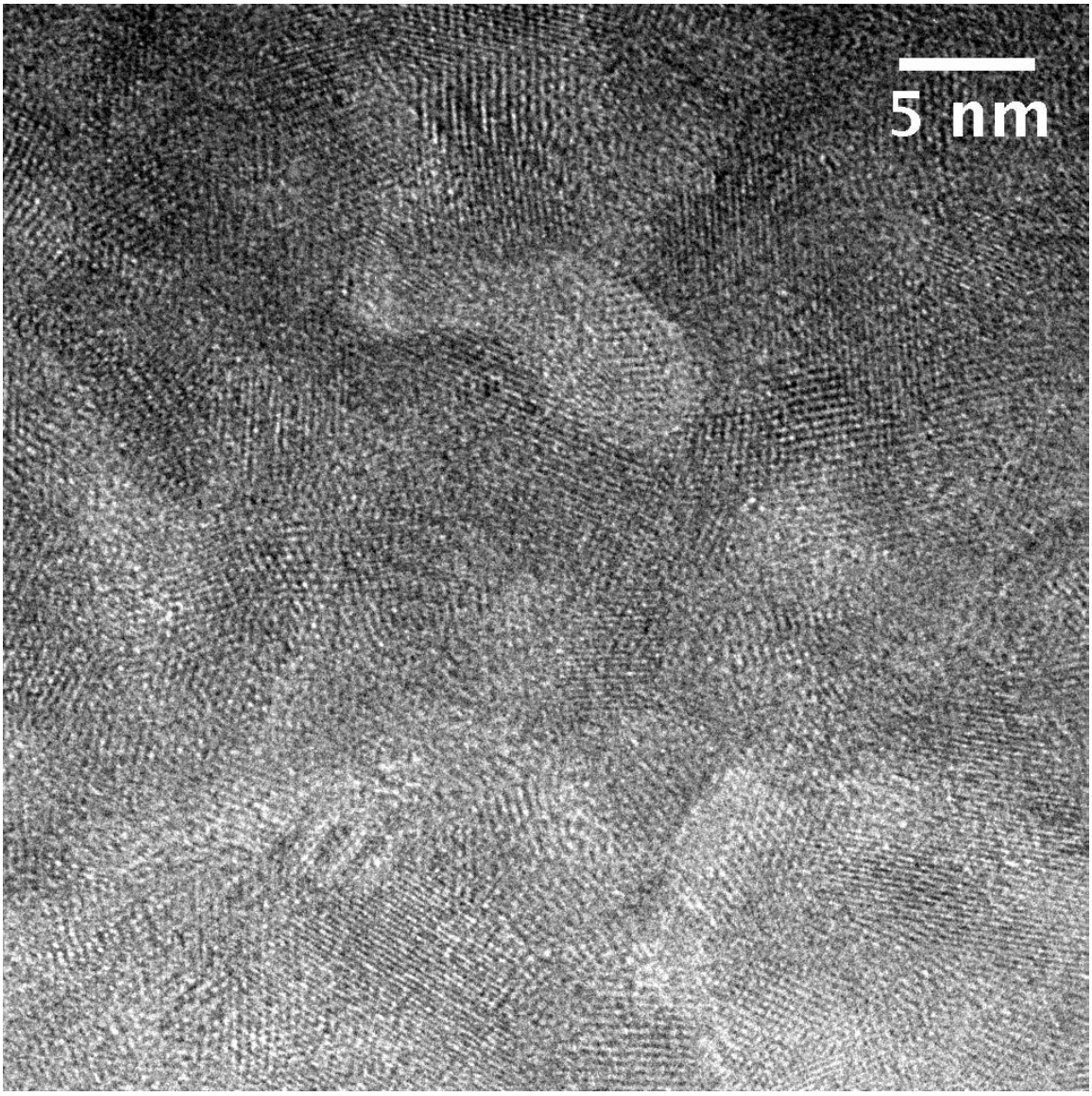

Figure 33 HRTEM image of a CdSe nanocomposite made from a starting particle size of 3.8nm.

Rutherford Backscattering (RBS) and Electron Dispersive X-ray Spectroscopy (EDS) both indicate the presence of very little Hg in the final films. As estimated from RBS, which is more sensitive for Hg, the final Hg:Cd ratio is about 0.001, which is near the limits of detectability for that method. This corresponds to submonolayer coverage of the initial nanocrystal in solution.

Nanocomposites between 100nm-500nm thick were thermally characterized using the 3ω method. To electrically isolate the CdSe composites from the heaterline, a

film of ~80nm thick Parylene dielectric material was deposited via a low temperature chemical vapor deposition technique. A resistive thermometer with dimensions 200μm x 5μm was then formed by liftoff lithography and 50nm Au was deposited by slow, thermal evaporation (~0.1 A/sec). Thermal transfer functions were measured from 50Hz-10,000Hz and analyzed using the differential method. The film thickness was determined after the experiment by creating a scratch directly adjacent to the heaterline and measuring the step-height using a profilometer to within an uncertainty of ~20nm and averaging over several locations along the line. Twelve total films were characterized at room temperature for nanocrystal sizes 3.1nm (2 films), 3.8nm (4), 4.1nm (1), 5.1nm (2), and 6.1nm (3). Temperature dependence was measured for one film from 200K-300K. The results are shown in Figure 34 and 35.

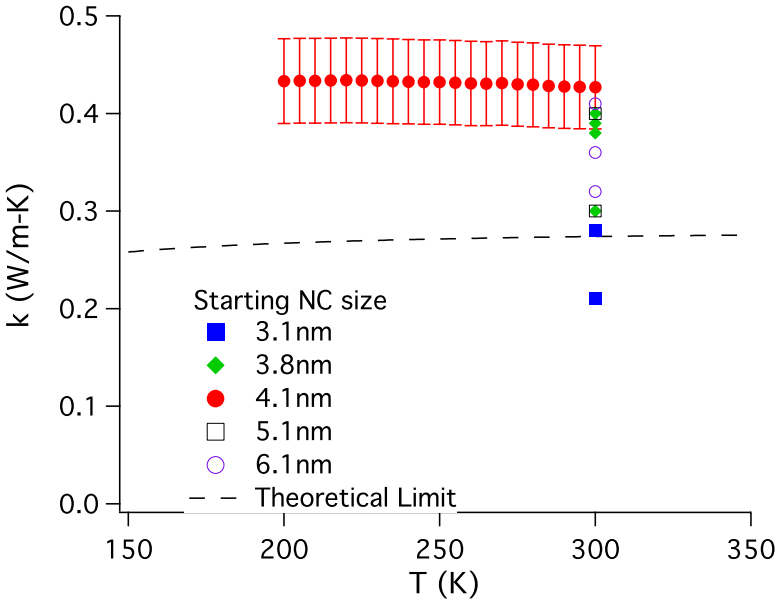

Figure 34 Summary of measured thermal conductivities. The theoretical limit is calculated from the bulk properties of single crystal CdSe using equation 4.2.

Results and Modeling

The thermal conductivity measured for all films is very low. All twelve measurements had conductivities below 0.43 W/m-K at room temperature, more than a factor of 20 below the bulk thermal conductivity of CdSe [90]. The temperature dependence of the thermal conductivity is very flat, which is consistent with a scattering rate that has little frequency dependence, such as boundary scattering. The measured thermal conductivity does not appear to be a strongly dependent on the starting nanoparticle size. However, owing to the difficulty of measuring the thickness, some of the thinnest films have an uncertainty of ~20%, which may mask any potential size dependence. Never-the-less, the films are very close to the theoretical lower limit for

the thermal conductivity of a disordered crystal, which can be numerically calculated using the number density of atoms, η, and the speed's of sound, v_i, using the equation [49],

$$k_{\min} = \left(\frac{\pi}{6}\right)^{1/3} k_B \eta^{2/3} \sum_i v_i \left(\frac{T}{\theta_i}\right)^2 \int_0^{\theta_i/T} \frac{x^3 e^x}{(e^x - 1)^2} dx \qquad 4.2$$

$$\theta_i \equiv v_i (\hbar / k_B)(6\pi^2 \eta)^{1/3}$$

Physically, this equation represents the uncorrelated motion of atoms that are weakly coupled such that adjacent atoms may exchange energy. Cahill et al [49] have shown that this model approximately describes thermal transport in amorphous solids and represents a lower limit to the thermal conductivity of highly disordered crystals. Using the properties of bulk CdSe, the theoretical minimum thermal conductivity is shown in Figure 31. The only measured film which is below this was very thin (~100nm) and thus the measurement uncertainty was ~20% (high enough that the violation is inconclusive).

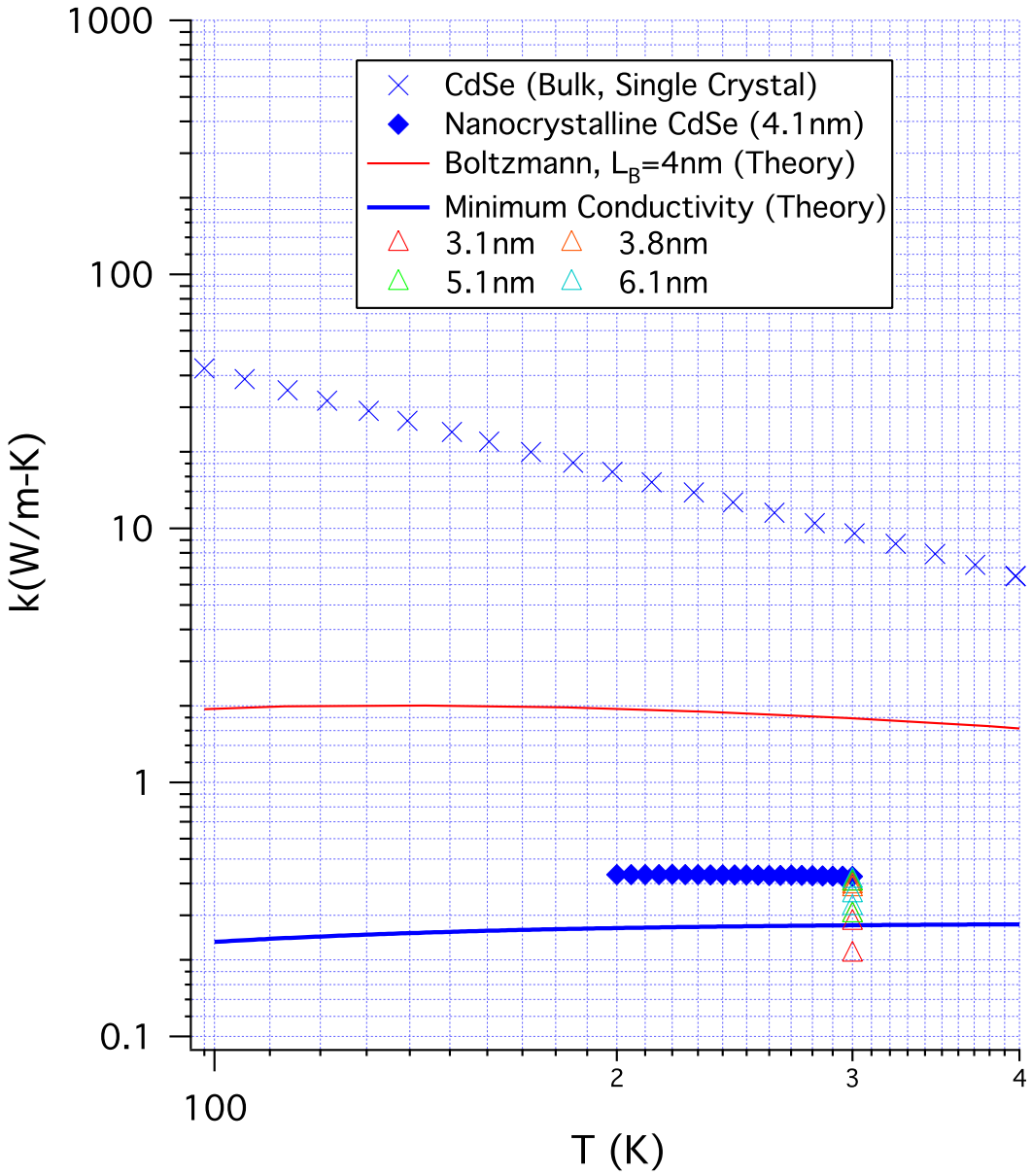

Figure 35 Summary of experimental and theoretical modeling results. CdSe nanocomposites are ~20-30 times less conductive than a single crystal, and show conductivity ~4-5 times below theoretical estimates based on boundary scattering.

While this represents a lower limit to the expected value, it is more illuminating to predict the expected behavior using the Callaway model. Phonon scattering in these

finely grained was modeled using the combination of phonon-phonon scattering and boundary scattering with scattering rates of the type

$$\tau_N^{-1} = B_1 T^3 \omega^2 \qquad 4.3$$

$$\tau_U^{-1} = B_2 T^2 \exp(-\theta_D / nT)\omega^2 \qquad 4.4$$

for the Normal and Umklapp phonon-phonon processes, and

$$\tau_B^{-1} = v / \ell_B \qquad 4.5$$

as a boundary scattering term. Minnich et al. has recently shown that this type of model adequately describes transport in ball-milled/sintered SiGe composites, albeit with a significantly larger grain size (10-20nm) and Debye temperature [91]. To estimate phenomenological constants (B_1, B_2, n) in the phonon-phonon scattering time, the temperature dependence of the thermal conductivity for bulk, single crystal CdSe was fit to the Callaway model neglecting all scattering effects other than phonon-phonon interactions. Since no literature data exists regarding the temperature dependent thermal conductivity of single crystal CdSe, an (1000) oriented crystal was obtained commercial and measured from 100K-400K using the 3ω method (Figure 35). At 300K, our results are in good agreement with the conductivity reported by Ioffe [90].

Modeling results (Figure 36) then show that boundary scattering should substantially alter the room temperature thermal conductivity once the grain size is below about 30nm. However, using boundary scattering alone, the measured value of the thermal conductivity cannot be explained. In fact, the measured values are about 4-5 times lower than values obtained from the modeling, which physically means that the actual phonon mean free path must be smaller than the crystallite size.

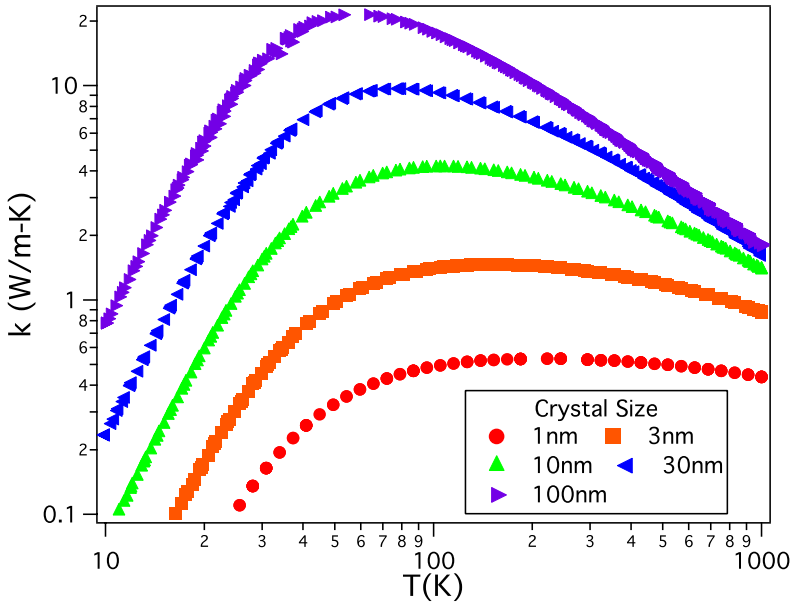

Figure 36 Thermal conductivity of CdSe predicted from Debye-Callaway modeling, including only the effects of phonon-phonon scattering and boundary scattering.

We have considered possible alternative explanations for the increase in scattering. One obvious alternate explanation would be the existence of large voids/porosity; however, we do not believe this to be the case, since in order to explain the current data, a very high degree of porosity and/or tortuosity would have to be present which has not been seen throughout the imaging or other characterization techniques. Rather, it seems likely that a deficiency in the model exists.

Apart from phonon-phonon scattering, it is possible that some type of impurity scattering is occurring within the particle. Such impurities could come from a combination of Hg alloying from the initial HgSe MCC, vacancies, isotopic impurities, or other non-point defects such as stacking faults. Since Cd and Se both contain a wide array of isotopic impurities, the model of Abeles [58] has be been adopted to calculate the scattering rate.

$$\tau_{isotope}^{-1} = A\omega^4$$

$$A = \frac{\delta^3}{4\pi v^3}\sum_i x_i\left(\frac{M_i - \bar{M}}{\bar{M}}\right)^2 \qquad 4.6$$

where the summation is over the various isotopic impurities each with mass M_i compared to the average mass $\bar{M} = \sum x_i M_i$. Considering the isotopic impurties of Cd (^{106}Cd(1.3%), ^{108}Cd(0.9%), ^{110}Cd(12.5%), ^{111}Cd(12.8%), ^{112}Cd(24.6%), ^{113}Cd(12.2%), ^{114}Cd(28.7%), ^{116}Cd(7.5%)) and Se (^{74}Se(0.9%), ^{76}Se(9.4%), ^{77}Se(7.6%), ^{78}Se(23.8%), ^{80}Se(49.6%), ^{82}Se(8.7%)) the value of A can be computed to be ~5.6x10^{-43} s^3, which is not intense enough to significantly alter the physical picture. Based on the Callaway model, we estimate that a value of the constant, A, of about 5×10^{-41} s^3 would be required to match the observed data.

There is not enough Hg in the composites to create substantial alloy impurity scattering in the composites (~0.1%at Hg), however it is observed that the Se:Cd ratio in the final composites is consistently above stoichiometric by ~10% (Figure 37). Measurement of the pre-ligand exchange particles show insignificant deviations from stiochiometry, so the excess Se would appear to be a result of the MCC treatment. Although the decomposed HgSe MCC also deviates from stoichiometric (Figure 38), there is not enough HgSe to explain the amount of extra Se found in the film (0.1% vs 10%), and thus the exact origin in not yet understood.

Regardless of its origin, given the amount of excess Selenium in the final film it may be possible that other point impurities are being generated such as Cd vacancies. It is known that vacancies in some materials have the effect of reducing the lattice constant as atoms reconstruct around the defect [92, 93], which could explain slight shifts of the XRD peaks relative to the bulk peaks in Figure 31. Also, Cd vacancies are known to cause deep trap states in CdSe [94] and CdTe [95], which impedes electrical transport and disrupts photoluminescence; we have observed both effects in our annealed films. Using an alloy scattering term of the type in equation 4.6, we estimate that if 5% of the Cd sites were vacant, the Boltzmann transpsort model would fit the

measurements. However, such a high density of vacancies would be unprecedented, and we currently have no way to directly observe this. In contrast, many observations have been made of the self-cleaning mechanisms in nanostructures, which should expel excess material to the outer surface of the nanocrystal [96]; self-cleaning has not been reported for vacancies, but is commonly observed for dopants and other inhomogeneities.

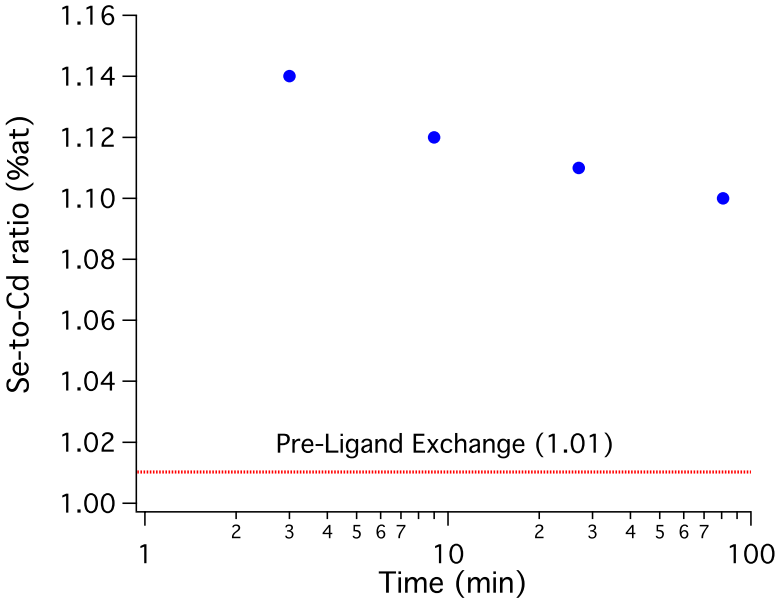

Figure 37 Stoichiometry of a CdSe nanocomposite (6.1nm) obtained from energy dispersive X-ray spectroscopy as a function of annealing time, compared with the as-made nanocrystals (pre-ligand exchange). Films show a large excess of Se which is not present in the starting material.

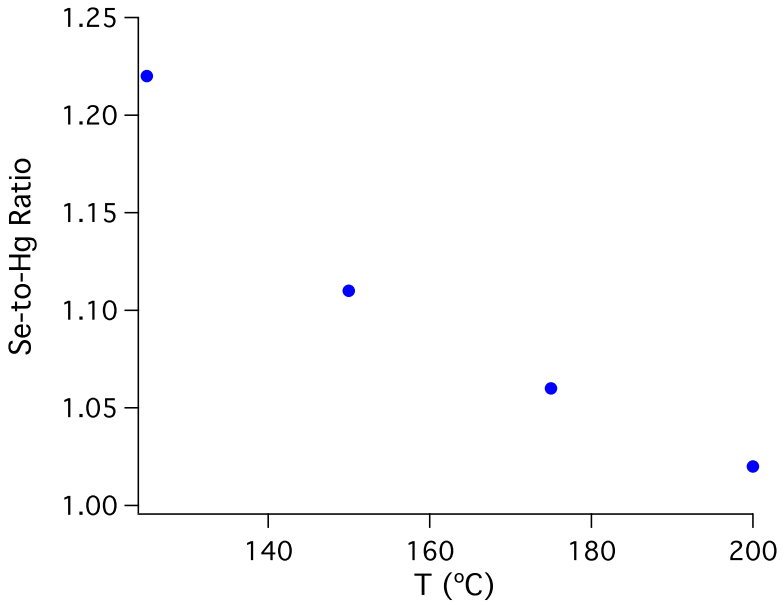

Figure 38 Stoichiometry of HgSe films obtained from energy dispersive X-ray spectroscopy as a function of annealing temperatures. Initial film contain an excess of Se, which decreases at higher annealing temperatures.

A more intriguing possibility is that the particle scattering model cannot adequately explain these materials. This material represents the smallest grained structure ever thermally characterized, and has a grain size that is nearly the same size as the dominant wavelength of the phonons involved in transport. In this material, long wavelength phonons cannot exist with distinct polarization, so the entire Boltzmann transport approach is called into question. On the other hand, a mean-field theory may not be appropriate either since the wavelength is comparable to the grain size [62]. Further understanding of the role of long wavelength vibrations will require low temperature thermal characterization that can distinguish between point defects and boundary scattering effect. The role of changes to the phonon dispersion relations/density-of-states may benefit from modern spectroscopic techniques such as inelastic neutron and x-ray scattering. If the ultra-low thermal conductivities reported here can be demonstrated in the presence of strong electrical properties, fully inorganic nanocomposites made from colloidal nanocrystals would represent a cost-competitive approach to forming nanostructured thermoelectric materials.

Universal and Solution-Processable Precursor for Bismuth Chalcogenide Thermoelectrics

Solution-processed materials are extremely attractive due to their compatibility with established high-throughput manufacturing techniques such as casting, printing, and dip-coating. These benefits have made solution-processing an attractive emerging production route to low-cost electronics [97] and photovoltaics [98]. Our method involves hydrazine-mediated reduction of a bulk semiconductor to create a solution-processable precursor, in analogy to work on chalcogenidometallate clusters for other electronic materials applications [28, 99]. These precursors are typically formed by mixing the metal-chalcogenide of interest with elemental chalcogen and hydrazine. This yields a mixture that can be solution-processed and then thermally decomposed into a polycrystal of its parent metal-chalcogenide. Using this chemistry, a number of applications have been demonstrated such as transistors [28, 29, 40, 100], phase change memory [30, 31], and photovoltaics [32, 101]. This represents the first demonstration of this approach for thermoelectric applications.

Materials Synthesis and Characterization

Recently, we have developed a route to the entire family of bismuth chalcogenide thermoelectric compounds by first creating a universal precursor based on bismuth sulfide (Bi_2S_3)[102]. The precursor was made by reacting 2 mmol Bi_2S_3 (Strem, 99.999%), 4 mmol S (Sigma Aldrich, 99.99%), and 4 mL of distilled hydrazine in a glass vial. After stirring for one or more days in a nitrogen atmosphere, the precursor forms a black viscous liquid. This results in a black viscous liquid. Thermogravimetric analysis of the dried precursor indicates that the decomposition process is complete by 250°C (Figure **39**). X-ray diffraction (XRD) of the precursor before and after decomposition (Figure 40) also illustrates a structural metamorphosis. XRD analysis indicates that the decomposition product is a polycrystalline mixture of Bi_2S_3 and elemental Bi. We demonstrate the utility of this precursor by manipulating its decomposition product into pure-phase compounds of the generalized form, $Bi_2Te_{3-x}Se_x$. For this, two chalcogenide solutions of (1) 1.5 M Se (Strem, 99.99%) solution in distilled hydrazine, and (2) 1.0 or 1.5 M Te (Alpha Aesar, 99.9999%) solution in distilled hydrazine were also prepared. Varying amounts of (1) and (2) were then added to the precursor to supply a stoichiometric amount of selenium and/or tellurium for the desired $Bi_2Te_{3-x}Se_x$ compound. During decomposition of these mixtures, the sulfur in the film is removed by the formation of gaseous byproducts. We use this approach to create the entire family of bismuth chalcogenide thermoelectric compounds: Bi_2Te_3, Bi_2Te_2Se, Bi_2TeSe_2, and Bi_2Se_3 (Figure 40). This approach is similar to a previously demonstrate route to $CuInSe_2$ and $CuInTe_2$ which are made by mixing multiple metal chalcogenide clusters [29, 100].

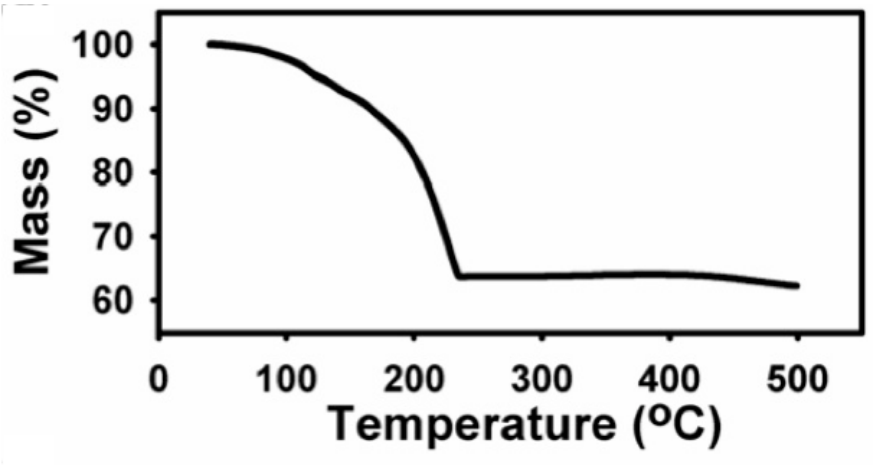

Figure 39 Thermogravimetric analysis of the dried Bi_2S_3 precursor. The sample was heated at a rate of 2°C/min.

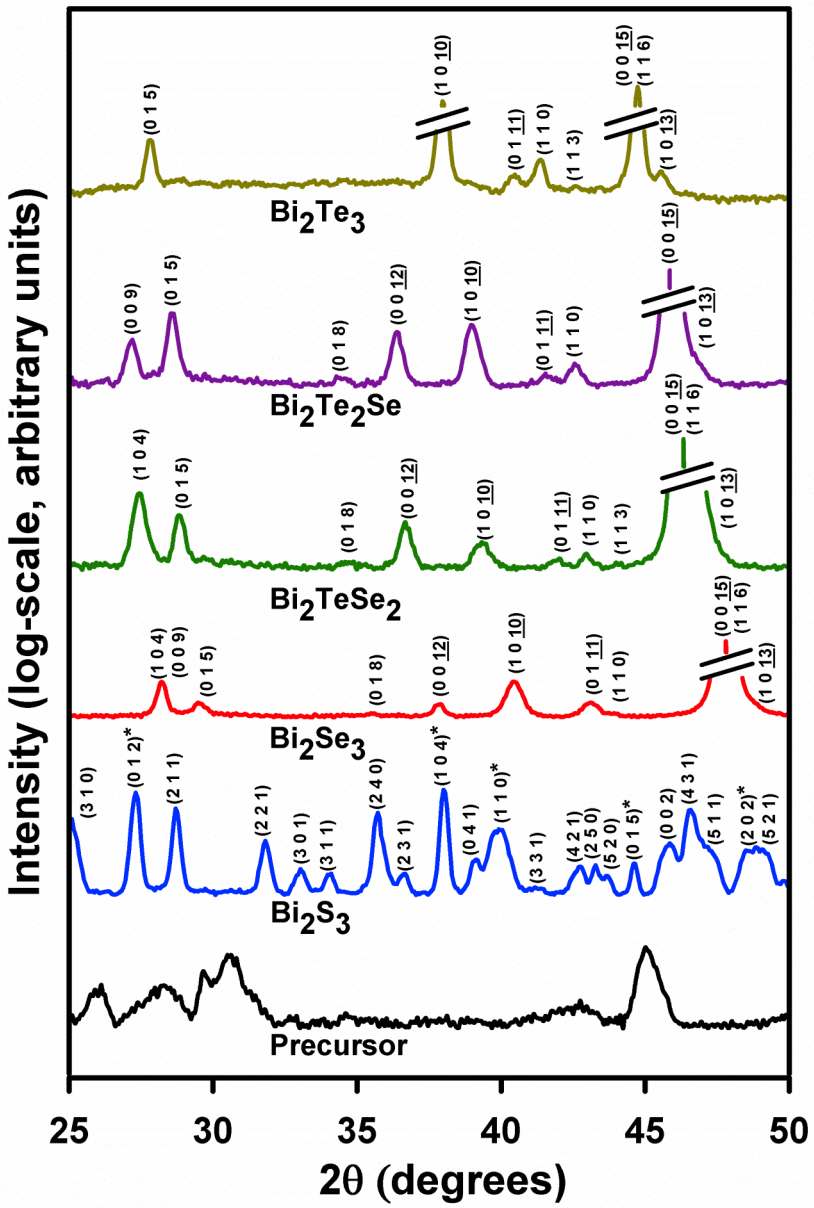

Figure 40 X-ray diffraction patterns from the main text plotted on a log scale with axis-breaks. This version of Figure 1b better illustrates the non-c-axis reflections present in the x-ray diffraction patterns of the Bi_2Te_3, Bi_2Te_2Se, Bi_2TeSe_2 and Bi_2Se_3 films. The Bi_2S_3 film is a mixture of Bi_2S_3 and elemental Bi (peaks labeled with *). All of the observed peaks in the diffraction patterns can be indexed with their respective JCPDS file. In the Bi_2S_3 diffraction pattern, many of the observed peaks can be assigned to multiple indices (i.e. they are likely a superposition of multiple peaks), but for reasons of clarity, the peaks are labeled with only the most intense index.

Thermoelectric Transport Measurements

Thin films for characterization and transport measurements were made by spin-coating the precursors onto substrates. Bi_2Se_3 films were made by annealing the precursor at 250°C for ~30 minutes. To promote incorporation of tellurium into the compounds, the precursors for Bi_2Te_3, Bi_2Te_2Se, and Bi_2TeSe_2 were annealed at 400°C for ~ 30 minutes (when annealed at 250°C, elemental Te peaks were observed in the XRD patterns indicating that the process was incomplete). We note that the low decomposition temperatures of these precursors makes this process compatible with flexible substrates such as high temperature plastics (e.g. kapton). The films were generally 300 – 800 nm thick after annealing as measured by profilometry. Rutherford backscattering spectrometry and energy dispersive x-ray spectroscopy confirm the presence of the indicated elements and the absence of residual sulfur to within the sensitivity of those methods.

The crystal structure of Bi_2Te_3 (which is isomorphous with Bi_2Se_3) is conveniently described as alternating layers of hexagonal monoatomic planes [103]. The layers alternate as $– Te^{(1)} – Bi – Te^{(2)} – Bi – Te^{(1)} –$. In the case of $Bi_2Te_{3-x}Se_x$, Se preferentially substitutes into the $Te^{(2)}$ sites; after the $Te^{(2)}$ sites are filled, Se randomly substitutes into $Te^{(1)}$ sites [104]. The intense (0 0 $\underline{15}$) peaks in the XRD patterns indicate that our polycrystalline films preferentially orient with the c-axis perpendicular to the substrate. The resultant films to possess roughness and porosity of various degrees, which can be seen clearly the scanning electron microscope images in Figure 41. This is a result of the precursor particle size and mass loss during decomposition. The Bi_2Se_3 films were much smoother than the tellurium-containing compounds and had grain sizes in the range of ~ 50 to 500 nm. Although the Bi_2Te_3, Bi_2Te_2Se, and Bi_2TeSe_2 films were rougher, their grains were much more developed and about an order of magnitude larger. Having established this new chemical route to the bismuth chalcogenide family of compounds, we characterized their transport characteristics relevant to thermoelectric performance. The thermoelectric figure of merit, ZT, characterizes the energy conversion efficiency of a thermoelectric material and is given by the expression, $ZT = S^2\sigma T/k$. The symbols S, σ, k, and T denote the Seebeck coefficient (or thermopower), electrical conductivity, thermal conductivity, and absolute temperature, respectively. The best materials used in thermoelectric devices today are bulk semiconductors with $ZT \sim 1$. Figure 42 shows the room temperature values of S, σ, and k for the films prepared in this work.

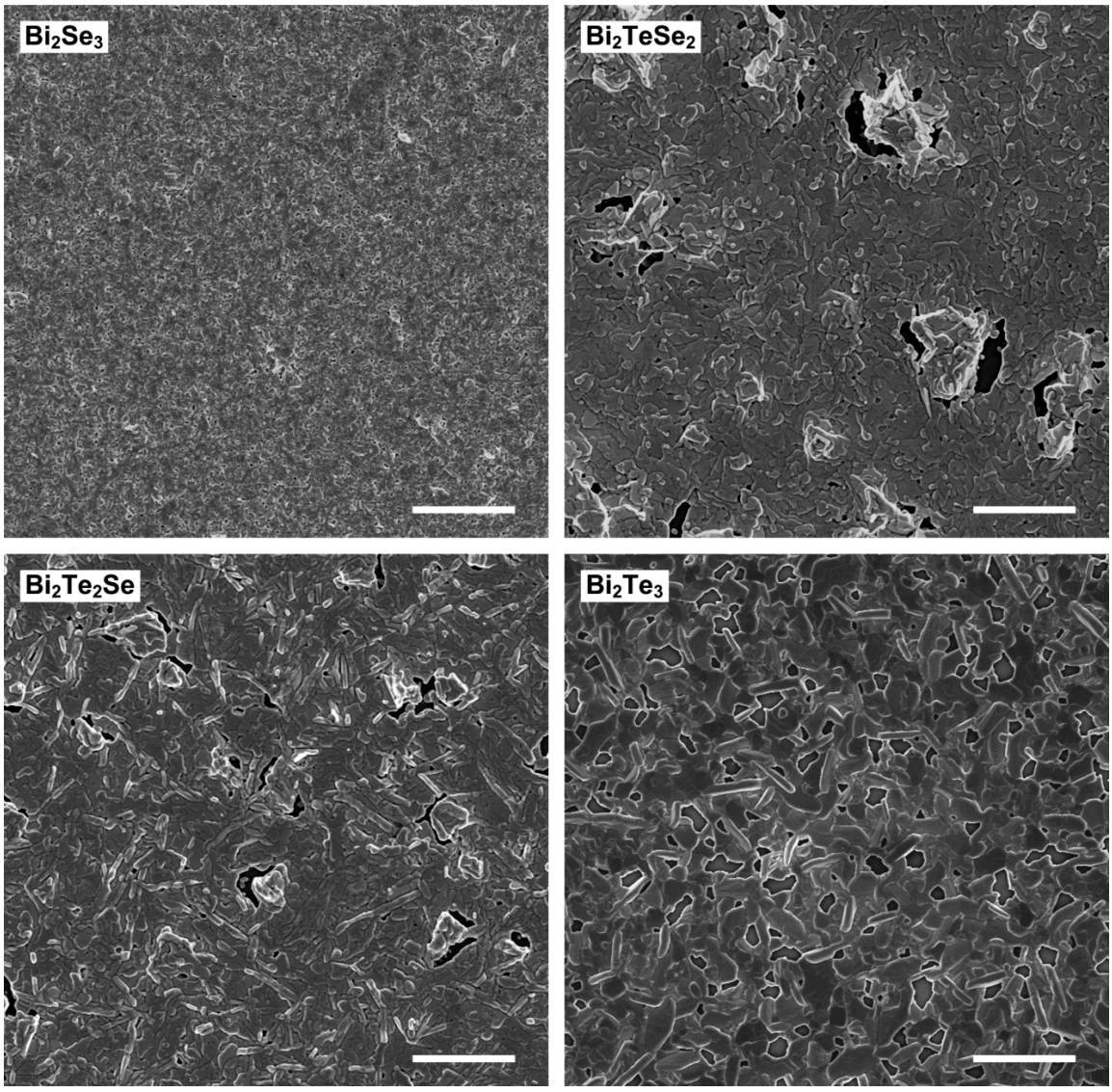

Figure 41 Scanning electron micrographs of typical Bi_2Se_3, Bi_2TeSe_2, Bi_2Te_2Se and Bi_2Te_3 films. The precursor particle size and mass loss during decomposition prevent the films from being smooth and flat. Although the films of the tellurium-containing compounds were much rougher than the Bi_2Se_3 films, their grains were much larger than the Bi_2Se_3 grains. The scale bar in all of the images is 5 µm.

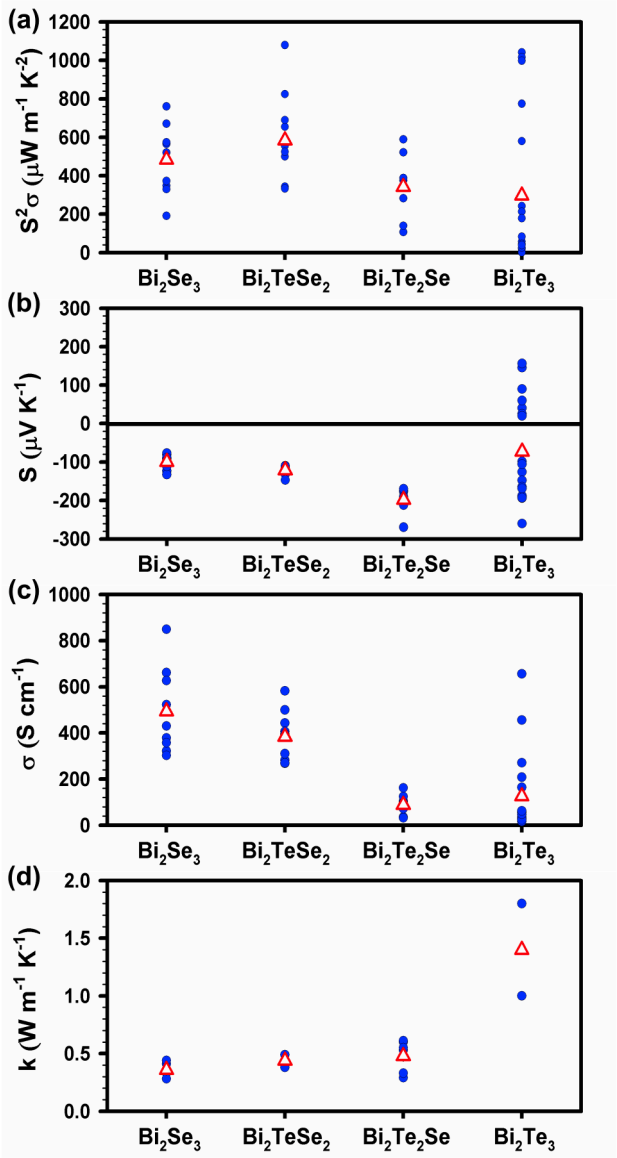

Figure 42 Room temperature transport properties of the films. The filled circles are measurements of individual samples and the open triangles indicate the average value. The measurement uncertainty on individual samples is approximately 7%, 30%, and 30% for S, σ, and k, respectively.

The electrical conductivity and thermopower of the films were measured using top-contact parallel electrodes prepares by hand using silver paint (Ted Pella Inc., Leitsilber 200). Samples were then diced into a more convenient size for charge transport characterization. After decomposing the precursors, the films were routinely handled in air, but for reasons of convenience, charge transport measurements were done on a probe station located inside of a nitrogen filled glovebox. Measurements of both electrical conductivity and thermopower were performed on identical samples. A combination of Agilent 34401A and 34410A multimeters and Keithley 2400 and 2425 sourcemeters were used for the charge transport measurements. The slope of voltage-current plots measured in a 4-point probe configuration was used for measurements of

in-plane electrical conductivity. The film thickness was measured using a Veeco Dektak 150 surface profilometer whereas digital calipers were used to measure the film length and width. To measure in-plane thermopower, the samples were placed on top of two commercial thermoelectric devices, which were used to heat and cool opposite ends of the sample. Thermocouples were used to measure the corresponding hot and cold side temperatures. The open circuit voltage was measured for a variety of temperature differences ranging between -15°C < ΔT < +15°C. Silicone thermal paste was used to improve thermal contact at the thermoelectric device – sample interface and at the thermocouple – sample interface.

Thermal measurements were performed using the 3omega method and analyzed using the the differential method. Samples were prepared by forming the film-of-interest on Si substrates and then depositing a ~200 nm dielectric layer of Parylene. For the heater-line, approximately 200 nm of Au was then evaporated through a shadow mask to form a 3 mm x 60 um line. The heater line width was measured on each sample using a calibrated optical microscope. Each heater/thermometer was calibrated from 20 °C – 35 °C, in order to determine its temperature coefficient of resistance (estimated ~10% uncertainty in TCR). Film thickness was measured after the experiment by scratching the sample adjacent to the heater-line and using a KLA-Tencor Alpha-Step IQ surface profiler.

All compounds exhibit a negative sign of thermopower, which indicates that these films are n-type semiconductors. The n-type behavior indicates that our synthesis generally leads to chalcogen-rich films. Even without extrinsic dopants, our films have remarkably high electrical conductivity; the electrical conductivities of optimally doped thermoelectric materials are only a factor of ~2 greater than our undoped Bi_2Se_3 and Bi_2TeSe_2 [103]. As the film changes from Bi_2Se_3 to Bi_2TeSe_2 to Bi_2Te_2Se, we observe a decrease in electrical conductivity and increase in thermopower, which is consistent with previous reports of the same materials prepared by high-temperature melt-processing [105]. The thermal conductivity of our materials is quite low and comparable to many plastics such as teflon (k = 0.35 W m^{-1} K^{-1}) and high density polyethylene (k = 0.33 W m^{-1} K^{-1}) [106]. To some extent the unusually low thermal conductivity can be explained by film porosity and crystal grain orientation. Nonetheless, it should be noted that these thermal conductivities are 2 – 3 times lower than a recent report that demonstrates enhanced ZT in nanostructured Bi_2Te_3-based alloys via a reduction in thermal conductivity [2].

While we observe clear and consistent trends in the transport properties, sample-to-sample variations are considerable. It is well known that metal-chalcogenide materials can accommodate a range of off-stoichiometric compositions and that this type of precursor chemistry can access these off-stoichiometric compositions [30, 99]. Bi_2Te_3 exhibits the most variable transport properties, which we attribute to variations in tellurium content. Early reports on Bi_2Te_3 [107] showed that varying Te content by just 3% can cause large changes in thermopower and electrical conductivity that are consistent with our observed property variations.

Based upon our room temperature transport measurements, we calculate a ZT of 0.40, 0.39, and 0.22 for Bi_2Se_3, Bi_2TeSe_2, and Bi_2Te_2Se, respectively. To our knowledge, this

is the highest reported ZT for a fully solution-processed material with broad substrate compatability [108, 109]. These values are even more notable since no steps have been taken to optimize carrier concentration or alloying. Due to film anisotropy and measurement directionality (cross-plane for thermal conductivity, in-plane for thermopower and electrical conductivity) we note that these values may overestimate *ZT*. Ideally all measurement directions would have been the same, however measurements of in-plane thermal conductivity [42] and cross-plane thermopower [110] are experimentally challenging to accomplish, and were not possible for these films. The ratio $k_{in\text{-}plane}/k_{cross\text{-}plane}$ of single crystal Bi_2Te_3 [111, 112] ranges from 1.5 – 2.5 and represents the maximum effects of anisotropy; this indicates that our *ZT* is at most overestimated by a factor of 2.5. We anticipate that anisotropy (and hence transport properties) will depend on film thickness due to changes in the substrate's overall influence on grain orientation. Since *ZT* depends only on the ratio, σ/k, the presence of film porosity does not introduce artifacts.

This work demonstrates a simple and universal precursor based on Bi_2S_3 can be used to form all the intermediate compounds of $Bi_2Se_{3-x}Te_x$ which are of importance for thermoelectrics. It is hoped that this approach will lead a path toward thermoelectric modules made by non-pick-and-place methods and may provide a useful matrix material for the materials studied in Chapter 4 and 5.

Future Research

This thesis has made strides towards understanding the physics of nanostructured thermoelectrics as well as the development of several techniques to produce them scalably. While none of the techniques shown here have yet achieved materials with record breaking efficiencies, the approach was quite general and lends itself to further improvements and novel experiments.

For example, it was shown in Chapter 3 that when nanoparticles are embedded in an alloyed matrix, thermal transport is reduced below the alloy limit and can approach the theoretical limit for a disordered crystal. Modeling shows that an optimum nanocrystal size exists depending on the temperature and composition of matrix. While it is difficult to perform a control experiment of this kind using samples made by molecular beam epitaxy, the solution processing approach in Chapter 5 could be a successful route to demostrate this phenomena. Colloidal nanocrystals can be made monodisperse with tunable size. If such particles were embedded in a host material with controlled volume fractions, then the nanoparticle-in-alloy concept could be studied as a function of diameter and volume fraction, which would conclusively prove the existence of an optimum nanocrystal size.

To achieve better electrical properties, the colloidal nanoparticle-in-alloy approach could be combined with hot electron filtering. The basic concept would be to densely embed metallic nanocrystals in a matrix of tunable gap semiconductor (which could be made using the hydrazine precursor approach). The semiconductor regions would serve as a thin barrier for electron transport. Electrons in the metallic particles with energy greater than the conduction band could easily transport between metallic regions; electrons with energy less the conduction band edge would be immobilized. Since the thermopower of a material is determined by the asymmetry of electron conductivity with respect to the chemical potential, if the metals chemical potential were within a few thermal energy units of the semiconductor conduction band edge, then only hot electron would transport and the Seebeck coefficient would be very high, despite large carrier concentration associated with the metal. This concept has successfully been used to yield a ZT~1.4 in the ErAs:$In_{1-x}Ga_xAs$ system [53], and could be more tunably executed using the colloidal nanocrystal approach. Since the matrix and particle can be chosen independently in this approach, such materials would not be restricted by the phase-diagram or self-assembly kinetics. In principle, even earth abundant material systems could be used as thermoelectrics in this configuration, such as Cu embedded in $SnS_{2-x}Se_x$.

One unexpected outcome of the current work is that the thermal transport of finely grained materials made from colloidal nanocrystals are much lower than what is predicted based on boundary scattering alone. It may be useful to measure the phonon density of states directly using advanced spectroscopy techniques such as Inelastic x-ray or neutron scattering. Very few nanostructured materials have been characterized using these techniques because of the difficulty of growing large samples required. However, the colloidal approach can produce large samples easily and thus would be

very amenable to such measurements. Using a direct measurement of the density of states/phonon dispersion it would be possible to distinguish whether the anomalous heat transport is caused by a change in dispersion which may occur as the grain size approached typical phonon wavelengths, or rather a material defect that enhances scattering from within the grains.

Lastly, it should be mentioned that, using the hydrazine precursor approach in chapter 5 and 6, there are a huge number of possible compounds that could be made simply by mixing known precursors (see Table 2). Some of these are already known to be good thermoelectric materials. It would be worthwhile to develop a methodology to pattern these compounds from solution into a module (e.g. spray coating, ink-jet printing, screen printing). Such techniques are non-trivial for thermoelectrics since high performance n and p junctions are simultaneously required, modules are generally thick (>100μm), contact resistances of connection must be low, and double-sided modules are typically used. Thus, despite the obvious analogies between scalable thermoelectrics and photovoltaic technologies, thermoelectrics have their own unique obstacles to overcome. If solution processable thermoelectrics are to succeed, their manufacturing methods must also be developed.

References

[1] G. Chen, *Nanoscale energy transport and conversion : a parallel treatment of electrons, molecules, phonons, and photons*. Oxford ; New York: Oxford University Press, 2005.

[2] B. Poudel, Q. Hao, Y. Ma, Y. C. Lan, A. Minnich, B. Yu, X. A. Yan, D. Z. Wang, A. Muto, D. Vashaee, X. Y. Chen, J. M. Liu, M. S. Dresselhaus, G. Chen, and Z. F. Ren, "High-thermoelectric performance of nanostructured bismuth antimony telluride bulk alloys," *Science,* vol. 320, pp. 634-638, May 2 2008.

[3] L. E. Bell, "Cooling, heating, generating power, and recovering waste heat with thermoelectric systems," *Science,* vol. 321, pp. 1457-1461, Sep 12 2008.

[4] C. B. Vining, "An inconvenient truth about thermoelectrics," *Nature Materials,* vol. 8, pp. 83-85, Feb 2009.

[5] A. Majumdar, "Thermoelectricity in semiconductor nanostructures," *Science,* vol. 303, pp. 777-778, Feb 6 2004.

[6] D. M. Rowe, *Thermoelectrics handbook : macro to nano*. Boca Raton: CRC/Taylor & Francis, 2006.

[7] V. P. Carey, *Liquid-vapor phase-change phenomena : an introduction to the thermophysics of vaporization and condensation processes in heat transfer equipment*, 2nd ed. New York: Taylor and Francis, 2008.

[8] C. Kittel, *Introduction to solid state physics*, 8th ed. Hoboken, NJ: Wiley, 2005.

[9] O. Madelung, *Introduction to solid-state theory*, Study ed. Berlin ; New York: Springer, 1996.

[10] M. K. Farr, J. G. Traylor, and S. K. Sinha, "Lattice-Dynamics of Gasb," *Physical Review B,* vol. 11, pp. 1587-1594, 1975.

[11] J. Callaway, "Model for Lattice Thermal Conductivity at Low Temperatures," *Physical Review,* vol. 113, pp. 1046-1051, 1959.

[12] L. D. Hicks, T. C. Harman, and M. S. Dresselhaus, "Use of Quantum-Well Superlattices to Obtain a High Figure of Merit from Nonconventional Thermoelectric-Materials," *Applied Physics Letters,* vol. 63, pp. 3230-3232, Dec 6 1993.

[13] L. D. Hicks and M. S. Dresselhaus, "Thermoelectric Figure of Merit of a One-Dimensional Conductor," *Physical Review B,* vol. 47, pp. 16631-16634, Jun 15 1993.

[14] L. D. Hicks and M. S. Dresselhaus, "Effect of Quantum-Well Structures on the Thermoelectric Figure of Merit," *Physical Review B,* vol. 47, pp. 12727-12731, May 15 1993.

[15] R. Venkatasubramanian, E. Siivola, T. Colpitts, and B. O'Quinn, "Thin-film thermoelectric devices with high room-temperature figures of merit," *Nature,* vol. 413, pp. 597-602, Oct 11 2001.

[16] K. F. Hsu, S. Loo, F. Guo, W. Chen, J. S. Dyck, C. Uher, T. Hogan, E. K. Polychroniadis, and M. G. Kanatzidis, "Cubic AgPbmSbTe2+m: Bulk thermoelectric materials with high figure of merit," *Science,* vol. 303, pp. 818-821, Feb 6 2004.

[17] A. I. Hochbaum, R. K. Chen, R. D. Delgado, W. J. Liang, E. C. Garnett, M. Najarian, A. Majumdar, and P. D. Yang, "Enhanced thermoelectric performance of rough silicon nanowires," *Nature,* vol. 451, pp. 163-U5, Jan 10 2008.

[18] A. I. Boukai, Y. Bunimovich, J. Tahir-Kheli, J. K. Yu, W. A. Goddard, and J. R. Heath, "Silicon nanowires as efficient thermoelectric materials," *Nature,* vol. 451, pp. 168-171, Jan 10 2008.

[19] J. K. Yu, S. Mitrovic, D. Tham, J. Varghese, and J. R. Heath, "Reduction of thermal conductivity in phononic nanomesh structures," *Nature Nanotechnology,* vol. 5, pp. 718-721, Oct 2010.

[20] W. Kim, S. L. Singer, A. Majumdar, J. M. O. Zide, D. Klenov, A. C. Gossard, and S. Stemmer, "Reducing thermal conductivity of crystalline solids at high temperature using embedded nanostructures," *Nano Letters,* vol. 8, pp. 2097-2099, Jul 2008.

[21] *Tellurium Statistics*: U.S. Geological Survey, 2009.

[22] *Annual Energy Review 2009*: U.S. Energy Information Administration, 2010.

[23] T. C. Harman, P. J. Taylor, M. P. Walsh, and B. E. LaForge, "Quantum dot superlattice thermoelectric materials and devices," *Science,* vol. 297, pp. 2229-2232, Sep 27 2002.

[24] J. M. Zide, J.-H. Bahk, R. Singh, G. Zeng, S. L. Singer, J. P. Feser, D. Xu, Z. X. Bian, A. Majumdar, J. E. Bowers, A. Shakouri, and A. Gossard, "High efficiency thermoelectric materials consisting of epitaxially-grown semimetal/semiconductor nanocomposites," *In Prepartion,* 2009.

[25] Y. Ma, Q. Hao, B. Poudel, Y. C. Lan, B. Yu, D. Z. Wang, G. Chen, and Z. F. Ren, "Enhanced thermoelectric figure-of-merit in p-type nanostructured bismuth antimony tellurium alloys made from elemental chunks," *Nano Letters,* vol. 8, pp. 2580-2584, Aug 2008.

[26] D. V. Talapin and C. B. Murray, "PbSe nanocrystal solids for n- and p-channel thin film field-effect transistors," *Science,* vol. 310, pp. 86-89, Oct 7 2005.

[27] E. V. Shevchenko, D. V. Talapin, N. A. Kotov, S. O'Brien, and C. B. Murray, "Structural diversity in binary nanoparticle superlattices," *Nature,* vol. 439, pp. 55-59, Jan 5 2006.

[28] D. B. Mitzi, L. L. Kosbar, C. E. Murray, M. Copel, and A. Afzali, "High-mobility ultrathin semiconducting films prepared by spin coating," *Nature,* vol. 428, pp. 299-303, Mar 18 2004.

[29] D. B. Mitzi, M. Copel, and C. E. Murray, "High-mobility p-type transistor based on a spin-coated metal telluride semiconductor," *Advanced Materials,* vol. 18, p. 2448, Sep 18 2006.

[30] D. J. Milliron, S. Raoux, R. Shelby, and J. Jordan-Sweet, "Solution-phase deposition and nanopatterning of GeSbSe phase-change materials," *Nature Materials,* vol. 6, pp. 352-356, May 2007.

[31] D. B. Mitzi, S. Raoux, A. G. Schrott, M. Copel, A. Kellock, and J. Jordan-Sweet, "Solution-based processing of the phase-change material KSb5S8," *Chemistry of Materials,* vol. 18, pp. 6278-6282, Dec 26 2006.

[32] D. B. Mitzi, M. Yuan, W. Liu, A. J. Kellock, S. J. Chey, V. Deline, and A. G. Schrott, "A High-Efficiency Solution-Deposited Thin-Film Photovoltaic Device," *Advanced Materials,* vol. 20, p. 3657, Oct 2 2008.

[33] W. Liu, D. B. Mitzi, M. Yuan, A. J. Kellock, S. J. Chey, and O. Gunawan, "12% Efficiency CuIn(Se,S)(2) Photovoltaic Device Prepared Using a Hydrazine Solution Process," *Chemistry of Materials,* vol. 22, pp. 1010-1014, Feb 9 2010.

[34] T. K. Todorov, K. B. Reuter, and D. B. Mitzi, "High-Efficiency Solar Cell with Earth-Abundant Liquid-Processed Absorber," *Advanced Materials,* vol. 22, pp. E156-+, May 25 2010.

[35] M. Yuan, D. B. Mitzi, W. Liu, A. J. Kellock, S. J. Chey, and V. R. Deline, "Optimization of CIGS-Based PV Device through Antimony Doping," *Chemistry of Materials,* vol. 22, pp. 285-287, Jan 26 2010.

[36] M. V. Kovalenko, B. Spokoyny, J. S. Lee, M. Scheele, A. Weber, S. Perera, D. Landry, and D. V. Talapin, "Semiconductor Nanocrystals Functionalized with

Antimony Telluride Zintl Ions for Nanostructured Thermoelectrics," *Journal of the American Chemical Society,* vol. 132, pp. 6686-6695, May 19 2010.

[37] D. B. Mitzi, "Polymorphic one-dimensional (N2H4)(2)ZnTe: Soluble precursors for the formation of hexagonal or cubic zinc telluride," *Inorganic Chemistry,* vol. 44, pp. 7078-7086, Oct 3 2005.

[38] D. B. Mitzi, "N4H9Cu7S4: A hydrazinium-based salt with a layered Cu7S4-framework," *Inorganic Chemistry,* vol. 46, pp. 926-931, Feb 5 2007.

[39] M. V. Kovalenko, M. Scheele, and D. V. Talapin, "Colloidal Nanocrystals with Molecular Metal Chalcogenide Surface Ligands," *Science,* vol. 324, pp. 1417-1420, Jun 12 2009.

[40] D. B. Mitzi, M. Copel, and S. J. Chey, "Low-voltage transistor employing a high-mobility spin-coated chalcogenide semiconductor," *Advanced Materials,* vol. 17, p. 1285, May 13 2005.

[41] D. G. Cahill, "Thermal-Conductivity Measurement from 30-K to 750-K - the 3-Omega Method," *Review of Scientific Instruments,* vol. 61, pp. 802-808, Feb 1990.

[42] T. Borca-Tasciuc, A. R. Kumar, and G. Chen, "Data reduction in 3 omega method for thin-film thermal conductivity determination," *Review of Scientific Instruments,* vol. 72, pp. 2139-2147, Apr 2001.

[43] C. Dames and G. Chen, "1 omega, 2 omega, and 3 omega methods for measurements of thermal properties," *Review of Scientific Instruments,* vol. 76, Dec 2005.

[44] S. M. Lee and D. G. Cahill, "Heat transport in thin dielectric films," *Journal of Applied Physics,* vol. 81, pp. 2590-2595, Mar 15 1997.

[45] T. Tong and A. Majumdar, "Reexamining the 3-omega technique for thin film thermal characterization," *Review of Scientific Instruments,* vol. 77, Oct 2006.

[46] Y. K. Koh, S. L. Singer, W. Kim, J. M. O. Zide, H. Lu, D. G. Cahill, A. Majumdar, and A. C. Gossard, "Comparison of the 3 omega method and time-domain thermoreflectance for measurements of the cross-plane thermal conductivity of epitaxial semiconductors," *Journal of Applied Physics,* vol. 105, Mar 1 2009.

[47] N. T. Nguyen, P. A. Berseth, Q. Y. Lin, C. Chiritescu, D. G. Cahill, A. Mavrokefalos, L. Shi, P. Zschack, M. D. Anderson, I. M. Anderson, and D. C. Johnson, "Synthesis and Properties of Turbostratically Disordered, Ultrathin WSe2 Films," *Chemistry of Materials,* vol. 22, pp. 2750-2756, May 11 2010.

[48] K. Kurabayashi, M. Asheghi, M. Touzelbaev, and K. E. Goodson, "Measurement of the thermal conductivity anisotropy in polyimide films," *Journal of Microelectromechanical Systems,* vol. 8, pp. 180-191, Jun 1999.

[49] D. G. Cahill, S. K. Watson, and R. O. Pohl, "Lower Limit to the Thermal-Conductivity of Disordered Crystals," *Physical Review B,* vol. 46, pp. 6131-6140, Sep 1 1992.

[50] A. G. Briggs, L. J. Challis, and F. W. Sheard, "Thermal Conductivity of Gasb-Insb Alloys at 300 K," *Journal of Physics Part C Solid State Physics,* vol. 3, p. 687, 1970.

[51] W. Kim, J. Zide, A. Gossard, D. Klenov, S. Stemmer, A. Shakouri, and A. Majumdar, "Thermal conductivity reduction and thermoelectric figure of merit increase by embedding nanoparticles in crystalline semiconductors," *Physical Review Letters,* vol. 96, Feb 3 2006.

[52] J. P. Heremans, C. M. Thrush, and D. T. Morelli, "Thermopower enhancement in lead telluride nanostructures," *Physical Review B,* vol. 70, Sep 2004.

[53] J. M. Zide, J.-H. Bahk, R. Singh, G. Zeng, J. P. Feser, D. Xu, S. L. Singer, Z. X. Bian, A. Majumdar, J. E. Bowers, A. Shakouri, and A. Gossard, "High efficiency semimetal/semiconductor nanocomposite thermoelectric materials," *Journal of Applied Physics,* 2010 (accepted).

[54] D. O. Klenov, D. C. Driscoll, A. C. Gossard, and S. Stemmer, "Scanning transmission electron microscopy of ErAs nanoparticles embedded in epitaxial In0.53Ga0.47As layers," *Applied Physics Letters,* vol. 86, Mar 14 2005.

[55] S. Gupta, S. Sethi, and P. K. Bhattacharya, "Picosecond Carrier Lifetime in Erbium-Doped-Gaas," *Applied Physics Letters,* vol. 62, pp. 1128-1130, Mar 8 1993.

[56] L. H. Brixner, "Structure and Electrical Properties of Some New Rare Earth Arsenides, Antimonides and Tellurides," *Journal of Inorganic & Nuclear Chemistry,* vol. 15, pp. 199-201, 1960.

[57] M. P. Hanson, D. C. Driscoll, E. R. Brown, and A. C. Gossard, "ErSb/GaSb metal/semiconductor nanocomposite grown by molecular beam epitaxy," *Transactions of the Indian Institute of Metals,* vol. 59, pp. 167-175, Apr 2006.

[58] B. Abeles, "Lattice Thermal Conductivity of Disordered Semiconductor Alloys at High Temperatures," *Physical Review,* vol. 131, p. 1906, 1963.

[59] W. Kim and A. Majumdar, "Phonon scattering cross section of polydispersed spherical nanoparticles," *Journal of Applied Physics,* vol. 99, Apr 15 2006.

[60] H. C. v. d. Hulst, *Light scattering by small particles*. New York: Dover Publications, 1981.

[61] N. Mingo, D. Hauser, N. P. Kobayashi, M. Plissonnier, and A. Shakouri, ""Nanoparticle-in-Alloy" Approach to Efficient Thermoelectrics: Silicides in SiGe," *Nano Letters,* vol. 9, pp. 711-715, Feb 2009.

[62] P. Sheng, *Introduction to wave scattering, localization, and mesoscopic phenomena*. San Diego: Academic Press, 1995.

[63] G. Chen, M. S. Dresselhaus, G. Dresselhaus, J. P. Fleurial, and T. Caillat, "Recent developments in thermoelectric materials," *International Materials Reviews,* vol. 48, pp. 45-66, Feb 2003.

[64] M. S. Dresselhaus, G. Chen, M. Y. Tang, R. G. Yang, H. Lee, D. Z. Wang, Z. F. Ren, J. P. Fleurial, and P. Gogna, "New directions for low-dimensional thermoelectric materials," *Advanced Materials,* vol. 19, pp. 1043-1053, Apr 20 2007.

[65] S. Franchi, G. Trevisi, L. Seravalli, and P. Frigeri, "Quantum dot nanostructures and molecular beam epitaxy," *Progress in Crystal Growth and Characterization of Materials,* vol. 47, pp. 166-195, 2003.

[66] C. B. Murray, C. R. Kagan, and M. G. Bawendi, "Synthesis and characterization of monodisperse nanocrystals and close-packed nanocrystal assemblies," *Annual Review of Materials Science,* vol. 30, pp. 545-610, 2000.

[67] F. W. Wise, "Lead salt quantum dots: The limit of strong quantum confinement," *Accounts of Chemical Research,* vol. 33, pp. 773-780, Nov 2000.

[68] G. D. Mahan and J. O. Sofo, "The best thermoelectric," *Proceedings of the National Academy of Sciences of the United States of America,* vol. 93, pp. 7436-7439, Jul 1996.

[69] T. E. Humphrey and H. Linke, "Reversible thermoelectric nanomaterials," *Physical Review Letters,* vol. 94, Mar 2005.

[70] G. Chen, *Nanoscale Energy Transport and Conversion*. New York: Oxford, 2005.

[71] W. Kim, R. Wang, and A. Majumdar, "Nanostructuring expands thermal limits," *Nano Today,* vol. 2, pp. 40-47, Feb 2007.

[72] R. Y. Wang, R. A. Segalman, and A. Majumdar, "Room temperature thermal conductance of alkanedithiol self-assembled monolayers," *Applied Physics Letters,* vol. 89, Oct 2006.

[73] R. Prasher, "Ultralow thermal conductivity of a packed bed of crystalline nanoparticles: A theoretical study," *Physical Review B,* vol. 74, Oct 2006.

[74] D. Vanmaekelbergh and P. Liljeroth, "Electron-conducting quantum dot solids: novel materials based on colloidal semiconductor nanocrystals," *Chemical Society Reviews,* vol. 34, pp. 299-312, 2005.

[75] D. Yu, C. J. Wang, B. L. Wehrenberg, and P. Guyot-Sionnest, "Variable range hopping conduction in semiconductor nanocrystal solids," *Physical Review Letters,* vol. 92, May 2004.

[76] C. H. Ben-Porat, O. Cherniavskaya, L. Brus, K. S. Cho, and C. B. Murray, "Electric fields on oxidized silicon surfaces: Static polarization of PbSe nanocrystals," *Journal of Physical Chemistry A,* vol. 108, pp. 7814-7819, Sep 2004.

[77] O. L. Lazarenkova and A. A. Balandin, "Miniband formation in a quantum dot crystal," *Journal of Applied Physics,* vol. 89, pp. 5509-5515, May 2001.

[78] H. Abrams and R. N. Tauber, "Thermoelectric Power of Single-Crystal P-Type Pbse," *Journal of Applied Physics,* vol. 40, pp. 3868-&, 1969.

[79] E. I. Rogacheva, T. V. Tavrina, O. N. Nashchekina, S. N. Grigorov, K. A. Nasedkin, M. S. Dresselhaus, and S. B. Cronin, "Quantum size effects in PbSe quantum wells," *Applied Physics Letters,* vol. 80, pp. 2690-2692, Apr 2002.

[80] A. Javey, J. Guo, Q. Wang, M. Lundstrom, and H. J. Dai, "Ballistic carbon nanotube field-effect transistors," *Nature,* vol. 424, pp. 654-657, Aug 2003.

[81] Z. Y. Zhang, X. L. Liang, S. Wang, K. Yao, Y. F. Hu, Y. Z. Zhu, Q. Chen, W. W. Zhou, Y. Li, Y. G. Yao, J. Zhang, and L. M. Peng, "Doping-free fabrication of carbon nanotube based ballistic CMOS devices and circuits," *Nano Letters,* vol. 7, pp. 3603-3607, Dec 2007.

[82] T. S. Mentzel, V. J. Porter, S. Geyer, K. MacLean, M. G. Bawendi, and M. A. Kastner, "Charge transport in PbSe nanocrystal arrays," *Physical Review B,* vol. 77, Feb 2008.

[83] N. F. Mott, *Conduction in non-crystalline materials*, 2nd ed. Oxford, New York: Oxford University Press, 1993.

[84] E. I. Rogacheva, T. V. Tavrina, S. N. Grigorov, O. N. Nashchenkina, V. V. Volobuev, A. G. Fedorov, K. A. Nasedkin, and M. S. Dresselhaus, "Effect of oxidation on the thermoelectric properties of PbSe thin films," *Journal of Electronic Materials,* vol. 31, pp. 298-303, Apr 2002.

[85] J. O. Sofo, "Thermoelectric Figure of Merit of n-HgCdSe," *Journal of Applied Physics,* vol. 77, pp. 1561-1563, Feb 15 1995.

[86] E. M. Chan, C. X. Xu, A. W. Mao, G. Han, J. S. Owen, B. E. Cohen, and D. J. Milliron, "Reproducible, High-Throughput Synthesis of Colloidal Nanocrystals for Optimization in Multidimensional Parameter Space," *Nano Letters,* vol. 10, pp. 1874-1885, May 2010.

[87] W. W. Yu, L. H. Qu, W. Z. Guo, and X. G. Peng, "Experimental determination of the extinction coefficient of CdTe, CdSe, and CdS nanocrystals," *Chemistry of Materials,* vol. 15, pp. 2854-2860, Jul 15 2003.

[88] B. D. Cullity, *Elements of x-ray diffraction*, 2d ed. Reading, Mass.: Addison-Wesley Pub. Co., 1978.

[89] J. Y. Zhang, X. Y. Wang, M. Xiao, L. Qu, and X. Peng, "Lattice contraction in free-standing CdSe nanocrystals," *Applied Physics Letters,* vol. 81, pp. 2076-2078, Sep 9 2002.

[90] A. V. Ioffe and A. F. Ioffe, "Thermal Conductivity of Semiconductor Solid Solutions," *Soviet Physics-Solid State,* vol. 2, pp. 719-728, 1960.

[91] A. J. Minnich, H. Lee, X. W. Wang, G. Joshi, M. S. Dresselhaus, Z. F. Ren, G. Chen, and D. Vashaee, "Modeling study of thermoelectric SiGe nanocomposites," *Physical Review B,* vol. 80, Oct 2009.

[92] W. Hertz, Waidelic.W, and H. Peisl, "Lattice Contraction Due to Quenching in Vacancies in Platinum and Gold," *Physics Letters A,* vol. A 43, pp. 289-290, 1973.

[93] T. Tanaka, "Lattice-Constant and Nonstoichiometry in Mn-Fe Ferrites," *Japanese Journal of Applied Physics,* vol. 13, pp. 1235-1237, 1974.

[94] A. Burger and M. Roth, "Growth of Medium Electrical-Resistivity Cdse Single-Crystals by the Temperature-Gradient Solution Zoning Technique," *Journal of Crystal Growth,* vol. 67, pp. 507-512, 1984.

[95] Z. C. Huang, E. Eissler, and C. R. Wie, "Role of Cadmium Vacancy-Related Defects in Cdte Nuclear-Detectors," *Nuclear Instruments & Methods in Physics Research Section B-Beam Interactions with Materials and Atoms,* vol. 100, pp. 507-510, Jun 1995.

[96] F. V. Mikulec, M. Kuno, M. Bennati, D. A. Hall, R. G. Griffin, and M. G. Bawendi, "Organometallic synthesis and spectroscopic characterization of manganese-doped CdSe nanocrystals," *Journal of the American Chemical Society,* vol. 122, pp. 2532-2540, Mar 22 2000.

[97] S. R. Forrest, "The path to ubiquitous and low-cost organic electronic appliances on plastic," *Nature,* vol. 428, pp. 911-918, Apr 29 2004.

[98] M. Jayachandran, M. J. Chockalingam, K. R. Murali, and A. S. Lakshmanan, "CuInSe2 for Photovoltaics - a Critical Assessment," *Materials Chemistry and Physics,* vol. 34, pp. 1-13, Apr 1993.

[99] D. B. Mitzi, "Solution Processing of Chalcogenide Semiconductors via Dimensional Reduction," *Advanced Materials,* vol. 21, pp. 3141-3158, Aug 21 2009.

[100] D. J. Milliron, D. B. Mitzi, M. Cope, and C. E. Murray, "Solution-processed metal chalcogenide films for p-type transistors," *Chemistry of Materials,* vol. 18, pp. 587-590, Feb 7 2006.

[101] D. B. Mitzi, M. Yuan, W. Liu, A. J. Kellock, S. J. Chey, L. Gignac, and A. G. Schrott, "Hydrazine-based deposition route for device-quality CIGS films," *Thin Solid Films,* vol. 517, pp. 2158-2162, Feb 2 2009.

[102] R. Y. Wang, J. P. Feser, X. Gu, K. M. Yu, R. A. Segalman, A. Majumdar, D. J. Milliron, and J. J. Urban, "Universal and Solution-Processable Precursor to Bismuth Chalcogenide Thermoelectrics," *Chemistry of Materials,* vol. 22, pp. 1943-1945, Mar 23 2010.

[103] H. Scherrer and S. Scherrer, in *Thermoelectrics Handbook: Macro to Nano*, D. M. Rowe, Ed., ed Boca Raton: CRC, 2006.

[104] H. Scherrer and S. Scherrer, "Thermoelectric Properties of Bismuth Antimony Telluride Solid Solutions," in *Thermoelectrics Handbook Macro to Nano*, D. M. Rowe, Ed., ed Boca Raton, USA: CRC, 2006.

[105] N. Fuschillo, J. N. Bierly, and F. J. Donahoe, "Transport Properties of the Pseudo-Binary Alloy System Bi2te3-Ysey," *Journal of Physics and Chemistry of Solids,* vol. 8, pp. 430-433, 1959.

[106] A. F. Mills, *Basic heat and mass transfer*, 2nd ed. Upper Saddle River, N.J.: Prentice Hall, 1999.

[107] C. B. Satterthwaite and R. W. Ure, "Electrical and Thermal Properties of Bi2Te3," *Physical Review,* vol. 108, pp. 1164-1170, 1957.

[108] R. Y. Wang, J. P. Feser, J. S. Lee, D. V. Talapin, R. Segalman, and A. Majumdar, "Enhanced thermopower in PbSe nanocrystal quantum dot superlattices," *Nano Letters,* vol. 8, pp. 2283-2288, Aug 2008.

[109] A. Zimmer, N. Stein, H. Terryn, and C. Boulanger, "Optical and thermoelectric characterizations of electroplated n-Bi-2(Te0.9Se0.1)(3)," *Journal of Physics and Chemistry of Solids,* vol. 68, pp. 1902-1907, Oct 2007.

[110] G. H. Zeng, J. M. O. Zide, W. Kim, J. E. Bowers, A. C. Gossard, Z. X. Bian, Y. Zhang, A. Shakouri, S. L. Singer, and A. Majumdar, "Cross-plane Seebeck coefficient of ErAs : InGaAs/InGaAlAs superlattices," *Journal of Applied Physics,* vol. 101, Feb 1 2007.

[111] H. Kaibe, Y. Tanaka, M. Sakata, and I. Nishida, "Anisotropic Galvanomagnetic and Thermoelectric Properties of N-Type Bi2Te3 Single-Crystal with the Composition of a Useful Thermoelectric Cooling Material," *Journal of Physics and Chemistry of Solids,* vol. 50, pp. 945-950, 1989.

[112] J. P. Fleurial, L. Gailliard, R. Triboulet, H. Scherrer, and S. Scherrer, "Thermal-Properties of High-Quality Single-Crystals of Bismuth Telluride .1. Experimental Characterization," *Journal of Physics and Chemistry of Solids,* vol. 49, pp. 1237-1247, 1988.

Appendix I: Calculating Uncertainty in dT/dR Using Statistical Methods

The temperature coefficent of resistance is a key parameter for 3ω experiments and other experiment based on resistive thermometers. Often, if the other aspects of the experiment are designed correctly, the uncertainty in dT/dR determines the accuracy of the method, and thus its uncertainty is vital to estimate. The TCR is determined from a fit to the measured R vs T curve, typically by a low-order polynomial. A procedure will be shown of how to calculate the uncertainty in dT/dR from a generalized linear regression of the T vs. R curve.

Consider a data set with N points y_i, x_i . A polynomial of order p can be fit to the data in the least square sense, using a generalized linear regression. To calculate the coefficients of the polynomial

$$y = \sum_{k=0}^{p} \beta_k x^k \tag{5.1}$$

matrix of data is formed

$$\Pi \equiv \begin{bmatrix} 1 & x_1 & x_1^2 & \cdots & x_1^p \\ 1 & x_2 & x_2^2 & & x_2^p \\ \vdots & & & \ddots & \\ 1 & x_N & x_N^2 & & x_N^p \end{bmatrix} \tag{5.2}$$

whence the predicted values of the function are

$$\hat{y} = \Pi\tilde{\beta} \tag{5.3}$$

and residual values are

$$\tilde{r} = \tilde{y} - \hat{y} \tag{5.4}$$

. The minimum associated with the sum of the squares of the residuals is given by

$$\tilde{\beta} = (\Pi^T\Pi)^{-1}\Pi^T\tilde{y} \tag{5.5}$$

and thus the regression coefficients are found. Defining $SSE \equiv \tilde{r}^T\tilde{r}$ (the sum of the squares of residuals), it can be shown that the covariance matrix is given by

$$\sigma_{\beta,i}\sigma_{\beta,j} = \frac{SSE}{N-p-1}\left(\Pi^T\Pi\right)^{-1} \tag{5.6}$$

. The standard deviations of the individual regression coefficients are given by the diagonal terms of the matrix; the off-diagonal terms are a measure of the correlation between the coefficients. Since the primary interest is not in the uncertainty of the

coefficients, but rather the uncertainty in the slope of the polynomial, we can use the formula for error propagation in a *correlated* system:

$$\sigma_f^2 = \sum_{i=0}^{p}\sum_{j=0}^{p}\frac{\partial f}{\partial \beta_i}\frac{\partial f}{\partial \beta_j}\sigma_{\beta,i}\sigma_{\beta,j} \qquad 5.7$$

For the current application, the regression is determined for

$$T = \sum_{k=0}^{p}\beta_k R^k \qquad 5.8$$

Taking the derivative,

$$\frac{dT}{dR} = \sum_{k=0}^{p} k\beta_k R^{k-1} \qquad 5.9$$

the uncertainty can then be determined using

$$\frac{\partial}{\partial \beta_i}\left(\frac{dT}{dR}\right) = iR^{i-1} \qquad 5.10$$

which gives

$$\left(\Delta\frac{dT}{dR}\right)^2 = \sum_{i=0}^{p}\sum_{j=0}^{p} ijR^{i+j-2}(\sigma_{\beta_i}\sigma_{\beta_j}) \qquad 5.11$$

where the last term is the covariance matrix determined using 5.6. Note that in order to get any particular confidence interval, the standard error should be scaled by a factor that depends on the degrees of freedom through the t-test. In the limiting case of infinite degrees-of-freedom, the factor is 2.2 for 95% confidence. In the current work, the uncertainty in dT/dR for experiments is calculated using equation 5.11.

Appendix II: MATLAB Code for Simulating Multi-layer Anisotropic Thermal Transport

```
%Calculates the "3w profile" for N layers, each with anisotropic
%conductivity.  The substrate (layer N) is considered semi-infinite.
%
% frequencies is a vector of VOLTAGE SOURCE FREQUENCIES in Hertz (NOT
% rad/s)
%
%Definitions:
%N:  Number of Layers
%ky: Vector of cross-plane conductivities (layer 1 is the topmost layer,
layer N is the substrate)
%kx: Vector of in-plane thermal conductivities
%Cv: Volumetric Heat Capacity of each layer (J/m3*K)
%d: Vector of layer thicknesses (includes substrate even if its
%semiinfinite)
% P: Heater power (W)
% L: Heater line length (m)
% b: Heater HALF-width (i.e. 1.5e-6 for a 3um wide line!)
%
%example: [deltaT,freqvect]=FullModelFunction(3,[1.5 10 18],[1.5 5 18],
%               1e7*[1 1 1],1e-6*[0.27 2 1000],.5^2/30,400e-6,7.5e-6)
function
[deltaT,freqvect]=FullModelFunctionv4(N,ky,kx,Cv,d,P,L,b,frequencies)

kxy=kx./ky;
alphay=ky./Cv;
www=sqrt(-1); %"i"

Lfreq=length(frequencies);
freqvect=zeros(Lfreq,1);
for i=1:Lfreq
    freqvect(i,1)=frequencies(i);
end

lambdamax=10*2*pi/min([d,w]);
lambdamin=0.01*2*pi/max([d,w]);
lambdainc=lambdamax/1e2;
lambda=[0,logspace(log10(lambdamin),log10(lambdamax),1e2)]; %row vector (1 x
LLambda)
LLambda=length(lambda);

omega=2*pi*freqvect; %column vector (LOmega x 1)
LOmega=length(omega);

omegaM=omega*ones(1,LLambda);
lambdaM=ones(LOmega,1)*lambda;

    B=sqrt(kxy(N).*lambdaM.^2+www*(2.*omegaM/alphay(N)));
    A=-1*ones(LOmega,LLambda);
    if N~=1
        for layer=N:-1:2
```

```
            Bminus=(kxy(layer-1).*lambdaM.^2+www*2.*omegaM/alphay(layer-
1)).^0.5;
            phiminus=Bminus*d(layer-1);
            term1=A.*(ky(layer)*B)./(ky(layer-1)*Bminus);
            Aminus=(term1-tanh(phiminus))./(1-term1.*tanh(phiminus));
            A=Aminus;
            B=Bminus;
        end
    end
integrand=1./(A.*B).*sin(b*lambdaM).^2./(b.*lambdaM).^2;
integrand(:,1)=1./(A(:,1).*B(:,1));

index=1:length(lambda)-1;
integral=zeros(length(freqvect),1);
for i=index;
    integral=integral+(integrand(:,i)+integrand(:,i+1))*0.5*(lambda(i+1)-
lambda(i));
end

deltaT=-P./(pi*L*ky(1))*integral;
%END OF CODE
```